

DISSERTATION

submitted to the
Combined Faculty of Natural Sciences and Mathematics
of Heidelberg University, Germany
for the degree of
Doctor of Natural Sciences

Put forward by
SIMON HEINZE
born in Duisburg, Germany
Oral examination: 19th of May, 2021

MATERIAL-SPECIFIC SIMULATIONS
OF MANY-BODY ELECTRON DYNAMICS

Referees: PROF. DR. MAURITS W. HAVERKORT
PROF. DR. TILMAN ENSS

Materialspezifische Simulationen der Vielteilchendynamik von Elektronen

Die für diese Arbeit relevanten theoretischen Methoden werden hergeleitet, beginnend mit einer Dichtefunktionaltheorierechnung und endend bei einer vollen Vielteilchenbeschreibung.

Sie werden genutzt, um die Dynamik des oftmals untersuchten Nickel^{II}oxidkristalls unter dem Einfluss eines treibenden Lasers zu simulieren. Es wird diskutiert, unter welchen Bedingungen verschiedene Anregungen möglich sind, wie sie sich zeitlich aufgelöst verhalten, und wie dieses Verhalten durch Auger-Meitner Zerfall beeinflusst wird.

Ähnliche Methoden werden auf das komplett andere System des Schwefelhexafluorids angewandt. Es wird gezeigt, dass ein Laser die effektive Austauschwechselwirkungsenergie erhöhen kann, welche unterschiedliche Vielteilchenzustände miteinander koppelt. Die experimentelle Messung wird durch mehrere theoretische Methoden reproduziert. Die vorgestellte Technik ist ein Beitrag zu dem Feld der durch Laser kontrollierten chemischen Reaktionen.

Das letzte untersuchte System ist holmiumdotiertes Gold. Das Elektroneneinfangspektrum von Holmium wird berechnet, und der Effekt von Auger-Meitner-Zerfall und der Goldumgebung als Selbstenergie hinzugefügt. Dieser *ab-initio*-Ansatz führt zu einem neuen Maß an Übereinstimmung mit der experimentellen Messung und ebnet einer schlussendlichen Bestimmung der Elektronenneutrinomasse aus den Ergebnissen den Weg.

Material-specific Simulations of many-body Electron Dynamics

Beginning with a Density Functional Theory calculation and ending with a full many-body description, the theoretical methods relevant for this thesis are derived.

They are used to simulate the dynamics of the thoroughly studied Nickel^{II}oxide crystal under the influence of a driving laser. The conditions in which various excitations are possible are being discussed, as well as how they behave in the time domain and how Auger-Meitner decay influences this behaviour.

Similar methods are applied to the completely different system of Sulphur-hexafluoride. It is shown that a tuning laser can increase the effective exchange interaction, which couples various many-body states. The experimental measurement is reproduced using several theoretical methods. The presented technique is a contribution to the field of laser controlled chemical reactions.

The last system under consideration is Holmium-doped Gold. The electron capture spectrum of Holmium is calculated, and the effect of Auger-Meitner decay and the Gold environment incorporated as a self-energy. This *ab initio* approach leads to a novel degree of agreement with the experimental measurement, paving the way to eventually extracting the mass of the electron neutrino from the results.

Contents

I	Methodologies	5
1	Density Functional Theory	7
1.1	Theory	7
1.2	FPLO	9
2	QUANTY	11
2.1	A Basis of Slater-determinants	11
2.2	Operators in second Quantisation	13
2.3	Lánczos Algorithm and Krylov Basis	15
3	Processing DFT Results	19
3.1	Active Space Atomic-like Orbitals	19
3.2	Rotation to a convenient Space	21
3.3	Adding Interaction	23
3.4	The $U - \Delta$ Formalism	24
4	Calculating physical Quantities	27
4.1	Eigensystems	27
4.2	Spectra	28
4.3	Self-energies	29
4.4	Time Evolutions	31
II	Applications	41
5	Nickel^{II}oxide	43
5.1	Motivation	43
5.2	Two Level System	44
5.3	Crystal Field Theory	47
5.4	Ligand Field Theory	49
5.5	Ligand Field Theory with Auger-Meitner decay	53
5.6	Discussion	60
6	Sulphur-hexafluoride	63
6.1	Motivation	63
6.2	Few-Configuration Fit	64

6.3	<i>Ab initio</i> many-body Simulation	75
6.4	Discussion	81
7	Holmium-doped Gold	83
7.1	Motivation	83
7.2	Atomic Ho vs. Au:Ho	84
7.3	Self-energy due to Auger-Meitner decay	90
7.4	Self-energy due to the Gold environment	95
7.5	Discussion	101
III Conclusions		103
8	Summary of Results and Outlook	105
9	Acknowledgements	109
	List of Abbreviations	113
	List of Publications	115
	List of Figures	115
	List of Tables	116
	Bibliography	117

“Throw physic to the dogs; I’ll none of it.”
-Macbeth, Act 5, Scene 3

Introduction

Motivation

The purpose of theoretical physics is to find a mathematical model that can aptly describe the behaviour of nature in certain circumstances. This model should ideally be based solely on fundamental parameters, because it is then possible to test and adjust the initial assumptions to not only reproduce experimental results, but also generate new insights.

One of the most common techniques used in experiments for extracting information about the dynamics of quantum mechanical systems is the measurement of spectra. They record how an ensemble of particles reacts to being excited, be it from an external or internal source like a laser or a radioactive decay. An intricate interplay with theory allows to not only observe the system but to eventually understand it.

This gain in knowledge usually leads to a plethora of applications. Specifically the field of photochemistry, in which chemical reactions are initiated by light-matter interactions, shall be mentioned here. The great degree of precision with which lasers can be controlled recently granted access to chemical reactions far from equilibrium which would not be possible otherwise.⁴⁹ This technique is for example used in the diverse fields of synthesis, solar energy conversion, information technology and medicinal therapy.²²

With ever improving experimental resolution arises the need for a precise quantitative theoretical description. In rare instances this can be achieved by a set of analytically solvable equations, but most theoretical models require a numerical simulation to adequately reproduce experimental results.

Characterising a fermionic quantum many-body system by writing down its Hamiltonian on a fundamental level is easily done in most cases. However, carrying out any corresponding calculations quickly brings every computer to its limits. The Hilbert space of a system reduced to N available one-particle orbitals and k interacting fermions is spanned by the Slater-determinants representing all pos-

sible configurations, and thus has a dimension given by the binomial coefficient $\binom{N}{k} = N!/k!(N-k)!$. Storing, for example, all coefficients of but one state of a system comprised of the C-2s and C-2p orbitals of a C₆₀ Fullerene would require $\binom{60 \cdot 8}{60 \cdot 4} \approx 10^{143}$ bytes, a number which is 63 orders of magnitude larger than the estimated number of atoms in the observable universe. This disproportionality between the size of interacting quantum systems and their corresponding Hilbert spaces is known as the exponential wall.⁴¹

It is thus apparent that the fundamental laws of physics and the knowledge of the system alone are insufficient to predict the behaviour of even a reasonably small molecule, let alone a macroscopic object like a crystal. In his article³ “More is Different”, Philip Anderson aptly states that “[t]he ability to reduce everything to simple fundamental laws does not imply the ability to start from those laws and reconstruct the universe”. Hence, the aim of the theoretical aspect of any field of exact science is to find approximations and models that lead to sufficiently accurate results while being numerically or even analytically feasible.

Anderson wedges many-body physics between particle physics and chemistry, as being based on the former, and being the basis for the latter. The aim of this thesis, despite it belonging to only one of the fields, is to lay the foundations to contribute to all three.

Outline

One important milestone on the road of finding a mathematical description for many-body physics is the development of Density Functional Theory (abbr. ‘DFT’). While in principle it makes the exact statement that the ground state of a system is uniquely described by its one-particle density matrix, most of its implementations operate on a mean field level. Because of this simplification, and despite its shortcomings, DFT is able to correctly predict several properties of numerous chemical compounds. The theoretical groundwork for DFT is briefly outlined in section 1, and a code that numerically implements it is introduced.

For systems which are insufficiently described by DFT it is still a reasonably good starting point for a many-body calculation. This comes with a plethora of new computational challenges, which are tackled by QUANTY. This quantum many-body tool is the basis for almost all results encountered throughout this thesis. Therefore, section 2 is dedicated to describing its basic structure and one of its most important features, the Lánczos algorithm.

The step from one-particle DFT to full many-body calculation is not straightforward. Keeping all one-particle orbitals would inflate the Hilbert space to un-

managable size, and the explicit inclusion of Coulomb interaction has to come with a correction for its implicit inclusion in DFT. Several techniques used in this thesis to overcome these challenges are presented in section 3.

Once the Hamiltonian of the system is known, QUANTY can be used to calculate physical quantities like eigensystems, spectra, self-energies or time evolutions. The steps necessary to find these are derived in section 4, making heavy use of the Lánczos algorithm.

With the theoretical groundwork laid out, this thesis proceeds to apply it to three very different physical systems. The first is Nickel^{II} oxide, a very thoroughly studied transition metal complex presented in section 5. The time evolution in the density formalism is calculated to study the response of the system to varying laser sources, with and without the inclusion of an idealised Auger-Meitner decay mechanism.

The second system is the molecule Sulphur-hexafluoride, discussed in section 6. A simplified fit model as well as an *ab initio* simulation are used to reproduce the experimentally measured effects an external laser field has on the effective exchange energy between various configurations, as manifested in the X-ray absorption spectrum. Understanding and controlling this interaction is a step towards laser-driven chemistry on a sub-nucleonic timescale.

The system examined in section 7 is Holmium-doped Gold. A detailed reproduction of the experimentally measured energy spectrum of the electron capture decay of ¹⁶³Holmium is achieved by introducing the effects of Auger-Meitner decay as well as that of the Gold environment as a self-energy. This accurate description can eventually lead the way to deriving the numerical value of the electron neutrino mass.

A summary of all results as well as an outlook for future studies is given in section 8.

Part I
Methodologies

1 Density Functional Theory

In Density Functional Theory (abbr. ‘DFT’) the one-particle density matrix of an electronic many-body system replaces the wave function as the entity used to derive measurable quantities. Although it is conceptionally an exact theory, DFT is usually implemented as a mean field theory, yet it works excitingly well for many applications, especially for open atomic shells with an angular momentum quantum number of $l \leq 1$. Where DFT does not work well, it still provides a good basis to improve upon, as explained in section 3. This section sketches out the most important contributions to the theory of DFT and briefly describes FPLO, a code used to implement it.

1.1 Theory

In 1964 Hohenberg and Kohn proved that for a system of electrons under an external potential v the electronic ground state one-particle density matrix n is a unique functional of v and vice versa, if the ground state is non-degenerate.³⁴

They subsequently formally defined a universal functional $F[n]$, in which for any external potential v the total energy

$$\begin{aligned} E_v[n] &\stackrel{\text{def}}{=} \int v(\vec{r})n(\vec{r})d\vec{r} + F[n] \\ &\stackrel{\text{def}}{=} \int v(\vec{r})n(\vec{r})d\vec{r} + \frac{1}{2} \iint \frac{n(\vec{r})n(\vec{r}')}{|\vec{r} - \vec{r}'|} d\vec{r}d\vec{r}' + G[n] \end{aligned} \quad (1.1)$$

gives the correct ground state energy if n is the correct ground state density.

In the following year Kohn and Sham developed an approximation of this formally exact equation by writing⁴²

$$G[n] \stackrel{\text{def}}{=} T_s[n] + E_{xc}[n] \quad , \quad (1.2)$$

with the kinetic energy functional $T_s[n]$ and the exchange and correlation energy functional

$$E_{xc}[n] \stackrel{\text{def}}{=} \int n(\vec{r}) \epsilon_{xc}(n(\vec{r})) d\vec{r} . \quad (1.3)$$

By using that $E_v[n]$ is minimal for the correct ground state density one finds, using the variational principle, that

$$\int \delta n(\vec{r}) \left(\varphi(\vec{r}) + \frac{\delta T_s[n]}{\delta n(\vec{r})} + \mu_{xc}(n(\vec{r})) \right) d\vec{r} = 0 , \quad (1.4)$$

where

$$\varphi(\vec{r}) \stackrel{\text{def}}{=} v(\vec{r}) + \int \frac{n(\vec{r}')}{|\vec{r} - \vec{r}'|} d\vec{r}' \quad (1.5)$$

is the potential experienced by an electron at position \vec{r} , and

$$\mu_{xc}(n) \stackrel{\text{def}}{=} \frac{d(n\epsilon_{xc}(n))}{dn} \quad (1.6)$$

is the effective exchange- and Coulomb-induced chemical potential.

By comparing equation (1.4) and $\int \delta n(\vec{r}) d\vec{r} = 0$ to a fictitious non-interacting system the authors found that this is equivalent to the Schrödinger equation

$$\underbrace{\left(-\frac{1}{2} \nabla^2 + \varphi(\vec{r}) + \mu_{xc}(n(\vec{r})) \right)}_{\stackrel{\text{def}}{=} \mathcal{H}_{DFT}} \psi_i(\vec{r}) = \epsilon_i \psi_i(\vec{r}) , \quad (1.7)$$

meaning that solving this equation gives the same result for n as solving equation (1.4), with

$$n(\vec{r}) \stackrel{\text{def}}{=} \sum_{i=1}^N |\psi_i(\vec{r})|^2 . \quad (1.8)$$

In a numerical implementation this set of the so called ‘Kohn-Sham-equations’ can be solved self-consistently using the following algorithm:

1. Assume a starting density n .
2. Use n , equation (1.5) and equation (1.6) to calculate φ and μ_{xc} .

3. Use the results obtained above to solve the one-particle Schrödinger equation (1.7) for a set of ψ_i .
4. Use equation (1.8) to find a new density n .
5. If a convergence criterion is not met, go back to step 2 using the new n . Otherwise terminate.

None of these steps inherently scale exponentially.

The only quantity in this procedure whose exact analytical form is not known is $\epsilon_{xc}(n(\vec{r}))$ and subsequently the exchange-correlation functional $E_{xc}[n]$. The educated guess for an approximation made here decides how well the final ground state density represents the many-body result. All calculations in this thesis are based on the Perdew-Wang local density approximation functional.⁶⁵

1.2 FPLO

A large number of codes that solve the Kohn-Sham equations self-consistently exist today, each with their own set of up- and downsides. Because Density Functional Theory only makes a statement about the ground state of a system the codes are optimised for the occupied orbitals. Consequently, the properties of the unoccupied orbitals greatly depend on the choice of code, and of the basis set therein.

The simulations detailed in section 6 and section 7 are based on a calculation with the DFT code FPLO⁴⁰ (which stands for ‘Full-Potential Local-Orbital’). It is developed primarily for calculating properties of crystals, but also provides functionalities to do calculations for molecules (which it implements by setting the lattice constant to a very large value).

It comes with a set of basis functions for most elements, which are represented by a real spherical harmonic times a radial function on a grid, trapped on a finite lattice with softened boundary conditions.

Among the features implemented in FPLO are modules for doing a force-relaxation as well as a downfolding, the latter of which is further explained in section 3.1.

The output of a converged FPLO calculation includes the radial functions of the basis orbitals and the Kohn-Sham Hamiltonian \mathcal{H}_{DFT} from equation (1.7) expressed in a suitable basis. Both can be read in and processed by QUANTY.

2 QUANTY

The quantum many-body tool QUANTY^{31,32} is an extension of the script language Lua.* It is developed by Maurits W. Haverkort et. al. and written in the C/C++ programming language. Its aim is to combine the versatility of Lua with the speed of C/C++ to provide the user with the means to do precise material-specific quantum calculations, which are further elaborated on in section 4, in reasonably short time.

It features numerous built-in functionalities for handling wave functions and operators, which are briefly described here. Common tasks like the calculations of eigensystems or spectra are implemented, while the program is versatile enough that less common quantities like time evolutions or self-energies can be constructed by the user (compare section 4).

To overcome the exponential wall of quantum physics QUANTY contains an implementation of modified Restricted Active Space Configuration Interaction (abbr. ‘RASCI’), which restricts any calculations to a portion of the Hilbert space that is large enough to contain the most important contributions to the quantity of interest, but small enough to be handled by the computer at the user’s disposal.

2.1 A Basis of Slater-determinants

The state of a single particle labelled j can be described in terms of one-particle orbitals. These are square-integrable complex-valued functions

$$\chi : \mathbb{R}^3 \rightarrow \mathbb{C} \quad , \quad \chi \in L^2 \quad \Leftrightarrow \quad \int_{\mathbb{R}^3} |\chi(\vec{x}_j)|^2 d\vec{x}_j < \infty \quad ,$$

which span an infinite-dimensional vector space \mathbb{H}_j . For a numerical treatment the dimension of this space has to be truncated, so in practice \mathbb{H}_j is restricted to a finite number of N orbitals. Linear operators corresponding to one-particle observables can on this space be represented by $N \times N$ matrices.

*The code can be downloaded and a documentation found on www.quanty.org.

To describe the state of an interacting fermionic system a more elaborate formalism is needed. Any operator describing the interaction between fermions will depend on the state of several particles, so that the Hilbert space of the complete system is needed. It is mathematically given by the tensor product space

$$\mathbb{H} = \bigotimes_{j=1}^F \mathbb{H}_j \quad , \quad (2.1)$$

where F is the number of particles in the system. One element of \mathbb{H} , which at first glance describes the fermions being distributed over one-particle orbitals χ_j with indices j_1, \dots, j_F , is for example given by

$$\psi : \mathbb{R}^{3F} \rightarrow \mathbb{C} \quad , \quad \psi(\vec{x}_1, \dots, \vec{x}_F) = \chi_{j_1}(\vec{x}_1) \cdots \chi_{j_F}(\vec{x}_F) \quad . \quad (2.2)$$

However, the space \mathbb{H}_ϕ of physical states is smaller than \mathbb{H} , because it contains only those elements that fulfil Fermi statistics, and thus Pauli's exclusion principle.⁶¹ In fact, ψ in equation (2.2) is not in \mathbb{H}_ϕ , because the wave function has to be antisymmetric under the exchange of the positions of two of the (indistinguishable) fermions.

\mathbb{H}_ϕ is spanned by the set of Slater-determinants.⁷¹ They are defined as

$$S_{j_1, \dots, j_F}(\vec{x}_1, \dots, \vec{x}_F) \stackrel{\text{def}}{=} \frac{1}{\sqrt{F!}} \begin{vmatrix} \chi_{j_1}(\vec{x}_1) & \chi_{j_1}(\vec{x}_2) & \cdots & \chi_{j_1}(\vec{x}_F) \\ \chi_{j_2}(\vec{x}_1) & \chi_{j_2}(\vec{x}_2) & \cdots & \chi_{j_2}(\vec{x}_F) \\ \cdots & \cdots & \ddots & \cdots \\ \chi_{j_F}(\vec{x}_1) & \chi_{j_F}(\vec{x}_2) & \cdots & \chi_{j_F}(\vec{x}_F) \end{vmatrix} \quad , \quad (2.3)$$

where $|\cdot|$ denotes the determinant and guarantees antisymmetry under the exchange of two particle positions, and, accordingly, that the object vanishes if two particles occupy the same orbital.

In Dirac notation the Slater-determinants can be written as

$$|j_1, \dots, j_F\rangle \stackrel{\text{def}}{=} \frac{1}{\sqrt{F!}} \sum_p \text{sgn}(p) \bigotimes_{k=1}^F |\chi_{p(k)}\rangle \quad , \quad (2.4)$$

where p goes through all possible bijective functions $p : \{1, \dots, F\} \rightarrow \{j_1, \dots, j_F\}$ and $\text{sgn}(p)$ assigns the appropriate sign.

Depending on the circumstances this is also exemplary encountered as

$$|j_1, \dots, j_F\rangle \stackrel{\text{def}}{=} |001011 \cdots\rangle \quad , \quad (2.5)$$

where all one-particle orbitals are labelled with either 1 if they are occupied, or 0 if they are not. This has the advantage that the total number of orbitals in the system is contained in the expressions.

QUANTY uses a system based on this last notation to numerically represent arbitrary many-body wave functions by storing all non-vanishing coefficients and a descriptor identifying the corresponding Slater-determinant basis functions.

2.2 Operators in second Quantisation

Expressing wave functions in terms of Slater-determinants has the advantage that their anti-symmetrisation is automatically included, but explicitly calculating matrix elements of operators with a spatial dependence becomes tediously cumbersome. To greatly simplify these calculations, creation and annihilation operators are introduced.

The creation operator a_k^\dagger is interpreted to add a particle in orbital χ_k to the system, such that²⁰

$$a_k^\dagger |j_1, \dots, j_F\rangle \propto \begin{cases} |j_1, \dots, j_F, k\rangle & , k \notin \{j_1, \dots, j_F\} \\ 0 & , k \in \{j_1, \dots, j_F\} \end{cases} . \quad (2.6)$$

Analogously, a_k removes a particle from χ_k ,

$$a_k |j_1, \dots, j_F\rangle \propto \begin{cases} 0 & , k \notin \{j_1, \dots, j_F\} \\ |j_1, \dots, j_{l-1}, j_{l+1}, \dots, j_F\rangle & , k = j_l \end{cases} . \quad (2.7)$$

Because a and a^\dagger do not conserve the number of particles in a state, they do not act on the Hilbert space \mathbb{H}^F with F fermionic particles as defined in equation (2.1), but rather on the Fock space given by the direct sum²⁰

$$\mathbb{F} \stackrel{\text{def}}{=} \bigoplus_F \mathbb{H}_\phi^F , \quad a : \mathbb{H}_\phi^F \rightarrow \mathbb{H}_\phi^{F-1} , \quad a^\dagger : \mathbb{H}_\phi^F \rightarrow \mathbb{H}_\phi^{F+1} .$$

As any Slater-determinant can be written as

$$|j_1, \dots, j_F\rangle = \prod_{k \in \{j_l\}} a_k^\dagger |0\rangle \quad (2.8)$$

with $|0\rangle$ the Slater-determinant with no electrons, the operators inherit the antisymmetry relations characteristic of fermions,

$$a_j^\dagger a_k^\dagger = -a_k^\dagger a_j^\dagger , \quad a_j a_k = -a_k a_j . \quad (2.9)$$

Together with²⁰

$$a_j a_k^\dagger + a_k^\dagger a_j = \delta_{j,k} \quad (2.10)$$

all algebraic properties of the operators and their effects on all basis states are known, which is sufficient for their implementation in QUANTY.

Any one-particle operator corresponding to a measurable quantity needs to be of the form

$$\mathcal{O}(\vec{r}_1, \vec{p}_1, \vec{r}_2, \vec{p}_2, \dots) = \sum_j \mathcal{O}(\vec{r}_j, \vec{p}_j) = \sum_j \mathcal{O}_j \quad , \quad (2.11)$$

where \mathcal{O}_j depends only on position \vec{r}_j and momentum \vec{p}_j of the j^{th} particle. The sum takes their indistinguishability into account.

Its representation in second quantisation, which is here denoted by omitting the position and momentum dependence, is defined as²⁰

$$\mathcal{O} = \sum_{k,l} \langle k | \mathcal{O} | l \rangle a_k^\dagger a_l = \sum_{k,l} a_k^\dagger a_l \int_{\mathbb{R}^3} \bar{\chi}_k(\vec{r}) \mathcal{O}(\vec{r}, \vec{p}) \chi_l(\vec{r}) d\vec{r} \quad , \quad (2.12)$$

because it then acts on the one-particle Hilbert space in exactly the same way,

$$\begin{aligned} \langle m | \mathcal{O} | n \rangle &= \sum_{k,l} \langle m | a_k^\dagger a_l | n \rangle \int_{\mathbb{R}^3} \bar{\chi}_k(\vec{r}) \mathcal{O}(\vec{r}, \vec{p}) \chi_l(\vec{r}) d\vec{r} \quad (2.13) \\ &= \sum_{k,l} \delta_{m,k} \delta_{l,n} \int_{\mathbb{R}^3} \bar{\chi}_k(\vec{r}) \mathcal{O}(\vec{r}, \vec{p}) \chi_l(\vec{r}) d\vec{r} \\ &= \int_{\mathbb{R}^3} \bar{\chi}_m(\vec{r}) \mathcal{O}(\vec{r}, \vec{p}) \chi_n(\vec{r}) d\vec{r} \quad . \end{aligned}$$

An analogous expression exists for two-particle operators,

$$\mathcal{O} = \sum_{\substack{k < l \\ m < n}} a_m^\dagger a_n^\dagger a_l a_k \int_{\mathbb{R}^6} \bar{\chi}_k(\vec{r}) \bar{\chi}_l(\vec{r}') \mathcal{O}(\vec{r}, \vec{p}, \vec{r}', \vec{p}') \chi_m(\vec{r}') \chi_n(\vec{r}) d\vec{r} d\vec{r}' \quad . \quad (2.14)$$

For one-particle orbitals that resemble atomic orbitals in that they are comprised of a radial part multiplied with a spherical harmonic function, QUANTY has the second quantisation form of many operators included in its implementation.

2.3 Lánczos Algorithm and Krylov Basis

One of the most important features of QUANTY is its implementation of the Lánczos algorithm.⁴⁶ Because it is the basis of almost all calculations done for this work it is described here in some detail. The algorithm has a normal incarnation and a block-version. The latter is described in this section, since the former can be considered the special case of 1×1 matrices.

For a Hilbert space \mathbb{H} and any Hermitian operator $\mathcal{O} : \mathbb{H} \rightarrow \mathbb{H}$ the Lánczos algorithm as it is implemented by QUANTY is defined as follows:

1. Pick an orthonormal set of starting vectors $\Psi_0 \subset \mathbb{H}$ with entries $\psi_{0,j}$. Furthermore pick a maximum number of iteration steps N .
2. Define the auxiliary set Ψ_1^x with $\#\Psi_1^x = \#\Psi_0$ and with elements

$$\psi_{1,j}^x \stackrel{\text{def}}{=} \mathcal{O}\psi_{0,j} - \sum_k \psi_{0,k} \langle \psi_{0,k} | \mathcal{O} | \psi_{0,j} \rangle \quad . \quad (2.15)$$

3. Orthogonalise the set with the Löwdin procedure:⁴⁸

Define the overlap matrix $(L_1)_{j,k} \stackrel{\text{def}}{=} \langle \psi_{1,j}^x | \psi_{1,k}^x \rangle$ and diagonalise it so that $L_1 = T_1 D_1 T_1^\dagger$, with the block matrix and row vector

$$D_1 \stackrel{\text{def}}{=} \begin{pmatrix} \Lambda_1 & 0 \\ 0 & 0 \end{pmatrix} \quad \text{and} \quad T_1 \stackrel{\text{def}}{=} (T_{1,\Lambda} \quad T_{1,0}) \quad . \quad (2.16)$$

Here Λ_1 denotes a diagonal matrix containing all non-vanishing eigenvalues of L_1 .

Define the orthonormal set Ψ_1 with elements*

$$\psi_{1,j} \stackrel{\text{def}}{=} \sum_k \psi_{1,k}^x (T_1')_{k,j} \quad , \quad \text{where} \quad T_1' \stackrel{\text{def}}{=} T_{1,\Lambda} \Lambda_1^{-\frac{1}{2}} T_{1,\Lambda}^\dagger \quad . \quad (2.17)$$

4. Define the next auxiliary set Ψ_{i+1}^x with $\#\Psi_{i+1}^x = \#\Psi_i$ and with elements

$$\begin{aligned} \psi_{i+1,j}^x \stackrel{\text{def}}{=} & \mathcal{O}\psi_{i,j} - \sum_k \psi_{i,k} \langle \psi_{i,k} | \mathcal{O} | \psi_{i,j} \rangle \\ & - \sum_k \psi_{i-1,k} \langle \psi_{i-1,k} | \mathcal{O} | \psi_{i,j} \rangle \quad . \end{aligned} \quad (2.18)$$

*Note that it is possible that $\#\Psi_1 < \#\Psi_0$. If $\#\Psi_1 = 0$ the algorithm has found an invariant subset, but this is very unlikely to happen.

5. Find Ψ_{i+1} by orthonormalising Ψ_{i+1}^x as in step 3 with $1 \mapsto i + 1$.
6. Repeat steps 3-5 for all $i < N$.

In the non-block-version of the Lánczos algorithm steps 3 and 5 become a simple normalisation.

Once the procedure has terminated, a basis $\Psi \stackrel{\text{def}}{=} \bigcup_{i=0}^N \Psi_i$ spanning a subspace of the full Hilbert space is found. Because every iteration applies the operator \mathcal{O} to the vectors that were already found (compare step 4), the space spanned by Ψ is the order- N Krylov subspace of \mathcal{O} , and the set is therefore called ‘Krylov basis’.⁴⁴

The orthonormality of Ψ justifying the word ‘basis’ can be seen as follows: First consider two states $\psi_{i,j}$ and $\psi_{i,k}$ from the same block Ψ_i that has no vanishing eigenvalues in the overlap matrix L_i , meaning that $T_i = T_{i,\Lambda}$. This set can always be constructed by removing vectors until Ψ_i is linearly independent. The i index is temporarily suppressed for simplicity. The overlap between two entries of Ψ is then given by*

$$\begin{aligned} \langle \psi_j | \psi_k \rangle &= \sum_{l,m} \overline{T'_{l,j}} \underbrace{\langle \psi_l^x | \psi_m^x \rangle}_{=L_{l,m}} T'_{m,k} = (T_\Lambda \Lambda^{-\frac{1}{2}} \underbrace{T_\Lambda^\dagger L T_\Lambda}_{=\Lambda} \Lambda^{-\frac{1}{2}} T_\Lambda^\dagger)_{j,k} \quad (2.19) \\ &= (T_\Lambda T_\Lambda^\dagger)_{j,k} = \delta_{j,k} \quad . \end{aligned}$$

This is merely a proof that the Löwdin procedure orthonormalises a linearly independent set.

For any two vectors $\psi_{0,j} \in \Psi_0$ and $\psi_{1,l}^x \in \Psi_1^x$ the equation

$$\langle \psi_{0,j} | \psi_{1,l}^x \rangle = \langle \psi_{0,j} | \mathcal{O} | \psi_{0,l} \rangle - \sum_k \underbrace{\langle \psi_{0,j} | \psi_{0,k} \rangle}_{=\delta_{j,k}} \langle \psi_{0,k} | \mathcal{O} | \psi_{0,l} \rangle = 0 \quad (2.20)$$

holds, as Ψ_0 was assumed to be orthonormal. Since this is also true for any superposition of $\psi_{1,l}^x$,

$$\langle \psi_{0,j} | \psi_{1,l} \rangle = 0 \quad \forall \psi_{1,l} \in \Psi_1 \quad . \quad (2.21)$$

Analogously it follows that if all vectors in all subsets up to a certain Ψ_i are orthonormal to one another, then they are also orthonormal to all vectors in Ψ_{i+1} . The orthonormality of Ψ follows per induction.

*Note that L_i in step 3 is Hermitian, therefore its eigenvalues Λ_i are real, and hence T_i' is Hermitian as well.

Using the definition of step 4 the matrix form O of the operator \mathcal{O} can be studied. Consider $i \geq k$, then

$$\begin{aligned} \langle \psi_{i,j} | \mathcal{O} | \psi_{k,l} \rangle &= \langle \psi_{i,j} | \psi_{k+1,l}^x \rangle + \sum_m \langle \psi_{i,j} | \psi_{k,m} \rangle \langle \psi_{k,m} | \mathcal{O} | \psi_{k,l} \rangle \\ &+ \sum_m \langle \psi_{i,j} | \psi_{k-1,m} \rangle \langle \psi_{k-1,m} | \mathcal{O} | \psi_{k,l} \rangle . \end{aligned} \quad (2.22)$$

Using the orthonormality of the states it follows that

$$\begin{aligned} \langle \psi_{i,j} | \mathcal{O} | \psi_{k,l} \rangle &= \sum_m \underbrace{\langle \psi_{i,j} | \psi_{k+1,m} \rangle}_{=\delta_{i,k+1}\delta_{j,m}} (T'_{k+1})_{m,l} \\ &+ \sum_m \underbrace{\langle \psi_{i,j} | \psi_{k,m} \rangle}_{=\delta_{i,k}\delta_{j,m}} \langle \psi_{k,m} | \mathcal{O} | \psi_{k,l} \rangle \\ &+ \sum_m \underbrace{\langle \psi_{i,j} | \psi_{k-1,m} \rangle}_{=\delta_{i,k-1}\delta_{j,m}} \langle \psi_{k-1,m} | \mathcal{O} | \psi_{k,l} \rangle , \end{aligned} \quad (2.23)$$

which gives*

$$\begin{aligned} \langle \psi_{i,j} | \mathcal{O} | \psi_{k,l} \rangle &= \delta_{i,k} \underbrace{\langle \psi_{k,j} | \mathcal{O} | \psi_{k,l} \rangle}_{\stackrel{\text{def}}{=} (A_k)_{j,l}} \\ &+ \delta_{i,k-1} \underbrace{\langle \psi_{k-1,j} | \mathcal{O} | \psi_{k,l} \rangle}_{\stackrel{\text{def}}{=} (B_k)_{j,l}} + \delta_{i,k+1} \underbrace{(T'_{k+1})_{j,l}}_{\stackrel{\text{def}}{=} (B_{k+1})_{j,l}} . \end{aligned} \quad (2.24)$$

It follows that O has the block-tri-diagonal form

$$O = \begin{pmatrix} A_0 & B_1 & 0 & 0 & \ddots \\ B_1 & A_1 & B_2 & 0 & \ddots \\ 0 & B_2 & A_3 & B_3 & \ddots \\ 0 & 0 & B_3 & A_4 & \ddots \\ \ddots & \ddots & \ddots & \ddots & \ddots \end{pmatrix} . \quad (2.25)$$

Physically, this implies that Ψ_n are the states that are coupled to Ψ_0 by the operator \mathcal{O} at n^{th} order. If $\mathcal{O} = \mathcal{H}$ represents the Hamiltonian of the system, the states are

*The Hermiticity of the operator \mathcal{O} implies the Hermiticity of its matrix form O . It follows that $\langle \psi_{k-1,j} | \mathcal{O} | \psi_{k,l} \rangle = (B_k)_{j,l} = (T'_k)_{j,l}$.

sorted by their importance for the dynamics of Ψ_0 . It is hence straightforward to find a less computationally expensive approximation by truncating the basis set at some appropriate length N .

Some of the numerous applications of the Lánczos algorithm are discussed in section 4.

3 Processing DFT Results

The entity describing the dynamics of a quantum mechanical system is the Hamiltonian. The DFT code FPLO described in section 1.2 provides the Hamiltonian \mathcal{H}_{DFT} of equation (1.7) as its output, which describes the system on a mean field level. This section explains how to get from this one-particle operator to the many-body Hamiltonian that describes the system well enough whilst keeping the Hilbert space from becoming too large.

3.1 Active Space Atomic-like Orbitals

Since DFT is, in its implementation, a one-particle mean field theory, it does not run into the exponential wall. DFT codes thus often use very large one-particle basis sets with up to thousands of orbitals. Because the aim of this section is to transition from that to a many-body picture, using the full basis as a starting point is not an option.

For that reason one picks an energy window $[E_{lower}, E_{upper}]$ on which the calculation and all relevant physical processes take place, and cuts out all other orbitals, keeping their occupation either filled or empty. This splits the basis of DFT eigenorbitals into three parts, called

$$\left\{ \begin{array}{ll} \text{‘passive unoccupied shells’} & , \quad E > E_{upper} \\ \text{‘active space’} & , \quad E \in [E_{lower}, E_{upper}] \\ \text{‘passive core shells’} & , \quad E < E_{lower} \end{array} \right. .$$

Focusing only on the active space does, depending on the energy window, greatly reduce the size of the basis, without having a noticeable impact on the results.

In the cases considered in this thesis there is often an open (i.e. neither filled nor empty) d or f shell present, which can not be properly treated on a mean field level and which often turns out to be of great importance for the results of the calculation. This shell is henceforth called the ‘main shell’. To retain some degree of intuition regarding it, it is desirable to find a basis for the active space of the crystal

or molecule system in which the first n orbitals are as close as possible to the n orbitals making up the main shell in the free atom.

It is furthermore desirable to have the basis orbitals be very localised, as this leads to more negligible elements in the Hamiltonian. Atomic-like orbitals fulfill this demand by construction, but they are potentially coupled to the passive shells. The procedure of choice therefore guarantees no coupling between active and passive shells, and results in basis orbitals for the active space that are as atomic-like as possible.²¹

The results of this reduction greatly depend on the choice of atomic orbitals of interest, and of the energy window. They have to be picked such that diagonalising the effective Hamiltonian on the active space leads to bands (or energy levels in case of a molecule) that each coincide with one of the bands of the full system.

The reduction to the active space is implemented in FPLO, where it is called ‘downfolding’, which is explained here.

By self-consistently solving the Kohn-Sham equations, FPLO finds the Bloch functions $|B_l^{\vec{k}}\rangle$ as the eigenfunctions to the Kohn-Sham Hamiltonian, where \vec{k} is a vector in reciprocal space. To find localised orbitals it combines them to Wannier functions, which are defined as⁷⁹

$$|W_j^{\vec{R}}\rangle \stackrel{\text{def}}{=} \sum_{\vec{k}, l} |B_l^{\vec{k}}\rangle U_{l,j}^{\vec{k}} e^{-i\vec{k}\cdot\vec{R}} \quad , \quad (3.1)$$

with \vec{R} a vector in real space around which the wave function is centered.

However, this definition has some freedom in form of the unitary transformation $U_{j,l}^{\vec{k}}$, the choice of which determines the form and localisation of $|W_j^{\vec{R}}\rangle$.

The procedure used in FPLO is outlined in ref. [21]. First, a set $|A_m^{\vec{R}}\rangle$ of atomic-like functions (which are a subset of the basis used by FPLO) centered around positions \vec{R} and with quantum numbers m are defined. With the help of these a set of auxiliary functions $|X_m^{\vec{k}}\rangle$ is found via*

$$|X_m^{\vec{k}}\rangle \stackrel{\text{def}}{=} \sum_l |B_l^{\vec{k}}\rangle h_m^{\vec{R}}(E_l^{\vec{k}}) \langle B_l^{\vec{k}} | A_m^{\vec{R}} \rangle \quad , \quad (3.2)$$

where $E_l^{\vec{k}}$ is the energy of the Bloch function and $h_m^{\vec{R}}$ a window function, i.e. a function with a compact carrier, on which it mostly takes the value 1 and falls off exponentially or as a step function towards the border of the active space.

*In ref. [21] the sum symbol is erroneously missing.

The orbitals $|X_m^{\vec{k}}\rangle$ are, in general, not orthogonal, which is remedied by the Löwdin⁴⁸ procedure*

$$|Y_j^{\vec{k}}\rangle \stackrel{\text{def}}{=} \sum_m |X_m^{\vec{k}}\rangle \left((L^{\vec{k}})^{-\frac{1}{2}} \right)_{m,j} , \quad (3.3)$$

with $L_{m,j}^{\vec{k}} \stackrel{\text{def}}{=} \langle X_m^{\vec{k}} | X_j^{\vec{k}} \rangle$. If any eigenvalue of $L^{\vec{k}}$ vanishes the process terminates with an error at this step.

FPLO chooses

$$U_{l,j}^{\vec{k}} = \sum_m h_m^{\vec{R}} (E_l^{\vec{k}}) \langle B_l^{\vec{k}} | A_m^{\vec{R}} \rangle \left((L^{\vec{k}})^{-\frac{1}{2}} \right)_{m,j} \quad (3.4)$$

in equation (3.1), meaning that

$$\begin{aligned} |W_j^{\vec{R}}\rangle &= \sum_{\vec{k},l} \sum_m |B_l^{\vec{k}}\rangle h_m^{\vec{R}} (E_l^{\vec{k}}) \langle B_l^{\vec{k}} | A_m^{\vec{R}} \rangle \left((L^{\vec{k}})^{-\frac{1}{2}} \right)_{m,j} e^{-i\vec{k}\cdot\vec{R}} \\ &= \sum_{\vec{k}} \sum_m |X_m^{\vec{k}}\rangle \left((L^{\vec{k}})^{-\frac{1}{2}} \right)_{m,j} e^{-i\vec{k}\cdot\vec{R}} = \sum_{\vec{k}} |Y_j^{\vec{k}}\rangle e^{-i\vec{k}\cdot\vec{R}} . \end{aligned} \quad (3.5)$$

This choice guarantees the orthonormality of the Wannier functions, because

$$\begin{aligned} \langle W_j^{\vec{R}} | W_l^{\vec{R}'} \rangle &= \sum_{\vec{k},\vec{k}'} e^{i\vec{k}\cdot\vec{R}} e^{-i\vec{k}'\cdot\vec{R}'} \underbrace{\langle Y_j^{\vec{k}} | Y_l^{\vec{k}'} \rangle}_{\delta_{\vec{k},\vec{k}'}\delta_{j,l}} \\ &= \sum_{\vec{k}} e^{i\vec{k}\cdot(\vec{R}-\vec{R}')} \delta_{j,l} = \delta_{\vec{R},\vec{R}'} \delta_{j,l} . \end{aligned} \quad (3.6)$$

After the procedure is completed, FPLO prints out the matrix elements of the Kohn-Sham Hamiltonian \mathcal{H}_{DFT} (compare equation (1.7)) in this basis.

3.2 Rotation to a convenient Space

Once the steps of section 3.1 are completed a matrix form H_{DFT} of the one-particle DFT Hamiltonian \mathcal{H}_{DFT} is found, with one part of the matrix describing the ‘main’

*Compare section 2.3 for a short proof that this orthonormalises the vectors.

shell on a mean field level. As the aim is to go beyond DFT, Coulomb interaction is added to that shell later on (compare section 3.3). This elevates the Hamiltonian to a many-body operator, leading to more realistic results, but also scaling the computation cost exponentially with the number of fermionic states, which corresponds to the size of the one-particle basis. To be able to do calculations despite this exponential wall, clever rotations combined with truncations are utilised to minimise the size of the Hilbert space. Which one of the following techniques is used depends on the system of interest.

Crystal Field Theory

The eigenorbitals of a single atom are well approximated by a radial part times a spherical harmonic function $Y_l^{l_z}(\theta, \phi)$. They are eigenfunctions to the Hamiltonian, the angular momentum operator, as well as to the operator of the z-component of angular momentum. To first order the energy depends only on l .

Any chemical environment necessarily breaks the isotropic symmetry of a single atom. This also breaks the degeneracy of the orbitals with the same quantum number l , as the overlap for some orbitals with the electrons from the neighbouring atoms is larger than for others. The atomic orbitals expressed in spherical harmonics are then no longer eigenfunctions of the Hamiltonian, but rather have to be linearly recombined such that they can be written as a radial part times a (real valued) tesseral harmonic function $Z_l^m(\theta, \phi)$.

In Crystal Field Theory (abbr. ‘CFT’) only the shells of the main atom are included in the calculation, and the breaking of the degeneracies is the only effect that the chemical environment has on the system.^{5,74} Which of the shells experiences a splitting can be found from symmetry considerations. Alternatively, the splitting is automatically included in the effective Hamiltonian of a DFT calculation (compare section 3.1).

Most compounds encountered in nature have octahedral symmetry, where the main atom has six equidistant neighbours with right angles to one another, which form the tips of an octahedron (compare for example figure 6.1). The 5 orbitals of a shell with d character (ignoring spin) in octahedral symmetry split into a threefold degenerate lower energy level labelled t_{2g} , and a twofold degenerate higher energy level called e_g . Their energy difference is historically called $10Dq$.⁶³

This local CFT approximation is often able to reproduce many properties of the system, such that in some cases (compare section 6) no further refinements of the theoretical description of the Hamiltonian are necessary.

Ligand Field Theory

When hopping to or from the neighbouring sites of the main atom is relevant, Ligand Field Theory (abbr. ‘LFT’) becomes the tool of choice. Here the filled shells of the neighbouring atoms that have the most overlap with the main shell are included in the basis, so that the DFT Hamiltonian includes the hopping parameters between them.

Depending on the symmetry of the system not all of the (in principle arbitrarily many) ligand states have an overlap with the main shell, and not all of these overlaps are large. To reduce the system to the most important ones a block Lánczos algorithm as described in section 2.3 is applied to H_{DFT} , with the orbitals of the main shell as the starting set Ψ_0 . The result is a basis in which the matrix form of the Hamiltonian is block-tri-diagonal, meaning that only the orbitals described by the set Ψ_1 interact with the main shell directly.

In Ligand Field Theory the basis is reduced to $\Psi_0 \cup \Psi_1$, meaning that the number of fermionic states is at most twice as large as the size of the main shell. For core level spectroscopy an additional core shell of the main atom is also added to the system.

3.3 Adding Interaction

Most parts of the systems considered in this work are sufficiently well described by mean field theory. The main shell, however, is usually not. Here the full Coulomb interaction

$$Q^M = \frac{1}{2} \sum_{i,j,k,l} Q_{i,j,k,l}^M a_i^\dagger a_j^\dagger a_l a_k \quad (3.7)$$

is added to the Hamiltonian. If the aim of the calculation is to calculate the X-ray absorption spectrum, the Coulomb interaction between the main shell and a core shell is usually added as well, as it is crucial for correctly reproducing experimentally observed multiplet structures and branching ratios.

Atomic one-particle orbitals are given by a radial part times a spherical harmonic. For atomic-like orbitals this still holds approximatively. In order to find the coefficients $Q_{i,j,k,l}^M$ on a many-body basis built from these orbitals equation (2.14) is used and the Coulomb interaction is expanded in spherical harmonics. This way the spherical integrals contained in

$$Q_{i,j,k,l}^M = \langle i, j | Q^M | k, l \rangle \quad (3.8)$$

turn into a sum of analytical Slater integrals, and the radial integrals become the Coulomb integrals⁷²

$$R_{ijkl}^{(k)} = e^2 \iint_0^\infty \frac{\min(r_1, r_2)^k}{\max(r_1, r_2)^{k+1}} R_i(r_1) R_j(r_2) R_k(r_1) R_l(r_2) r_1^2 r_2^2 dr_1 dr_2 \quad . \quad (3.9)$$

These can be solved numerically using the radial functions R_i obtained from the output of a DFT calculation.

Since the main shell Coulomb interaction is already included in the Density Functional Theory calculation on a mean field level the mean field version Q_{MF}^M of the operator needs to be subtracted in order to avoid doubly counting it. It is calculated following the Hartree-Fock scheme⁵²

$$\begin{aligned} a_i^\dagger a_j^\dagger a_k a_l \rightarrow & -a_i^\dagger a_k \langle a_j^\dagger a_l \rangle + a_i^\dagger a_l \langle a_j^\dagger a_k \rangle + a_j^\dagger a_k \langle a_i^\dagger a_l \rangle \\ & - a_j^\dagger a_l \langle a_i^\dagger a_k \rangle - \langle a_i^\dagger a_l \rangle \langle a_j^\dagger a_k \rangle + \langle a_i^\dagger a_k \rangle \langle a_j^\dagger a_l \rangle \quad . \end{aligned} \quad (3.10)$$

Because any electron in Density Functional Theory interacts not only with the electron density of all other electrons, but also with its own, an additional self interaction term $Q_{MF,SI}^M$ needs to be added. It is approximated by

$$Q_{MF,SI}^M = \sum_i^{N_M-1} \bar{Q} \langle a_i^\dagger a_i \rangle a_i^\dagger a_i \quad , \quad (3.11)$$

where N_M is the number of fermionic one-particle states in the main shell and \bar{Q} is defined as the average Coulomb interaction strength given by

$$\bar{Q} \stackrel{\text{def}}{=} \frac{2}{N_M(N_M-1)} \sum_{j,k=0}^{N_M-1} (Q_{jkkj}^M - Q_{jkjk}^M) \quad . \quad (3.12)$$

3.4 The $U - \Delta$ Formalism

After applying the transformations of section 3.2 and section 3.3 the Hamiltonian has the form of an interacting Tight-Binding Operator. The one-particle onsite energy difference between main and ligand shell is often not correctly reproduced by the procedure. To correct this, several parameters usually called U and Δ are used and varied to fit the result to the experiment.⁸¹

A system described by Ligand Field Theory will, in its ground state, have a core shell \mathcal{C} filled with c electrons, and a main shell \mathcal{M} filled with m electrons

that is coupled to a Ligand shell \mathcal{L} with a filling of l . The configuration to energy assignments

$$E \stackrel{\text{def}}{=} \begin{cases} 0 & , & \mathcal{C}^c \mathcal{M}^m \mathcal{L}^l \\ \Delta_{\mathcal{C}\mathcal{M}} & , & \mathcal{C}^{c-1} \mathcal{M}^{m+1} \mathcal{L}^l \\ \Delta_{\mathcal{L}\mathcal{M}} & , & \mathcal{C}^c \mathcal{M}^{m+1} \mathcal{L}^{l-1} \end{cases} \quad (3.13)$$

are made.

Assuming that Coulomb interaction acts only on the main shell and between the main and core shell, these assignments lead to a set of equations featuring the (spherically averaged) Coulomb interaction strengths $U_{\mathcal{M}\mathcal{M}}$ and $U_{\mathcal{C}\mathcal{M}}$ and the corrected onsite energies ϵ :

$$0 = c\epsilon_{\mathcal{C}} + m\epsilon_{\mathcal{M}} + l\epsilon_{\mathcal{L}} \quad (3.14)$$

$$\begin{aligned} & + m(m-1) \frac{U_{\mathcal{M}\mathcal{M}}}{2} + mcU_{\mathcal{C}\mathcal{M}} \\ \Delta_{\mathcal{C}\mathcal{M}} = & (c-1)\epsilon_{\mathcal{C}} + (m+1)\epsilon_{\mathcal{M}} + l\epsilon_{\mathcal{L}} \end{aligned} \quad (3.15)$$

$$\begin{aligned} & + (m+1)m \frac{U_{\mathcal{M}\mathcal{M}}}{2} + (m+1)(c-1)U_{\mathcal{C}\mathcal{M}} \\ \Delta_{\mathcal{L}\mathcal{M}} = & c\epsilon_{\mathcal{C}} + (m+1)\epsilon_{\mathcal{M}} + (l-1)\epsilon_{\mathcal{L}} \end{aligned} \quad (3.16)$$

$$+ (m+1)m \frac{U_{\mathcal{M}\mathcal{M}}}{2} + (m+1)cU_{\mathcal{C}\mathcal{M}}$$

The three equations are solved by

$$\begin{aligned} \epsilon_{\mathcal{C}} = & \frac{m^2 (U_{\mathcal{M}\mathcal{M}} - 2U_{\mathcal{C}\mathcal{M}}) - 2l (U_{\mathcal{C}\mathcal{M}} - \Delta_{\mathcal{L}\mathcal{M}} + \Delta_{\mathcal{C}\mathcal{M}})}{2(c+m+l)} \\ & + \frac{m (U_{\mathcal{M}\mathcal{M}} - 2(U_{\mathcal{C}\mathcal{M}} + lU_{\mathcal{C}\mathcal{M}} + \Delta_{\mathcal{C}\mathcal{M}}))}{2(c+m+l)} , \end{aligned} \quad (3.17)$$

$$\begin{aligned} \epsilon_{\mathcal{M}} = & \frac{-m^2 U_{\mathcal{M}\mathcal{M}} + mU_{\mathcal{M}\mathcal{M}}(1-2l-2c) - 2c^2 U_{\mathcal{C}\mathcal{M}}}{2(c+m+l)} \\ & + \frac{2l\Delta_{\mathcal{L}\mathcal{M}} + 2c(U_{\mathcal{C}\mathcal{M}} - lU_{\mathcal{C}\mathcal{M}} + \Delta_{\mathcal{C}\mathcal{M}})}{2(c+m+l)} , \end{aligned} \quad (3.18)$$

$$\begin{aligned} \epsilon_{\mathcal{L}} = & \frac{m^2 U_{\mathcal{M}\mathcal{M}} + m(U_{\mathcal{M}\mathcal{M}} + 2cU_{\mathcal{C}\mathcal{M}} - 2\Delta_{\mathcal{L}\mathcal{M}})}{2(c+m+l)} \\ & + \frac{2c(U_{\mathcal{C}\mathcal{M}} - \Delta_{\mathcal{L}\mathcal{M}} + \Delta_{\mathcal{C}\mathcal{M}})}{2(c+m+l)} . \end{aligned} \quad (3.19)$$

The average onsite energies of the different shells are set to the corresponding values of ϵ . The parameters U and Δ are fitted for best agreement with the experiment.

If the system is described by Crystal Field Theory the onsite energies follow by setting $l = 0$,

$$\epsilon_C = \frac{\frac{m+m^2}{2} (U_{MM} - 2U_{CM}) - m\Delta_{CM}}{c+m} , \quad (3.20)$$

$$\epsilon_M = \frac{\frac{m-m^2}{2} U_{MM} + (c - c^2) U_{CM} + c (\Delta_{CM} - mU_{MM})}{c+m} . \quad (3.21)$$

4 Calculating physical Quantities

The result obtained after all appropriate steps described in section 3 are taken is a Hamiltonian operator that is as small as possible and as large as necessary to adequately describe the system of interest in a given spatial and energetic region. In short, a suitable and useful representation of the system is found.

The primary aim of many theoretical studies is to start from this description and calculate measurable quantities such as expectation values of Hermitian operators that can, in the best case, directly be compared to experimental results.

This section presents the most common quantities calculated for this work and briefly sketches how to obtain them using QUANTY.

4.1 Eigensystems

Due to the exponential wall it is in most cases virtually impossible to find the full eigensystem of a many-body Hamiltonian. However, for all practical purposes it is sufficient to approximately know the lowest N eigenvalues and the corresponding eigenstates. To find these QUANTY starts a block Lánczos algorithm (compare section 2.3) with N random states as a starting set Ψ_0 . As most Hamiltonians under consideration conserve the particle number, the states in Ψ_0 need to contain the correct amount of electrons. After $M - 1$ iteration steps the algorithm yields a block-tri-diagonal matrix with a dimension that is at most $(N \cdot M) \times (N \cdot M)$. QUANTY diagonalises this matrix, giving an approximation for the eigenvectors $|e_i\rangle$.

The programme then picks the N states with lowest energy and uses them as the starting set for a new Lánczos algorithm. It repeats to do so until the variance

$$\langle e_i | \mathcal{H}^2 | e_i \rangle - \langle e_i | \mathcal{H} | e_i \rangle^2, \quad (4.1)$$

which vanishes for a true eigenstate, is sufficiently small for all states $|e_i\rangle$ with $i \leq N$.

4.2 Spectra

The Hamiltonian describes the dynamics of the isolated system. A spectrum on the other hand describes how it can react to a disturbance, i.e. an effect that is not yet included in the effective description, such as an applied laser field or a spontaneous radioactive decay.

Let the unperturbed system be represented by the wave function $|\psi\rangle$ and the perturbation by an operator \mathcal{T} . The probability to find the perturbed system in the eigenstate $|E_j\rangle$ of the Hamiltonian \mathcal{H} is approximately given by the square of its overlap with $\mathcal{T}|\psi\rangle$. Because any closed system obeys energy conservation, this transition is only possible if the energy ω introduced to the system by the perturbation is equal to the difference between E_j and $E_0 \stackrel{\text{def}}{=} \langle\psi|\mathcal{H}|\psi\rangle$. The spectrum, which is defined as the probability density for the sum of all excitations, is thus given by

$$S(\omega) = \sum_j \delta(\omega - E_j + E_0) |\langle E_j|\mathcal{T}|\psi\rangle|^2 . \quad (4.2)$$

This is an incarnation of Fermi's Golden rule.¹⁶

The computationally more accessible response function defined as

$$\mathcal{G}(\omega) \stackrel{\text{def}}{=} \left\langle \psi \left| \mathcal{T}^\dagger \frac{1}{\omega - \mathcal{H} + E_0 + i0^+} \mathcal{T} \right| \psi \right\rangle , \quad (4.3)$$

where 0^+ denotes a positive infinitesimal number, contains the spectrum in its imaginary part. To see this, insert the completeness relation $\mathbb{1} = \sum_j |E_j\rangle \langle E_j|$ to find

$$\begin{aligned} \mathcal{G}(\omega) &= \left\langle \psi \left| \mathcal{T}^\dagger \frac{\sum_j |E_j\rangle \langle E_j|}{\omega - E_j + E_0 + i0^+} \mathcal{T} \right| \psi \right\rangle \\ &= \sum_j \frac{1}{\omega - E_j + E_0 + i0^+} |\langle E_j|\mathcal{T}|\psi\rangle|^2 . \end{aligned} \quad (4.4)$$

Using Plemelj's formula⁶⁶

$$\text{Im} \frac{1}{x + i0^+} = -\pi \delta(x) \quad (4.5)$$

directly shows that

$$-\text{Im} \frac{\mathcal{G}(\omega)}{\pi} = S(\omega) . \quad (4.6)$$

To actually compute a spectrum from equation (4.3), QUANTY applies a Lánczos algorithm (compare section 2.3) to the starting vector $\mathcal{T}|\psi\rangle$ with the operator \mathcal{H} , and thus finds an approximate eigensystem $\left\{ \left| E_j^{appr} \right\rangle \right\}$. This alone is insufficient, because in reality the Hamiltonian has uncountably many eigenstates in a finite energy interval, leading to a continuous spectrum rather than a discrete collection of δ -peaks. To approximate this, a finite number of eigenstates and -values is computed, and the infinitesimal quantity 0^+ in equation (4.3) replaced by a larger number Γ , transforming the δ -peaks to broadened Lorentzian curves. The value* of Γ is usually obtained from experimental measurements.

4.3 Self-energies

In section 4.2 the broadening of the spectrum was introduced as a fit parameter. A from the theorist's point of view more satisfactory, but also computationally more demanding approach is the self-energy formalism (compare ref. [10]).

Broadening occurring in reality is lost because the model Hamiltonian purposefully cannot reach all multi-particle states, but only a reasonably small subspace spanned for example by the eigensystem $\{|E_j\rangle\}$. This set can formally be extended to the orthonormal basis

$$\{|B_j\rangle\} \stackrel{\text{def}}{=} \{|E_j\rangle\} \cup \{|C_j\rangle\} \quad , \quad (4.7)$$

where $\{|C_j\rangle\}$ are those states that can be accessed from $\{|E_j\rangle\}$ via a so far neglected correction \mathcal{U} to the Hamiltonian.[†]

Inserting the (approximate) completeness relation for the reachable eigensystem into equation (4.3) twice, and replacing \mathcal{H} with the expanded Hamiltonian \mathcal{H}_x gives

$$\mathcal{G}(\omega) = \sum_{j,k} \left\langle \psi \left| \mathcal{T}^\dagger |E_j\rangle \langle E_j| \frac{1}{\omega - \mathcal{H}_x + E_0 + i0^+} |E_k\rangle \langle E_k| \mathcal{T} \right| \psi \right\rangle \quad . \quad (4.8)$$

*or values, $\Gamma = \Gamma(\omega)$ can be energy dependent

[†]Depending on the form of \mathcal{U} it can be necessary to replace $|E_j\rangle$ with $|E_j\rangle \otimes |\psi_{C,0}\rangle$, where the second wave function denotes the initial state of a previously unreachable part of the Hilbert space. This replacement is implied in the notation.

The operator \mathcal{O} in the denominator expressed in the expanded basis is

$$\begin{aligned} \mathcal{O} = & \omega + E_0 + i0^+ - \sum_j |E_j\rangle E_j \langle E_j| - \sum_{j,k} |C_j\rangle H_{x,j,k} \langle C_k| \\ & + \sum_{j,k} |C_j\rangle U_{j,k} \langle E_k| + \sum_{j,k} |E_j\rangle U_{j,k}^\dagger \langle C_k| \quad , \end{aligned} \quad (4.9)$$

or, in block matrix form,

$$\mathcal{O} = \begin{pmatrix} (\omega + E_0 + i0^+) \mathbb{1} - \text{diag}(E_j) & U^\dagger \\ U & (\omega + E_0 + i0^+) \mathbb{1} - H_x \end{pmatrix} \quad . \quad (4.10)$$

The upper left element of the inverse of this matrix is given by⁸²

$$\left(O^{-1}\right)_{1,1} = \frac{1}{(\omega + E_0 + i0^+) \mathbb{1} - \text{diag}(E_j) - \Sigma(\omega)} \quad , \quad (4.11)$$

where the self-energy Σ is introduced as¹⁰

$$\begin{aligned} \Sigma_{j,k}(\omega) & \stackrel{\text{def}}{=} \left(U^\dagger \frac{1}{(\omega + E_0 + i0^+) \mathbb{1} - H_x} U \right)_{j,k} \\ & = \sum_{l,m} \langle E_j | \mathcal{U}^\dagger | C_l \rangle \langle C_l | \frac{1}{\omega + E_0 + i0^+ - \mathcal{H}_x} | C_m \rangle \langle C_m | \mathcal{U} | E_k \rangle \quad . \end{aligned} \quad (4.12)$$

Because

$$\langle E_m | \mathcal{U} | E_k \rangle = 0 \quad \forall m, k \quad (4.13)$$

by construction, the sums over all projectors $|C_{l/m}\rangle \langle C_{l/m}|$ on the newly introduced states in equation (4.12) can be replaced by the sums over the projectors $|B_{l/m}\rangle \langle B_{l/m}|$ on all basis states. According to the completeness relation these objects are unit operators, such that the self-energy becomes

$$\Sigma_{j,k}(\omega) = \left\langle E_j \left| \mathcal{U}^\dagger \frac{1}{\omega + E_0 + i0^+ - \mathcal{H}_x} \mathcal{U} \right| E_k \right\rangle \quad . \quad (4.14)$$

As the corrections made to the Hamiltonian can again not reach all possible states, 0^+ is replaced with a non-infinitesimal number Γ , so that

$$\Sigma_{j,k}(\omega) = \left\langle E_j \left| \mathcal{U}^\dagger \frac{1}{\omega + E_0 + i\Gamma - \mathcal{H}_x} \mathcal{U} \right| E_k \right\rangle \quad . \quad (4.15)$$

At first glance, one fit parameter is merely replaced by another, but it turns out that while Γ influences the shape of Σ to a significant degree, it has only a small to negligible effect on the response function \mathcal{G} , from which the spectrum is obtained.

Because section 4.15 has the exact same form as equation (4.3), it can be calculated using similar methods.

Since it is assumed that $\langle C_j | E_k \rangle = 0$ for all j and k , the upper left element is the only part of \mathcal{O}^{-1} that remains when plugging it back into equation (4.8), which now takes the form*

$$\mathcal{G}(\omega) = \sum_{j,k} \langle \psi | \mathcal{T}^\dagger | E_j \rangle \frac{1}{\omega - E_j \delta_{j,k} + E_0 - \Sigma_{j,k}(\omega)} \langle E_k | \mathcal{T} | \psi \rangle . \quad (4.16)$$

The imaginary part of $\Sigma_{j,k}$ thus broadens the spectrum obtained from \mathcal{G} , while the real part shifts its peaks. The self-energy furthermore has the potential to create interference between states $|E_{j/k}\rangle$ that would be orthogonal eigenstates of the Hamiltonian without the correction, giving rise to Fano's effect.²³

If several corrections $\mathcal{U}^{(1)}$, $\mathcal{U}^{(2)}$ to the Hamiltonian are implemented that lead to separated Hilbert spaces, then the cross terms arising in equation (4.15) vanish, so that

$$\Sigma(\omega) = \Sigma^{(1)}(\omega) + \Sigma^{(2)}(\omega) . \quad (4.17)$$

This makes it possible to treat corrections from unrelated phenomena independently from one another, as long as the same energy Gauge is used for all.

4.4 Time Evolutions

There are several ways to describe the time evolution of a physical system, two of which are used in this thesis. The first method involves a time dependent wave function, whose evolution is governed by the Schrödinger equation. This method has the advantage that the wave function at any time is known and can be used with QUANTY's functionality to calculate the system's spectrum. The second method is based on the many-particle density matrix, which evolves according to the von Neumann equation,⁷⁸ or, in its extended form, the GKSL equation.^{29,47} The latter allows to incorporate the effect of a decay mechanism.

*Since Σ has a non-infinitesimal, non-vanishing imaginary part, $i0^+$ can be neglected.

Time Evolutions of the Wave Function

The Schrödinger equation⁷⁰ for a Hamiltonian \mathcal{H} and a wave function ψ is given by*

$$\mathcal{H}(t)\psi(t) = i\partial_t\psi(t) = \lim_{d_t \rightarrow 0} i \frac{\psi(t + d_t) - \psi(t)}{d_t} . \quad (4.18)$$

For a time-independent Hamiltonian this differential equation is solved by

$$\psi(t) = e^{-i\mathcal{H}t}\psi(0) \quad (4.19)$$

for every time t . In the more general case $\mathcal{H} = \mathcal{H}(t)$ where the commutator $[\mathcal{H}(t_1), \mathcal{H}(t_2)]$ between the Hamiltonian at different times does not always vanish, the solution to equation (4.18) becomes the much more complicated expression¹⁷⁻¹⁹

$$\psi(t) = \mathcal{T}_{\mathcal{D}} e^{-i \int_0^t \mathcal{H}(t') dt'} \psi(0) . \quad (4.20)$$

Because it features the numerically rather inaccessible Dyson time ordering operator $\mathcal{T}_{\mathcal{D}}$, using equation (4.20) in calculations is not feasible. Instead, another formalism is needed.

After treating d_t in equation (4.18) as a non-vanishing entity for the moment, equation (4.18) becomes

$$\psi(t + d_t) = [\mathbb{1} - i\mathcal{H}(t)d_t] \psi(t) . \quad (4.21)$$

Iteratively applying this n times, this equation yields

$$\psi(t + nd_t) = \left(\prod_{j=1}^n \{ \mathbb{1} - i\mathcal{H}[t + (j-1)d_t]d_t \} \right) \psi(t) . \quad (4.22)$$

Now suppose that nd_t is significantly smaller than the timescale on which $\mathcal{H}(t)$ changes, so that $\mathcal{H}(t) \approx \text{const.}$ in this time period. The equation then simplifies to

$$\psi(t + nd_t) \approx (\mathbb{1} - i\mathcal{H}(t)d_t)^n \psi(t) . \quad (4.23)$$

Define $\Delta_t = nd_t$, so that $d_t = \frac{\Delta_t}{n}$ and

$$\psi(t + \Delta_t) \approx \left(\mathbb{1} - \frac{i\mathcal{H}(t)\Delta_t}{n} \right)^n \psi(t) . \quad (4.24)$$

Keeping Δ_t constant and sending $n \rightarrow \infty$ gives

$$\psi(t + \Delta_t) \approx e^{-i\mathcal{H}(t)\Delta_t} \psi(t) . \quad (4.25)$$

By applying this iteratively the wave function at any time t can be calculated.

* $\hbar = 1$

Time Evolutions of the Density

The von Neumann equation

The many-particle density matrix* ρ is defined as the sum of the projectors on states ψ_j with probabilities p_j ,⁷⁸

$$\rho \stackrel{\text{def}}{=} \sum_j p_j |\psi_j\rangle \langle \psi_j| \quad . \quad (4.26)$$

Using the Schrödinger equation (4.18) and its Hermitian conjugate one can find the time evolution to be given by the von Neumann equation⁷⁸

$$\begin{aligned} i \frac{\partial}{\partial t} \rho &= i \sum_j p_j ([\partial_t |\psi_j\rangle] \langle \psi_j| + |\psi_j\rangle [\partial_t \langle \psi_j|]) \\ &= \sum_j p_j [\mathcal{H}, |\psi_j\rangle \langle \psi_j|] = [\mathcal{H}, \rho] \quad . \end{aligned} \quad (4.27)$$

This also holds for time-dependent Hamiltonians.

The GKSL equation

If, however, the decay into the continuum is to be taken into account, then the von Neumann equation must be extended to become the GKSL equation, which was discovered by Vittorio Gorini, Andrzej Kossakowski and George Sudarshan,²⁹ and independently by Göran Lindblad.⁴⁷ Its derivation here roughly follows the review works refs. [7, 51, 64], with the difference that this work assumes a time-dependent Hamiltonian.

Suppose that a system can be divided into a part \mathcal{B} of bound states governed by the Hamiltonian $\mathcal{H}_{\mathcal{B}}(t)$, which is the main system of physical interest, and a continuum \mathcal{C} evolving according to $\mathcal{H}_{\mathcal{C}}$, to which electrons can be excited via some decay mechanism $\mathcal{H}_{\mathcal{BC}}$ that has a comparably small amplitude. This is the same setup as in section 4.3, where a self-energy was introduced to yield a correction of the spectrum. For the time evolution of a system under the influence of an environment a different formalism is required, which gives a correction to the von Neumann equation (4.27).

To develop this formalism a density operator $\rho_{\mathcal{B}}$ is needed that for every operator \mathcal{O} acting only on the subspace \mathcal{B} fulfils

$$\langle \mathcal{O} \rangle_{\mathcal{B}} = \text{Tr}(\mathcal{O} \cdot \rho_{\mathcal{B}}) \stackrel{!}{=} \text{Tr}(\mathcal{O} \otimes \mathbb{1}_{\mathcal{C}} \cdot \rho) = \langle \mathcal{O} \otimes \mathbb{1}_{\mathcal{C}} \rangle \quad , \quad (4.28)$$

*Not to be confused with the one-particle density matrix n .

as this requirement guarantees that physical quantities on \mathcal{B} remain unaffected by changing the description from ρ to ρ_B .

Let $\{b_j\}$ be a basis of \mathcal{B} and $\{c_l\}$ a basis of \mathcal{C} . Indirectly defining the partial trace of an operator $\rho : \mathcal{B} \otimes \mathcal{C} \rightarrow \mathcal{B} \otimes \mathcal{C}$ via

$$\langle b_j | \text{Tr}_{\mathcal{C}}(\rho) | b_k \rangle \stackrel{\text{def}}{=} \sum_l \langle b_j \otimes c_l | \rho | b_k \otimes c_l \rangle \quad (4.29)$$

and setting

$$\rho_B \stackrel{\text{def}}{=} \text{Tr}_{\mathcal{C}}(\rho) \quad (4.30)$$

satisfies equation (4.28), because

$$\begin{aligned} \text{Tr}(\mathcal{O} \otimes \mathbb{1}_{\mathcal{C}} \cdot \rho) &= \sum_{j,l} \langle b_j \otimes c_l | \mathcal{O} \otimes \mathbb{1}_{\mathcal{C}} \cdot \rho | b_j \otimes c_l \rangle \quad (4.31) \\ &= \sum_{j,l,m,n} \langle b_j \otimes c_l | \mathcal{O} \otimes \mathbb{1}_{\mathcal{C}} | b_m \otimes c_n \rangle \langle b_m \otimes c_n | \rho | b_j \otimes c_l \rangle \\ &= \sum_{j,l,m,n} \langle b_j | \mathcal{O} | b_m \rangle \delta_{l,n} \langle b_m \otimes c_n | \rho | b_j \otimes c_l \rangle \\ &= \sum_{j,m} \langle b_j | \mathcal{O} | b_m \rangle \sum_l \langle b_m \otimes c_l | \rho | b_j \otimes c_l \rangle \\ &= \sum_j \langle b_j | \mathcal{O} \cdot \rho_B | b_j \rangle = \text{Tr}(\mathcal{O} \cdot \rho_B) \quad . \end{aligned}$$

To find the equation of motion for ρ_B it is helpful to express everything in the interaction picture with \mathcal{H}_{BC} defined as the interaction. Any operator is transformed according to

$$\mathcal{O}^I \stackrel{\text{def}}{=} U_{t_0,t}^\dagger \mathcal{O} U_{t_0,t} \quad , \quad (4.32)$$

where $U_{t_0,t}$ is the unitary time evolution of $\mathcal{H} - \mathcal{H}_{BC}$. Since \mathcal{H}_B and therefore \mathcal{H} explicitly depend on time, the evolution is formally given by¹⁷⁻¹⁹

$$U_{t_0,t} = \mathcal{T}_{\mathcal{D}} e^{-i \int_{t_0}^t [\mathcal{H}(t') - \mathcal{H}_{BC}] dt'} \quad , \quad (4.33)$$

with the Dyson time ordering operator $\mathcal{T}_{\mathcal{D}}$. Per construction it fulfils the Schrödinger equation for the time evolution,

$$i \frac{\partial}{\partial t} U_{t_0,t} = [\mathcal{H}(t) - \mathcal{H}_{BC}] U_{t_0,t} \quad . \quad (4.34)$$

Note that since $\mathcal{H} - \mathcal{H}_{BC} = \mathcal{H}_B \otimes \mathbb{1}_C + \mathbb{1}_B \otimes \mathcal{H}_C$ factorises, so does

$$\begin{aligned} U_{t_0,t} &= \mathcal{T}_D e^{-i \int_{t_0}^t (\mathcal{H}_B \otimes \mathbb{1}_C + \mathbb{1}_B \otimes \mathcal{H}_C) dt'} \\ &= \mathcal{T}_D e^{-i \int_{t_0}^t (\mathcal{H}_B \otimes \mathbb{1}_C) dt'} \otimes \mathcal{T}_D e^{-i \int_{t_0}^t (\mathbb{1}_B \otimes \mathcal{H}_C) dt'} \\ &\stackrel{\text{def}}{=} U_{B,t_0,t} \otimes U_{C,t_0,t} \quad , \end{aligned} \quad (4.35)$$

with each part fulfilling

$$i \frac{\partial}{\partial t} U_{B/C,t_0,t} = \mathcal{H}_{B/C}(t) U_{B/C,t_0,t} \quad . \quad (4.36)$$

In the interaction picture the von Neumann equation (4.27) becomes (suppressing time arguments for the moment)

$$\begin{aligned} i \frac{\partial}{\partial t} \rho^I &= \left(\partial_t U^\dagger \right) \rho U + U^\dagger (\partial_t \rho) U + U^\dagger \rho (\partial_t U) \\ &= -U^\dagger (\mathcal{H} - \mathcal{H}_{BC}) \rho U + U^\dagger [\mathcal{H}, \rho] U + U^\dagger \rho (\mathcal{H} - \mathcal{H}_{BC}) U \\ &= U^\dagger ([\mathcal{H}, \rho] - [\mathcal{H} - \mathcal{H}_{BC}, \rho]) U = U^\dagger [\mathcal{H}_{BC}, \rho] U \\ &= U^\dagger \mathcal{H}_{BC} U U^\dagger \rho U - U^\dagger \rho U U^\dagger \mathcal{H}_{BC} U = [\mathcal{H}_{BC}^I, \rho^I] \quad . \end{aligned} \quad (4.37)$$

This equation is formally solved by

$$\rho^I(t) = \rho^I(t_0) - i \int_{t_0}^t [\mathcal{H}_{BC}^I(t'), \rho^I(t')] dt' \quad . \quad (4.38)$$

Plugging this solution back into equation (4.37) gives

$$\begin{aligned} \frac{\partial}{\partial t} \rho^I(t) &= -i \left[\mathcal{H}_{BC}^I(t), \rho^I(t_0) \right] \\ &\quad - \left[\mathcal{H}_{BC}^I(t), \int_{t_0}^t [\mathcal{H}_{BC}^I(t'), \rho^I(t')] dt' \right] \quad . \end{aligned} \quad (4.39)$$

Applying the partial trace to both sides of the equation leads to

$$\begin{aligned} \frac{\partial}{\partial t} \rho_B^I(t) &= -i \text{Tr}_C \left(\left[\mathcal{H}_{BC}^I(t), \rho^I(t_0) \right] \right) \\ &\quad - \text{Tr}_C \left(\left[\mathcal{H}_{BC}^I(t), \int_{t_0}^t [\mathcal{H}_{BC}^I(t'), \rho^I(t')] dt' \right] \right) \quad . \end{aligned} \quad (4.40)$$

To carry out the partial traces some approximations have to be made. Based on the assumption of a small coupling between B and C one can reason that

1. the density factorises, $\rho^I \approx \rho_B^I \otimes \rho_C^I$.
2. the continuum part of the density in the Schrödinger picture always remains in its ground state, $\rho_C(t) \approx \rho_C(t_0)$.
3. the continuum is empty, $\rho_C \approx |0\rangle\langle 0| \stackrel{\text{def}}{=} \rho_0$. Therefore

$$\rho_C^I(t) \approx U_{t_0,t}^\dagger |0\rangle\langle 0| U_{t_0,t} \stackrel{\text{def}}{=} \rho_0^I(t) \quad . \quad (4.41)$$

These approximations together lead to a new form of the time derivative of the density,

$$\begin{aligned} \frac{\partial}{\partial t} \rho_B^I(t) = & -i \text{Tr}_C \left(\left[\mathcal{H}_{BC}^I(t), \rho_B^I(t_0) \otimes \rho_0^I(t_0) \right] \right) \\ & - \int_{t_0}^t \text{Tr}_C \left(\left[\mathcal{H}_{BC}^I(t), \left[\mathcal{H}_{BC}^I(t'), \rho_B^I(t') \otimes \rho_0^I(t') \right] \right] \right) dt' \quad . \end{aligned} \quad (4.42)$$

To find a closed expression for ρ_B^I some further assumptions concerning the explicit form of the Hamiltonian have to be made, namely that

1. the coupling term can be written as

$$\begin{aligned} \mathcal{H}_{BC}^I(t) = & U_{t_0,t}^\dagger \sum_{\vec{j},k} \alpha_{\vec{j},k} \left(\sigma_{\vec{j}} \otimes a_k^\dagger + \sigma_{\vec{j}}^\dagger \otimes a_k \right) U_{t_0,t} \\ = & \sum_{\vec{j},k} \alpha_{\vec{j},k} \left(\sigma_{\vec{j}}^I(t) \otimes a_k^{\dagger I}(t) + \sigma_{\vec{j}}^{\dagger I}(t) \otimes a_k^I(t) \right) \quad , \end{aligned} \quad (4.43)$$

with \vec{j} a multi-index labeling bound states, $\sigma_{\vec{j}}$ acting on \mathcal{B} , a_k^\dagger creating an electron in the continuum \mathcal{C} and $\alpha_{\vec{j},k}$ a possibly vanishing factor.

2. the continuum part \mathcal{H}_C has no constant term and is particle number conserving*, meaning that

$$\begin{aligned} & \text{Tr}_C \left(\mathcal{O}_B^I(t_1) \otimes \mathcal{O}_C^I(t_1) \cdot \rho_B^I(t_2) \otimes \rho_0^I(t_2) \right) \\ = & \left\langle 0 \left| U_{C,t_1,t_2}^\dagger \mathcal{O}_C U_{C,t_1,t_2} \right| 0 \right\rangle \\ = & \begin{cases} 0 & \text{for } \mathcal{O}_C = a_k^\dagger, a_k, a_k^\dagger a_{k'} \\ \delta_{k,k'} & \text{for } \mathcal{O}_C = a_k a_{k'}^\dagger \end{cases} \quad . \end{aligned} \quad (4.44)$$

* Any constant terms can always be absorbed into \mathcal{H}_B , and, since the Hamiltonian only appears inside commutators and complex exponents, they cancel anyhow.

3. the continuum excitations are short lived, so that

$$\begin{aligned} \langle a_k^I(t_1) a_k^{\dagger I}(t_2) \rangle &= \langle 0 | U_{C,t_0,t_1}^\dagger a_k U_{C,t_2,t_1} a_k^\dagger U_{C,t_0,t_2} | 0 \rangle \\ &\approx \delta(t_2 - t_1) . \end{aligned} \quad (4.45)$$

It follows that the first term in equation (4.42) vanishes, as do many combinations in the second term. What remains is

$$\begin{aligned} \frac{\partial}{\partial t} \rho_B^I(t) &= - \int_{t_0}^t \sum_{\vec{j}, \vec{j}'} \sum_k \alpha_{\vec{j},k} \alpha_{\vec{j}',k} \sigma_{\vec{j}}^{\dagger I}(t) \sigma_{\vec{j}'}^I(t') \rho_B^I(t') \delta(t - t') dt' \\ &+ \int_{t_0}^t \sum_{\vec{j}, \vec{j}'} \sum_k \alpha_{\vec{j},k} \alpha_{\vec{j}',k} \sigma_{\vec{j}}^{\dagger I}(t) \rho_B^I(t') \sigma_{\vec{j}'}^I(t') \delta(t - t') dt' \\ &+ \int_{t_0}^t \sum_{\vec{j}, \vec{j}'} \sum_k \alpha_{\vec{j},k} \alpha_{\vec{j}',k} \sigma_{\vec{j}}^{\dagger I}(t') \rho_B^I(t') \sigma_{\vec{j}'}^I(t) \delta(t - t') dt' \\ &- \int_{t_0}^t \sum_{\vec{j}, \vec{j}'} \sum_k \alpha_{\vec{j},k} \alpha_{\vec{j}',k} \rho_B^I(t') \sigma_{\vec{j}'}^{\dagger I}(t') \sigma_{\vec{j}}^I(t) \delta(t - t') dt' . \end{aligned} \quad (4.46)$$

Another helpful assumption is that only those terms significantly contribute which affect the same indices, such that all terms with $\vec{j} \neq \vec{j}'$ can be ignored. The decay strength γ_j for a given decay channel is then defined via

$$\sum_k \alpha_{j,k}^2 \stackrel{\text{def}}{=} 2\gamma_j \phi_j , \quad (4.47)$$

where the function ϕ evaluated at \vec{j} gives 1 if \vec{j} describes a physically meaningful combination of indices, and 0 if it does not.* Now all sums and integrals can be evaluated, giving†

$$\begin{aligned} \frac{\partial}{\partial t} \rho_B^I(t) &= \sum_{\vec{j}} \gamma_{\vec{j}} \phi_{\vec{j}} \left(2\sigma_{\vec{j}}^{\dagger I}(t) \rho_B^I(t) \sigma_{\vec{j}}^I(t) - \left\{ \sigma_{\vec{j}}^{\dagger I}(t) \sigma_{\vec{j}}^I(t), \rho_B^I(t) \right\} \right) \\ &= U_{B,t_0,t}^\dagger \sum_{\vec{j}} \gamma_{\vec{j}} \phi_{\vec{j}} \left(2\sigma_{\vec{j}}^{\dagger} \rho_B(t) \sigma_{\vec{j}} - \left\{ \sigma_{\vec{j}}^{\dagger} \sigma_{\vec{j}}, \rho_B(t) \right\} \right) U_{B,t_0,t} . \end{aligned} \quad (4.48)$$

*The values of \vec{j} that ϕ deems physically meaningful depend on the decay mechanism.

†Because of symmetry considerations $\int_{t_0}^t \delta(t - t') dt' = \frac{1}{2}$, which cancels the prefactor of γ .

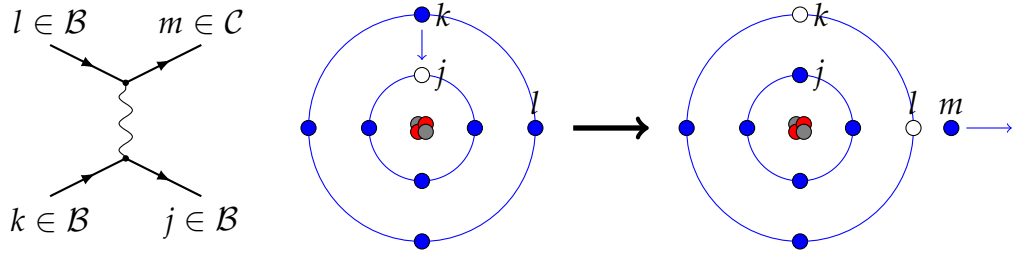


Figure 4.1: The Feynman diagram and a schematic representation of Auger-Meitner decay. The indices denote the part of the full system that the orbitals belong to.

To transform this back to the Schrödinger picture consider (suppressing time arguments for the moment)

$$\begin{aligned}
\partial_t \rho_B^l &= \left(\partial_t U_B^\dagger \right) \rho_B U_B + U_B^\dagger (\partial_t \rho_B) U_B + U_B^\dagger \rho_B (\partial_t U_B) \\
&= i U_B^\dagger \mathcal{H}_B \rho_B U_B + U_B^\dagger (\partial_t \rho_B) U_B - i U_B^\dagger \rho_B \mathcal{H}_B \partial_t U_B \\
&= U_B^\dagger (\partial_t \rho_B + i [\mathcal{H}_B, \rho_B]) U_B \quad ,
\end{aligned} \tag{4.49}$$

meaning that

$$\begin{aligned}
\frac{\partial}{\partial t} \rho_B(t) &= -i [\mathcal{H}_B(t), \rho_B(t)] \\
&\quad + \sum_{\vec{j}} \gamma_{\vec{j}} \phi_{\vec{j}} \left(2 \sigma_{\vec{j}}^\dagger \rho_B(t) \sigma_{\vec{j}} - \left\{ \sigma_{\vec{j}}^\dagger \sigma_{\vec{j}}, \rho_B(t) \right\} \right) \quad .
\end{aligned} \tag{4.50}$$

This is the GKSL equation for the many-particle density matrix of a system \mathcal{B} , dissipatively coupled to an empty continuum via a diagonal decay mechanism.

Auger-Meitner decay

The dissipation mechanism implemented in this work is Auger-Meitner decay, which was independently discovered by Lise Meitner⁵⁴ and Pierre Auger.⁴ It describes an electron in the state k decaying to fill a core hole j and donating its energy to an electron in state l which is then excited into the continuum state m . The Feynman diagram corresponding to this process is shown in figure 4.1, the operator is given by $\alpha_{j,k,l,m} a_m^\dagger a_j^\dagger a_k a_l$, where a_m^\dagger acts on the continuum part \mathcal{C} of the Hilbert space and the rest of the operator acts on the bound part \mathcal{B} . In the language

of the GKSL equation (4.50) this means that

$$\sigma_{j,k,l} = a_j^\dagger a_k a_l \quad . \quad (4.51)$$

The values of $\phi_{j,k,l}$ are defined by the fact that Auger-Meitner decay conserves total spin and total angular momentum, meaning that if for example two spin up electrons are annihilated then the new core electron must also have up spin.

Implementation

The numerical implementation of the time evolution happens by choosing a suitable basis and expressing all operators in it, so that QUANTY only has to handle matrices. To find this basis, the Lánczos algorithm is applied to the ground state $|\psi_0\rangle$, resulting in N_{Kry} Krylov states $\{|\psi_i\rangle\}$.

This basis covers the most important states reached by exciting the ground state. To also cover de-excitation, the states*

$$\mathcal{T} |\psi_i\rangle \quad \text{for } i \in [1, N_{Kry} - 1] \quad (4.52)$$

are added to the basis set, with the perturbation operator \mathcal{T} from equation (4.3).

If dissipation via Auger-Meitner decay is included in the calculation, the decayed states have to be reached as well. A further addition to the basis is therefore made by†

$$\sigma_{j,k,l} |\psi_i\rangle \quad \text{for } i \in [1, N_{Kry} - 1] \quad , \quad (j, k, l) : \phi_{j,k,l} = 1 \quad , \quad (4.53)$$

with the Lindblad operators $\sigma_{j,k,l}$ as defined in equation (4.51) and $\phi_{j,k,l}$ giving 1 if, and only if, the combination j, k, l describes a physically possible decay mechanism.

The function ϕ is further exploited in that only those combinations are allowed which result in a continuum electron with a z-projected angular momentum quantum number of $l_z = 0$. This is done purely to reduce the size of the Hilbert space, as the calculations become too cumbersome to handle otherwise.

Once the basis set is complete it is orthonormalised using the Gram-Schmidt procedure,^{30,69} which has the advantage that the ground state $|\psi_0\rangle$ is left unchanged. All operators of interest are then expressed in this basis.

At the beginning of the calculation the system is prepared in the ground state. If the time evolution is calculated using the wave function, the starting vector therefore

*Note that i begins at 1 instead of 0, because a state proportional to $\mathcal{T} |\psi_0\rangle$ is already contained in the Krylov basis.

†The index again begins at 1, because the ground state cannot decay.

has a 1 as its first entry and 0 everywhere else. Its time evolution is found by iteratively applying equation (4.25), which in this formalism becomes a multiplication of a matrix with a vector.

The resulting object can be transformed back to a many-body wave function $|\psi(t)\rangle$, which can be used to calculate time-dependent spectra (compare section 4.2). If several laser fields $\mathcal{T}_j(t)$ disturb the system, it is possible to explicitly and non-perturbatively include the effects of all but \mathcal{T}_{j_0} , the one making the excitation of interest, by adding them to the Hamiltonian,

$$\mathcal{H} \rightarrow \mathcal{H}(t) = \mathcal{H}_0 + \sum_{j \neq j_0} \mathcal{T}_j(t) \quad . \quad (4.54)$$

If on the other hand the many-particle density matrix is used as the quantity characterising the state of the system, the initial condition is a matrix with a 1 as its 1, 1 element and 0 everywhere else. Its evolution in time is then found by solving either equation (4.27) or, if decay is included, equation (4.50). Because these are differential equations for which no closed and simple form analogous to equation (4.25) is known they are solved for each time step using a RK4 Runge-Kutta method.^{45,67}

Part II
Applications

5 Nickel^{II}oxide

5.1 Motivation

Light offers one of the most versatile ways to interact with matter on an atomic level. Understanding the effects of this interaction and being able to calculate quantitative predictions is crucial not only for physical, chemical and biological experiments, but also for numerous technological applications.

The devices in development include photovoltaic cells and molecular machines. Both share that the incoming light induces a charge-transfer excitation, which then dissipates and transforms its energy either in an electric current or molecular motion.⁵³ Another remotely related application is that of qubits. Here a laser-induced spin-flip excitation is a promising candidate for storing information.³⁸

Because of their correlated behaviour and large spin-orbit coupling, transition metals exhibit complicated but also fast and rich dynamics. This makes them well suited as the active centres of proposed photon based technical applications.³⁷

Of all crystalline transition metal compounds Nickel^{II}oxide (abbr. ‘Ni^{II}O’) is among the most thoroughly studied. It was one of the earliest examples where band theory predicted a substance to be conducting, while experiment proved it to be insulating.^{14,58} Much research emphasizing the important role Coulomb interaction plays in transition metal compounds followed, which is why Ni^{II}O is still often used as the system to test theories on.³³

Both for charge-transfer and spin-flip excitations the dynamics play out on several different time-scales:⁷⁷

1. The initial excitation can happen on the order of a few hundred *as*.
2. The excited state usually relaxes to a lower excited state within a hundred *fs*.
3. The system thermally equilibrates in the following few *ps* in the case of a small molecule. It takes significantly longer for larger systems.

Parameter	Used Values
$E [V/a_B]$	380, 760, 1520, 3040
$\omega [eV]$	846.275
$\text{FWHM} = 2\sqrt{2 \ln 2} \sigma [as]$	100, 333, 1000, 3330

Table 5.1: The parameters used for the external Hamiltonian.

The last step can be tackled theoretically using for example linear response time-dependent Density Functional Theory.⁷³ Several experiments have utilised ultrafast spectroscopy to monitor the second step.^{12,38,57} A theoretical study of the dynamics of Ni^{II}O following a spin-flip excitation can be found in ref. [35]. There, the authors investigate the second step of the relaxation process by preparing the system in an excited state and letting it evolve according to the Schrödinger equation.

This section focuses on the first step. The Ni^{II}O system is modelled using several levels of theory. It is prepared in the ground state and the light is simulated as a time dependent perturbation of the Hamiltonian in form of an electric field. The effects of the model and the form of the light field on orbital, charge-transfer and spin-flip excitations are investigated. Furthermore, another set of calculations is presented in which the effect of Auger-Meitner decay on the dynamics is incorporated via the GKSL equation.

5.2 Two Level System

Theory

The full Hamiltonian \mathcal{H} is the sum of a time-independent part \mathcal{H}_0 describing the Nickel^{II}oxide system on a varying level of theory and an external, time-dependent part $\mathcal{H}_{ext}(t)$ describing the laser pulse.

The first level of theory is to approximate the Ni^{II}O crystal as a 2 level system. Here the states of the Ni-2*p* and Ni-3*d* shells are individually degenerate and separated by an energy difference Δ_ω . The Hamiltonian reads

$$\mathcal{H}_{0=} = \epsilon_p \mathcal{N}_p + \epsilon_d \mathcal{N}_d \quad , \quad (5.1)$$

with onsite energies ϵ , number operators \mathcal{N} , and $\epsilon_d - \epsilon_p = \Delta_\omega$. Applying a resonant sinusoidal electric field $E(t) = E_0 \sin(\Delta_\omega t)$ to the system would make the occupation oscillate between the two shells with the Rabi frequency $\omega_{Rabi} \propto E_0$.

Instead, the external part of the Hamiltonian is given by a transition operator multiplied by an oscillation enveloped by a Gaussian function. It reads

$$\mathcal{H}_{ext}(t) = E_0 \cos(\omega t) \exp\left(-\frac{t^2}{2\sigma^2}\right) (p_x d_x + p_y d_y + p_z d_z) \quad , \quad (5.2)$$

with the electric laser field strength E_0 , the laser frequency ω , a standard deviation of the pulse length σ (and thus a full width at half maximum (abbr. ‘FWHM’) of $2\sqrt{2 \ln 2} \sigma$), the three components of the normalised polarisation vector \vec{p} , and the three dipole operators d_x , d_y and d_z . Some of the parameters are varied throughout the calculations (compare table 5.1).

The time evolution of the system is calculated using the von Neumann equation (4.27). The numerical implementation of the time evolution is described in section 4.4.

To find results that can easily be compared to one another the width σ of the laser pulse is coupled to the electric field strength E such that their product is constant during a set of runs. This means that a lower coupling strength is applied over a longer period of time, leading to roughly the same number of oscillations in the partial occupation (see below). The symbol \mathbb{E} is defined as

$$\mathbb{E} \stackrel{\text{def}}{=} \text{FWHM} \cdot E_0 \quad , \quad (5.3)$$

and calculations are carried out for $\mathbb{E} = 100 \text{ as} \cdot 380 \text{ V}/a_B = 38 \text{ fVs}/a_B$, $76 \text{ fVs}/a_B$, $152 \text{ fVs}/a_B$ and $304 \text{ fVs}/a_B$.

Results

In order to present the results of the numerous calculations in an understandable fashion, the information is consistently encoded in the following ways: Black lines belong to calculations in which the full width at half maximum of the external electric field is 100 as , red lines to an FWHM of 333 as , orange lines to 1 fs and turquoise coloured lines to 3.33 fs . In composite figures with four panels the polarisation of the light is kept constant in the x -direction, the upper left panel shows the results for which $\mathbb{E} = 38 \text{ fVs}/a_B$, the upper right for $\mathbb{E} = 76 \text{ fVs}/a_B$, the lower left for $\mathbb{E} = 152 \text{ fVs}/a_B$ and the lower right for $\mathbb{E} = 304 \text{ fVs}/a_B$. Alternatively, \mathbb{E} is kept constant at $76 \text{ fVs}/a_B$ within a figure, in which case the upper left panel shows the result for light polarised in the $(1, 0, 0)$ -direction, the upper right for the $(0, 0, 1)$ -direction, the lower left for the $(1, 1, 0)$ -direction and the lower right for the $(1, 1, 2)$ -direction.

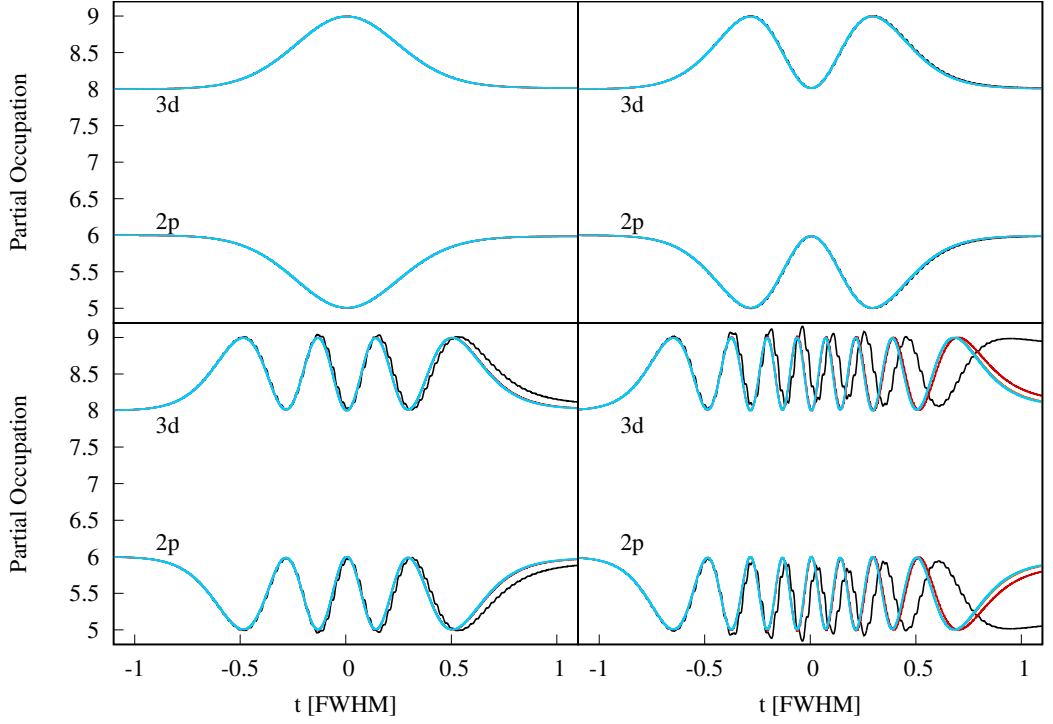


Figure 5.1: Partial occupations for the 2 state system, for polarisation in the x -direction and laser pulse FWHMs of 100 as (black lines), 333 as (red lines), 1 fs (orange lines) and 3.33 fs (turquoise lines). The values of \mathbb{E} are $38 fV_s/a_B$ (upper left), $76 fV_s/a_B$ (upper right), $152 fV_s/a_B$ (lower left) and $304 fV_s/a_B$ (lower right).

The time dependent partial occupations defined as

$$\sum_{j \in J} \langle a_j^\dagger a_j \rangle_t \quad (5.4)$$

for the indices J describing the shells Ni- $2p$ and Ni- $3d$ in the approximation of the 2 level system are shown in figure 5.1. In this simple model only an orbital excitation from the Ni- $2p$ to the Ni- $3d$ shell and back is possible.

Although the laser pulse is not a pure sinusoidal excitation but a sine multiplied with a Gaussian, the system behaves ‘Rabi-like’ for not too large electric field strengths (upper panels), meaning that the observed behavior is the same when FWHM of the laser pulse is changed but \mathbb{E} is kept constant. Only the time scale changes linearly with FWHM, as would be expected for a Rabi system. Because the

Parameter [eV]	2 Levels	CFT	LFT
ϵ_p	0	-683.467	-683.467
ϵ_d	846.175	134.190	134.190
ϵ_L	-	-	240.333
ζ_p	-	11.51	11.51
ζ_d	-	0.081	0.081
H	-	0.12	0.12
$10Dq_d$	-	1.1	0.56
$10Dq_L$	-	-	1.44
V_{t2g}	-	-	1.21
V_{eg}	-	-	2.06
γ	-	-	0, 1

Table 5.2: The parameters used for the different levels of theory, in units of eV.

time scale in figure 5.1 is given in units of FWHM, the lines lie almost perfectly on top of each other in the upper images.

The number of observed occupation peaks also doubles when doubling \mathbb{E} , as is expected.

At very high field strengths of about $1500 V/a_B$ and higher the scaling invariance breaks down, even for this simplified 2 level system (compare the black lines in the lower panels and the red line in the lower right panel of figure 5.1). In these cases the difference in amplitude between two neighbouring peaks in the laser is too large to locally approximate the signal as a sinusoidal wave. In case of the black lines the frequency of the external electric field can directly be observed as a small modulation of the line.

5.3 Crystal Field Theory

Theory

In Crystal Field Theory (abbr. ‘CFT’) the internal Hamiltonian is given by

$$\mathcal{H}_{0CFT} = \mathcal{H}_{0=} + \zeta_p \mathcal{C}_{ls,p} + \zeta_d \mathcal{C}_{ls,d} + \mathcal{Q} + HS_{112} + 10Dq_d \mathcal{C}_{CF,d} , \quad (5.5)$$

with $\mathcal{H}_{0=}$ given by equation (5.1), spin-orbit coupling parameters ζ and operators \mathcal{C}_{ls} , Coulomb interaction \mathcal{Q} on the $3d$ and between the $3d$ and $2p$ shells, an exchange

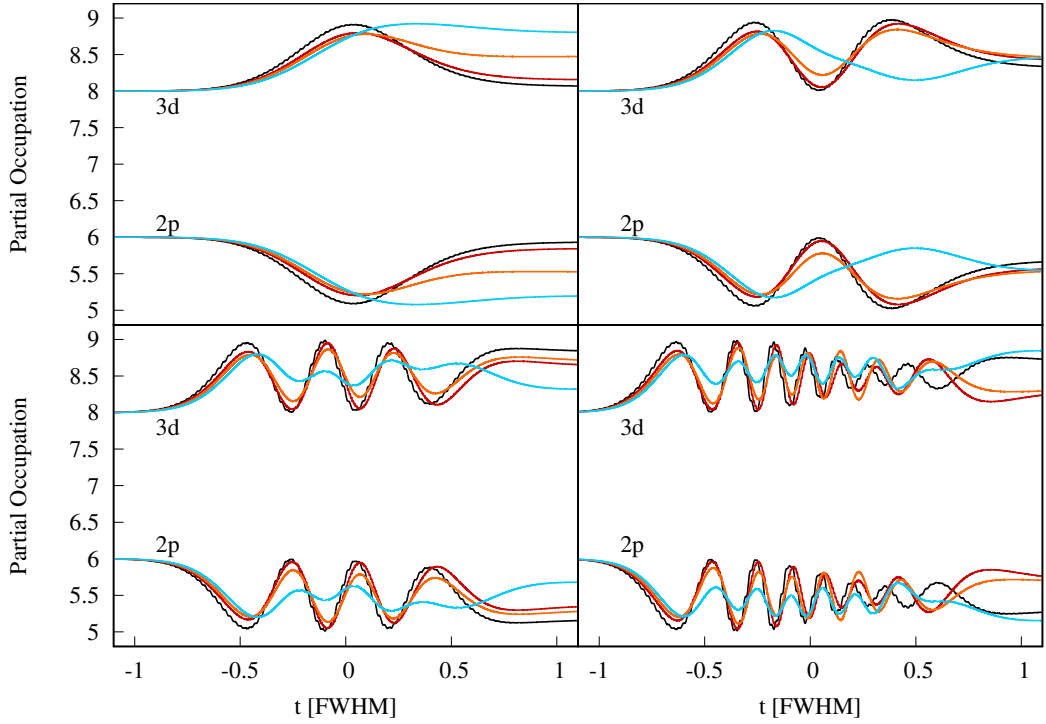


Figure 5.2: Partial occupations for Crystal Field Theory, for polarisation in the x -direction and laser pulse FWHMs of 100 as (black lines), 333 as (red lines), 1 fs (orange lines) and 3.33 fs (turquoise lines). The values of \mathbb{E} are $38 fV_s/a_B$ (upper left), $76 fV_s/a_B$ (upper right), $152 fV_s/a_B$ (lower left) and $304 fV_s/a_B$ (lower right).

field strength H coupled to the spin-operator \mathcal{S} oriented in the 112-direction, and the crystal field splitting parameter $10Dq$ coupled to a splitting \mathcal{C}_{CF} of the Ni-3d states due to the effects of the chemical environment. The parameters of $\mathcal{H}_{0=}$ differ from those used in the pure 2 level theory. They are given in table 5.2.

Results

In figure 5.2 the partial occupations for the Crystal Field Theory calculation are depicted. Since Coulomb interaction and other effects split the states into several multiplets, the behaviour is significantly different from the 2 level system. Yet, certain similarities can be observed.

For the shortest FWHM of 100 as (black lines) the behaviour of the 2 level sys-

tem is almost reproduced (compare figure 5.1), especially for lower field strengths (upper panels in figure 5.2). A doubling in field strength roughly doubles the number of cycles of orbital excitation and de-excitation, although some deviation can be observed, as the final occupation of the orbitals differs from the 2 level case.

Also with increasing initial field strength the time evolution becomes more asymmetric around the pulse maximum (which sits at $t = 0$), due to the fact that in contrast to the 2 level system there is no unique excitation energy any more, but a plethora of individual ones.

With increasing FWHM and thus decreasing maximum field strength the system's response seems to become slower, as the oscillations' peaks shift slightly to the right and the amplitudes decrease. Thus, the final occupation of the Ni-3d shell in case of $\mathbb{E} = 38 fV_s/a_B$ is almost 8 for the pulse with an FWHM of 100 *as* and close to 9 for the 3.33 *fs* pulse (compare black and turquoise lines in the upper left panel of figure 5.2), an effect that can not be observed in the 2 level system.

5.4 Ligand Field Theory

Theory

In Ligand Field Theory (abbr. 'LFT') the close chemical environment is added to the system, and can be excited to and from. The Hamiltonian is now given by

$$\mathcal{H}_{0LFT} = \mathcal{H}_{0CFT} + \epsilon_L \mathcal{N}_L + 10Dq_L \mathcal{C}_{CF,L} + V_{t2g} \mathcal{T}_{t2g} + V_{eg} \mathcal{T}_{eg} \quad , \quad (5.6)$$

with \mathcal{H}_{0CFT} given by equation (5.5) and hopping parameters V and operators \mathcal{T} . The parameters of \mathcal{H}_{0CFT} are again different from pure CFT (compare table 5.2).

Results

The Ligand Field Theory partial occupations, including that of the ligand, can be seen in figure 5.3. Due to the presence of the ligand shell the behaviour is even more distorted compared to the 2 level system. After the laser pulse excites the system it is, in general, not in an occupation eigenstate any more, leading to oscillations between the Ni-3d and the ligand shell. To make these charge transfer excitations visible the plots in figure 5.3 and in the following figures range from -1 to 2 FWHMs.

The occupation of the Ni-2p shell is not affected very much by the addition of the Ligand, instead the behaviour is very similar to that in Crystal Field Theory.

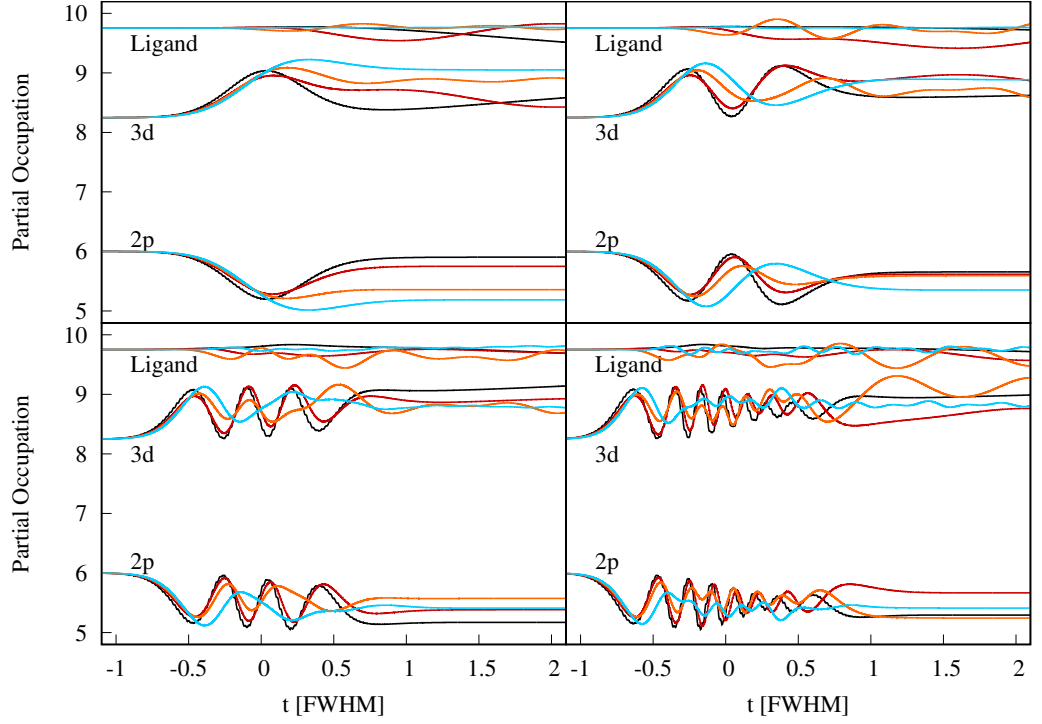


Figure 5.3: Partial occupations for Ligand Field Theory, for polarisation in the x -direction and laser pulse FWHMs of 100 as (black lines), 333 as (red lines), 1 fs (orange lines) and 3.33 fs (turquoise lines). The values of \mathbb{E} are $38 fV_s/a_B$ (upper left), $76 fV_s/a_B$ (upper right), $152 fV_s/a_B$ (lower left) and $304 fV_s/a_B$ (lower right).

Exceptions are large FWHMs of more than 1 fs and values of $\mathbb{E} \geq 152 fV_s/a_B$ (compare orange and turquoise lines in the lower panels of figure 5.3).

The Ni- $3d$ shell is affected in several ways: Due to hybridisation with the ligand shell its initial occupation is increased and during the de-excitation process some occupation of the ligand is excited to the Ni- $3d$ shell. As this charge transfer excitation only begins with the first excitation peak the effect is not very pronounced for $\mathbb{E} \geq 38 fV_s/a_B$. For larger values of \mathbb{E} most excitation seems to happen for an FWHM of 1 fs , but this might not be a trend. It is noteworthy that it takes comparably high field strengths of about $91 V/a_B$ to excite the system into the ligand shell using the pulse with FWHM of 3.33 fs , a behaviour that is explained below.

Because of the exchange field H pointing in the $(1, 1, 2)$ -direction the full Nickel^{II}oxide system has much lower symmetry than would be expected from the

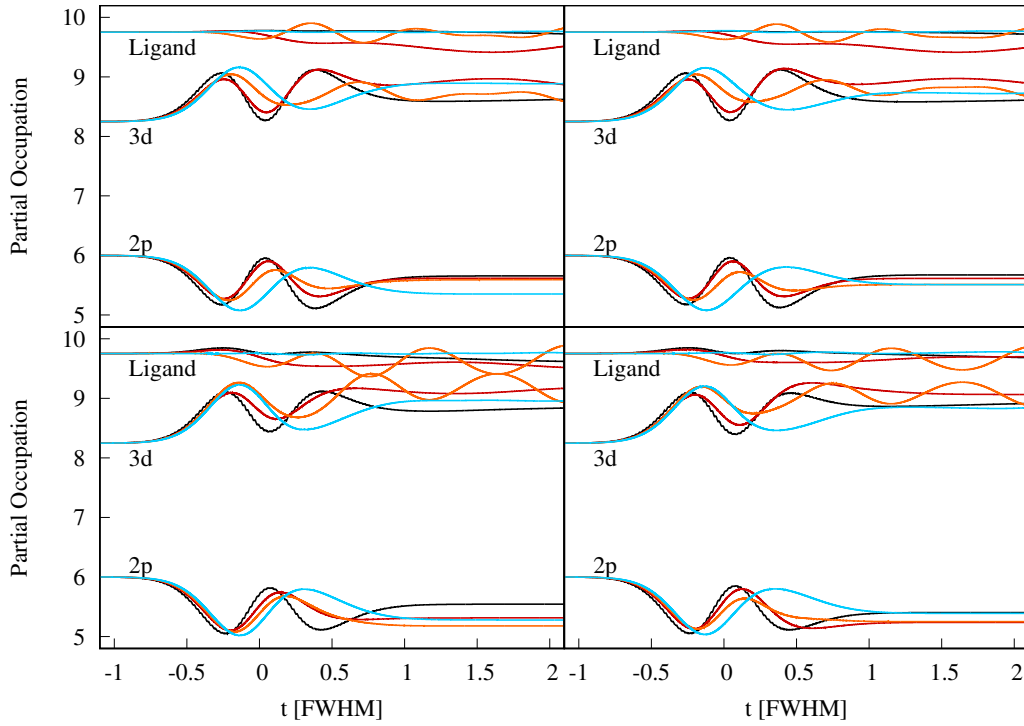


Figure 5.4: Partial Occupations for Ligand Field Theory, for polarisations in the $(1,0,0)$ -direction (upper left), $(0,0,1)$ -direction (upper right), $(1,1,0)$ -direction (lower left) and $(1,1,2)$ -direction (lower right). The laser pulse FWHMs are 100 as (black lines), 333 as (red lines), 1 fs (orange lines) and 3.33 fs (turquoise lines). All plots were created with $E = 76 fV_s/a_B$.

crystal structure alone. Therefore calculations for many laser polarisations can be of interest. Here the $(1,0,0)$ - or x -direction, the $(0,0,1)$ -, the $(1,1,0)$ - and the $(1,1,2)$ -direction are picked. The product of electric field maximum and FWHM is kept constant at $E = 76 fV_s/a_B$. The partial occupations for the corresponding Ligand Field Theory calculations are displayed in figure 5.4.

It is evident that the behaviour of the partial occupations for the x - and z -directions is very similar, as both laser polarisations point along a symmetry axis of the crystal. Only for the pulse with an FWHM of 3.33 fs a slight difference can be observed.

The charge transfer excitation is much more pronounced for polarisations in the $(1,1,0)$ - and $(1,1,2)$ -directions, except for the calculation with an FWHM of 3.33 fs . During the first occupation peak some electrons are even excited from the

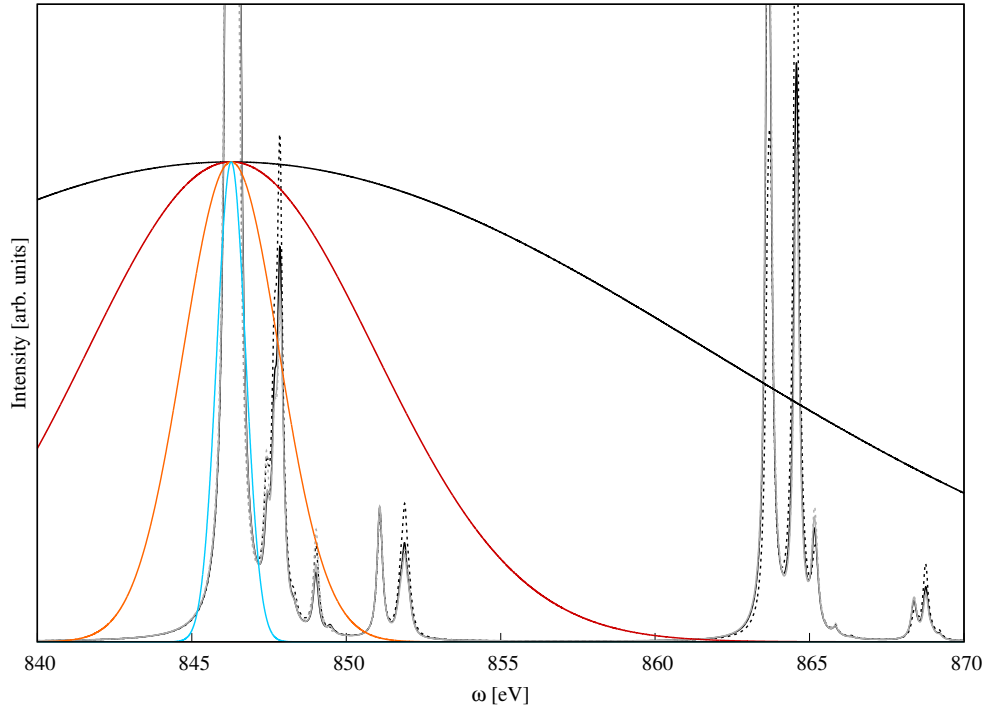


Figure 5.5: Spectra for light in the $(1,0,0)$ -direction (black solid line), the $(0,0,1)$ -direction (black dashed line), the $(1,1,0)$ -direction (grey solid line) and the $(1,1,2)$ -direction (grey dashed line). Also depicted are the Fourier-transforms of the laser pulses with FWHMs 100 as (black line), 333 as (red line), 1 fs (orange line) and 3.33 fs (turquoise line).

Ni- $3d$ shell to the ligand instead of the other way round, and for the calculation with an FWHM of 1 fs and light polarised in the $(1,1,0)$ -direction the Ni- $3d$ occupation exceeds the ligand occupation (compare the orange line in the lower left panel of figure 5.4).

Some of the dynamical behaviour of Nickel^{II}oxide can be predicted from its response function of equation (4.3), the negative imaginary part of which is the spectrum (compare section 4.2). Specifically the X-ray absorption spectrum (abbr. ‘XAS’) contains information about the system’s reaction to the simulated laser pulse. It is depicted in figure 5.5 for various polarisations.

All spectra are dominated by the large L3 edge, centred at 846.275 eV . At around 848 eV some Ni multiplet features are visible. The first peaks produced by ligand excitations sit at roughly 852 eV . The large L2 edge can be seen at approximately

864 eV, followed by two smaller ligand peaks at around 868 eV.

Also shown are the Fourier transforms of the laser pulses of different FWHMs (scaled such that their maxima are at the same value). A sinusoidal pulse would have a delta peak as its Fourier transform and would thus only excite at one given frequency. Any possible excitation that is not at that frequency will not contribute to the dynamics of the system because the effect of the external field is damped quickly by detuning. Due to the Gaussian envelope the laser pulses are composed of infinitely many frequencies, with prefactors falling off with the distance from the main frequency.

The Fourier transforms can therefore be used to predict which transitions a given laser pulse is likely to excite. In frequency space, the pulse with an FWHM of 3.33 fs has approximately no overlap with other peaks than the L3 edge main peak. It is thus expected to make no ligand excitations, as indeed noted before (compare the turquoise lines in figure 5.3). The peaks with FWHMs of 1 fs and 333 as are both expected to not excite to the L2 edge, and the latter should make more ligand excitations than the former. No restrictions can be made on the broad 100 as pulse.

However, the static spectrum together with the Fourier transformed laser pulses do not tell the full story. Once the laser starts exciting the system it is not in the ground state any more, and the Hamiltonian has changed. It subsequently has, in general, a different spectrum, possibly leading to other excitation amplitudes. Note, for example, that even though the overlap of the Fourier transform of the 1 fs pulse with the ligand peaks is small, it excites to them if the laser field strength is sufficiently high, as is evident from the orange lines in figure 5.3. The aforemade considerations also suggest that ligand excitations are the same for most pulses and a bit stronger for the (0, 0, 1)-direction, but figure 5.4 shows that they are strongest in case of the (1, 1, 0)-polarisation, at least for the laser pulse FWHM of 1 fs (orange lines). The explicit calculation of the time-evolution therefore clearly goes beyond the linear-response theory of spectra.

5.5 Ligand Field Theory with Auger-Meitner decay

Theory

The results presented so far are calculated for an idealised system from which electrons can not escape. In reality, however, the excited system can relax via Auger-Meitner decay, which intrinsically couples it to a continuum (see 4.1 for a graphical

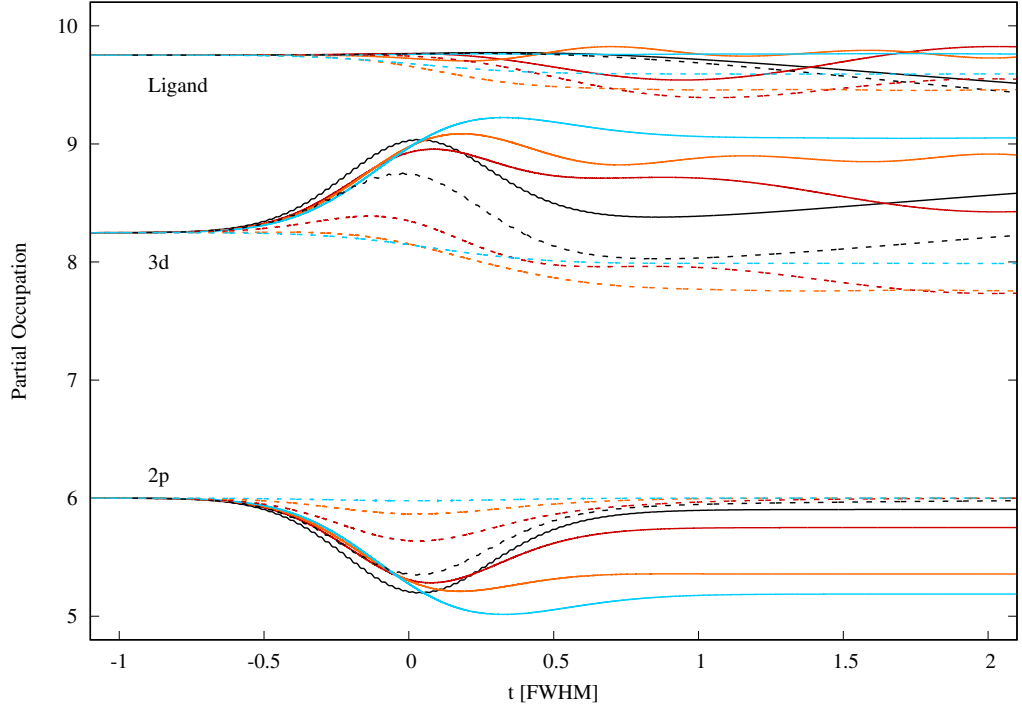


Figure 5.6: Partial occupations for Ligand Field Theory, for polarisation in the x -direction and laser pulse FWHMs of 100 as (black lines), 333 as (red lines), 1 fs (orange lines) and 3.33 fs (turquoise lines). All plots were created with $\mathbb{E} = 38 fV_s/a_B$.

depiction of the mechanism). The effects of this dissipation need to be taken into account in order to make reliable predictions.

To simulate this, the von Neumann equation (4.27) governing the time evolution is replaced by the GKSL equation (4.50). In this section, the decay strength γ is treated as a parameter and set to either 0 or 1 eV . It is assumed to be the same for all physically allowed decay channels.

Results

The partial occupations of the Ni- $2p$, Ni- $3d$ and ligand shell for values of \mathbb{E} of $38 fV_s/a_B$, $76 fV_s/a_B$, $152 fV_s/a_B$ and $304 fV_s/a_B$ are presented in figures 5.6, 5.7, 5.8 and 5.9, respectively. The results for the calculations including a decay strength of

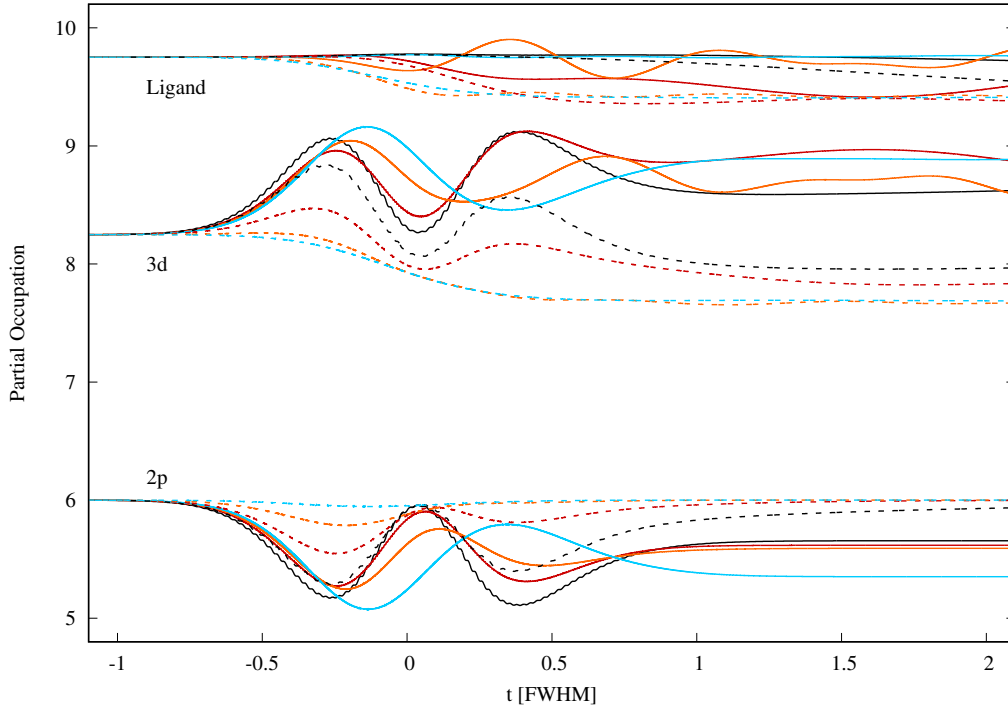


Figure 5.7: Partial occupations for Ligand Field Theory, for polarisation in the x -direction and laser pulse FWHMs of 100 as (black lines), 333 as (red lines), 1 fs (orange lines) and 3.33 fs (turquoise lines). All plots were created with $\mathbb{E} = 76 fV_s/a_B$.

$\gamma = 1 \text{ eV}$ are depicted with dashed lines, and those for calculations without decay are shown with solid lines for reference.

Because the decay strength, which implies a characteristic time scale, is kept constant throughout the calculations while the laser pulse length is not, it is expected that the role dissipation plays increases with the width of the pulse. This behaviour can best be observed in the Ni- $2p$ occupation for $\mathbb{E} = 38 fV_s/a_B$ (compare figure 5.6). While the population at time $t = 0$ is roughly the same for all pulse lengths for the non-decaying case, it gets closer to its initial value with increasing FWHMs if decay is considered. At an FWHM of 3.33 fs there is no oscillation visible any more. This shows that the orbital excitation is damped with increasing laser field strength.

The occupations of the other shells complete the picture. For FWHMs of 100 as

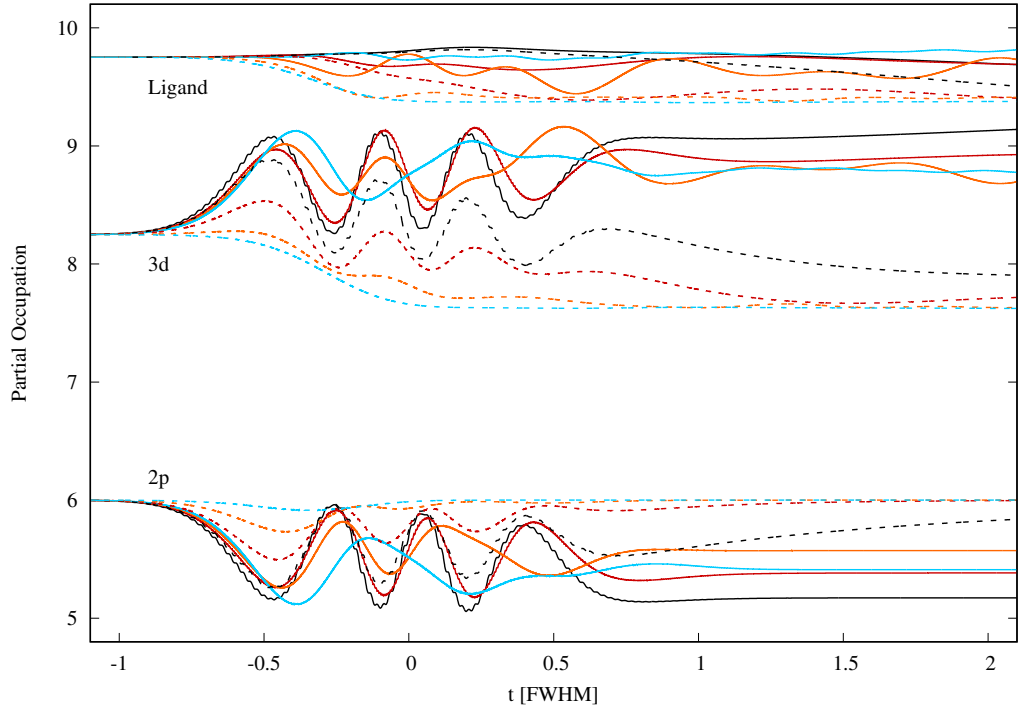


Figure 5.8: Partial occupations for Ligand Field Theory, for polarisation in the x -direction and laser pulse FWHMs of 100 as (black lines), 333 as (red lines), 1 fs (orange lines) and 3.33 fs (turquoise lines). All plots were created with $\mathbb{E} = 152 \text{ fVs}/a_B$.

and 333 as the occupation of the Ni- $3d$ shell increases, albeit significantly less than in the non-decaying case. The decay then lets it fall off lower than the initial occupation. In case of the longer pulses the population begins to decrease once the laser starts exciting electrons.

This lower population of the Ni- $3d$ orbitals increases the excitation rate from the ligand shell. For all FWHMs the ligand occupation begins to decrease earlier in case of decay than without, and ends at a lower value. This means that the charge transfer excitation is amplified by the inclusion of decay in the calculation, but there seems to be no dependence on the width of the laser pulse.

The decay also seems to suppress the after-pulse Ni- $3d$ -ligand oscillations. This does not mean, however, that the system is closer to an eigenstate of the occupation operators, because the decay of an excited state, which is a probabilistic process

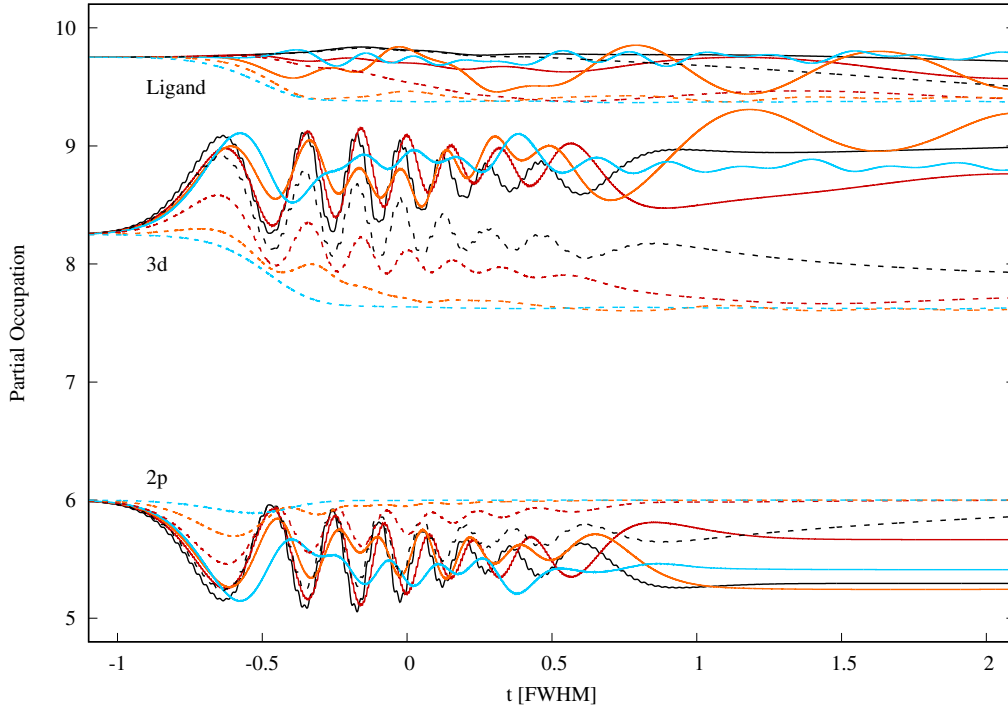


Figure 5.9: Partial occupations for Ligand Field Theory, for polarisation in the x -direction and laser pulse FWHMs of 100 as (black lines), 333 as (red lines), 1 fs (orange lines) and 3.33 fs (turquoise lines). All plots were created with $\mathbb{E} = 304 \text{ fVs}/a_B$.

happening at a random time, changes the system's density to that of a mixed state. This means that it can no longer be described by a single wave function, but by an ensemble of states.

Similar observations can be made when increasing the product of FWHM and laser field strength to $\mathbb{E} = 76 \text{ fVs}/a_B$ (compare figure 5.7). For FWHMs of 100 as and 333 as the Ni- $2p$ occupation features two minima, although the second minimum is significantly closer to the initial value than the first. For an FWHM of 1 fs the second minimum is not visible, and the curve of 3.33 fs is almost completely flat.

Again only the lower two values of FWHM manage to produce an increase in the Ni- $3d$ occupation, both show a smaller revival coinciding with the second Ni- $2p$ minimum. For the larger values of FWHM the occupation falls off in a very similar

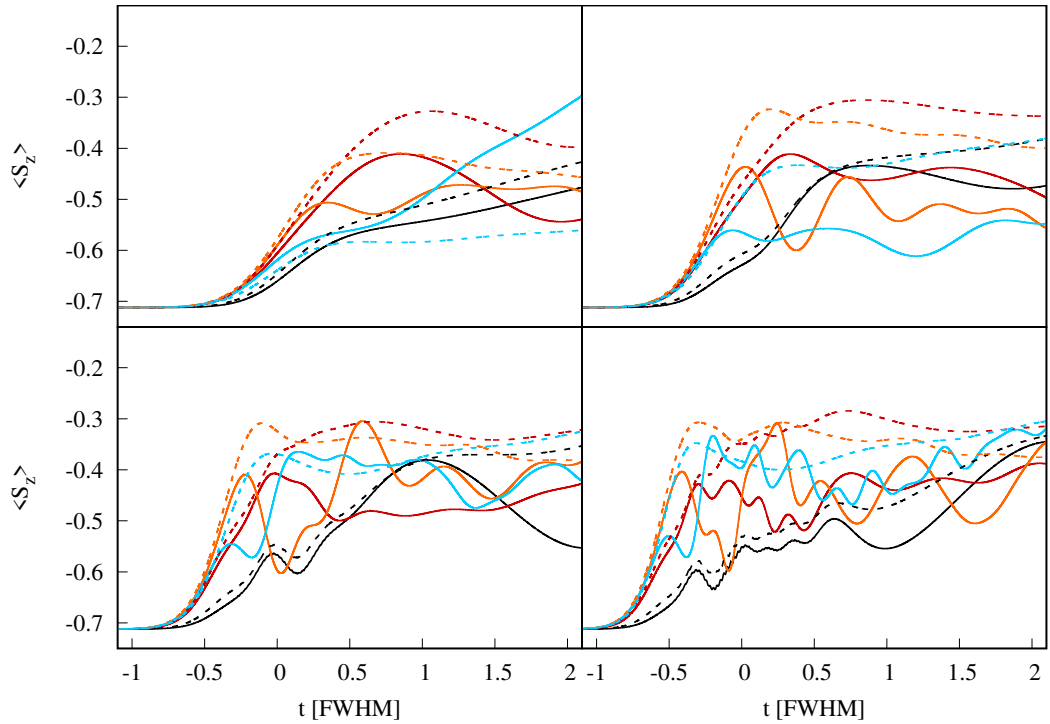


Figure 5.10: Spin in z -direction in units of $\hbar = 1$ for Ligand Field Theory, for polarisation in the x -direction and laser pulse FWHMs of 100 as (black lines), 333 as (red lines), 1 fs (orange lines) and 3.33 fs (turquoise lines). The values of \mathbb{E} are $38 fV_s/a_B$ (upper left), $76 fV_s/a_B$ (upper right), $152 fV_s/a_B$ (lower left) and $304 fV_s/a_B$ (lower right).

manner.

Doubling the laser field strength so that $\mathbb{E} = 152 fV_s/a_B$ changes some of this behaviour (compare figure 5.8). There is a small second and even smaller third oscillation maximum visible in the Ni- $3d$ occupation at an FWHM of 1 fs , and a single tiny minimum in the Ni- $2p$ occupation for the 3.33 fs pulse.

The Ni- $3d$ occupation quickly falls off to one less electron than the initial value in case of the pulse with an FWHM of 3.33 fs , and saturates there. This is most likely a computational artefact, because only states with up to one decayed electron were considered in the basis set in order to speed up calculations. In reality the final occupation would most likely be significantly lower than the calculated value.

The $\mathbb{E} = 304 fV_s/a_B$ calculations do not add much new information (compare figure 5.9). In case of the pulse with an FWHM of 1 fs there is a small excitation

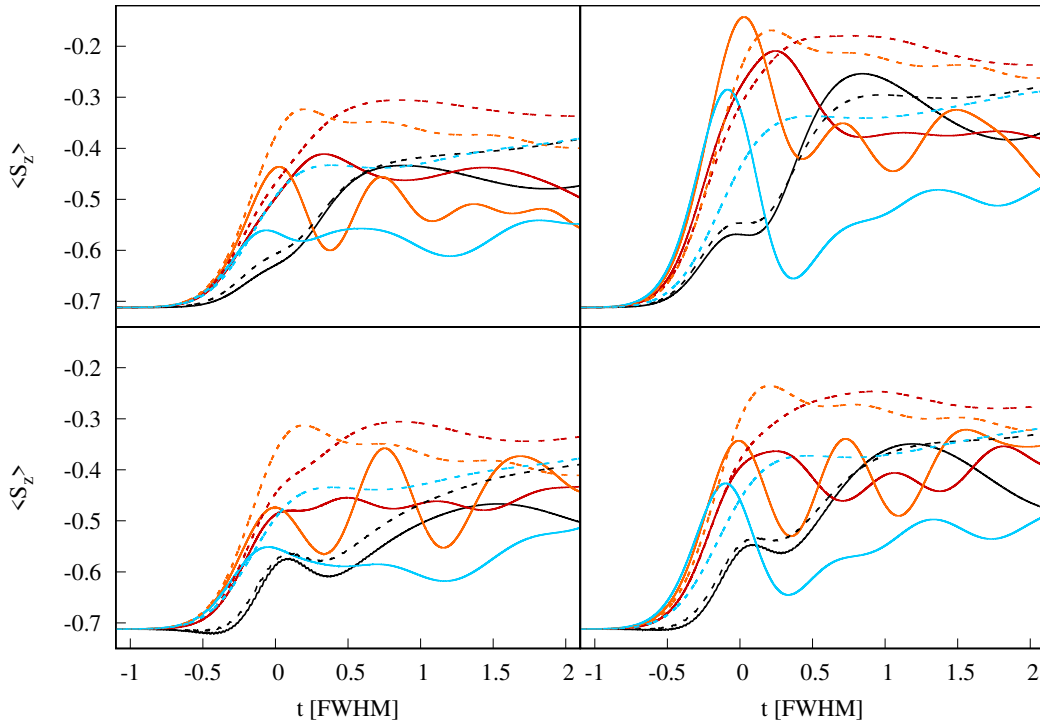


Figure 5.11: Spin in z-direction in units of $\hbar = 1$ for Ligand Field Theory, for polarisations in the (1,0,0)-direction (upper left), (0,0,1)-direction (upper right), (1,1,0)-direction (lower left) and (1,1,2)-direction (lower right). The laser pulse FWHMs are 100 as (black lines), 333 as (red lines), 1 fs (orange lines) and 3.33 fs (turquoise lines). All plots were created with $\mathbb{E} = 76 fV_s/a_B$.

into the Ni-3d shell at the beginning of the pulse, but it quickly falls to values lower than the initial value. Orbital excitations can therefore be forced by stronger laser fields, even for long pulses. For all practical applications, however, it is safe to say that orbital excitations do not happen for pulse FWHMs larger than about 500 as.

The expectation value of the z-component of the system's spin is displayed in figure 5.10 for different values of \mathbb{E} . The system starts off in a polarised state, with $\langle S_z \rangle \approx -0.7$, the absolute value of which is then decreased once the laser starts exciting the system*. At some point the trend reverses, and the absolute value of $\langle S_z \rangle$ begins to oscillate, usually about a value of roughly -0.5 . The absolute value never reaches 0. The time when this oscillation begins happens earlier (in terms

*Note that $\hbar = 1$ in the unit system used here, meaning that $\langle S_z \rangle$ has units of 1.

of FWHM) the longer the laser pulse is, suggesting that this is related to a system-internal time-scale.

After the excitation by the laser the system is, in general, not in an Eigenstate anymore, which can lead to spin precessions. This can be observed especially well for the pulse with an FWHM of $3.33 fs$ and $\mathbb{E} = 304 fV_s/a_B$ (compare the turquoise line in the upper left panel of figure 5.10). This precession happens significantly slower than the changes induced directly by the laser.

It seems that decay in Nickel^{II}oxide favours electrons that have no counterpart with spin in the other direction, as almost all calculations with decay give a lower absolute value for $\langle S_z \rangle$ than without. This is plausible, because Auger-Meitner decay does not change the spin of the electrons, meaning that the population making up the majority has more decay channels than the minority.

Furthermore, decay smooths the seemingly chaotic behaviour induced by strong laser fields.

Since spin is a direction-dependent quantity its behaviour under different laser polarisations is of interest. It is shown in figure 5.11.

As expected, the laser light in z -direction manages to have the most impact on the value of $\langle S_z \rangle$, especially for an FWHM of $1 fs$. Even here the spin is not flipped, though.

The very short pulse with the polarisation in $(1, 1, 0)$ -direction is the only observed pulse that manages to increase the absolute value of $\langle S_z \rangle$ when it starts exciting the system, albeit only by a very small amount.

Therefore, within the scope of these simulations, no spin-flip excitation can be observed.

5.6 Discussion

The ultrafast dynamics of Nickel^{II}oxide were observed for different levels of theory. In the 2 level description the system mostly behaved as expected from Rabi-theory, although its electric field wave was enveloped by a Gaussian. This behaviour broke down for very high electric field strengths of about $1500 V/a_B$ and higher. The Crystal Field Theory description offered a more complicated but similar behaviour for short pulse lengths and low field strengths. This trend was continued in the description by Ligand Field Theory, but for larger pulse lengths and field strengths the behaviour became much richer.

In this description, orbital excitation and de-excitation happened for all field strengths and pulse lengths. Charge transfer excitation from the ligand orbitals to

Ni-3*d* was observed to be strongest for pulse lengths between 333 *as* and 1 *fs* and did almost not happen for a pulse length of 3.33 *fs*, a behaviour which could be explained by the results of the X-ray absorption spectrum. No total spin-flip excitation could be observed for any combination of pulse length, field strength and polarisation.

The inclusion of decay in the calculation significantly changed the time-evolution. Orbital excitations were strongly suppressed and were practically impossible for pulse lengths over 500 *as*, although they could be forced by very strong fields. The lower Ni-3*d* occupation amplified the charge transfer excitation. The spin-flip excitations were also affected, in that the absolute value of $\langle \mathcal{S}_z \rangle$ was decreased with time.

The inclusion of the decay mechanism certainly leaves room for improvement. Here, only one parameter γ was used for all decay channels, while in reality the strength differs from channel to channel. Calculating the values of γ in an *ab initio* fashion, as it is done in section 7, is therefore desirable. The approximation of only allowing decayed electrons with $l_z = 0$ can be treated with more computational power, as the inclusion of larger values does not exponentially scale the complexity of the calculation.

It might also be instructive to include different relaxation mechanisms like fluorescence decay, during which a single electron is de-excited and a photon emitted.

To quantify the interaction between light and matter more accurately, the electric dipole moments can be calculated from the full basis orbitals, whose spatial dependence can be extracted from a Density Functional Theory calculation, as is done in section 6.

What the calculations are lacking most is experimental measurements to test the predictions they make. Only those can conclusively reveal whether the assumptions and simplifications made to arrive at the results are justified, and help to tweak them.

This aspiration is not restricted to one specific material, because the method presented here and tested for the exemplary case of Nickel^{II} oxide can easily be applied to any system for which an approximate Hamiltonian of comparable complexity is known.

Comparing the theory to experiments will advance the understanding of interactions between light and matter, and the presented technique may well become common for simulating photochemical reactions.

6 Sulphur-hexafluoride

Most of the content of this chapter will also have been published in ref. [68].

6.1 Motivation

The realms of chemistry, biology and solid state physics are almost entirely governed by the electronic interactions between charged particles. Most phenomena in atoms can be described by electrons subjected to the potential of a nucleus, where on a one-particle level they occupy various atomic orbitals. In chemically inert molecules a description of non-interacting nuclei in the Born-Oppenheimer approximation⁶ is usually sufficient, in which the individual orbitals combine to form molecular orbitals (abbr. ‘MO’).^{59,62}

Despite the many merits of mean field theory, some phenomena elude description without the explicit inclusion of many-body interactions. Specifically the exchange part of the Coulomb interaction allows for mixing between otherwise completely decoupled configurations, thus influencing for example the shape of spectra.⁶⁰

It is shown here that this interaction can be probed and its effective value tuned by lasers, as the electric light field mixes configurations with different exchange parameters. This tuning happens on a timescale below that of nuclear dynamics. Controlling the effective value of the fundamental exchange parameter is a novel step towards laser directed chemistry in the Born-Oppenheimer regime.

The effect is demonstrated in this section for the molecule Sulphur-hexafluoride (abbr. ‘SF₆’). It is the candidate of choice because its chemical inertness makes it experimentally accessible, and because its small number of atoms and lack of open shells result in low computational time and clear dynamics. Furthermore, its static X-ray absorption spectrum has been extensively studied both experimentally³⁶ and theoretically.^{15,39} This makes it ideal for this proof-of-concept study.

In the experiment, the X-ray absorption spectrum (abbr. ‘XAS’) of SF₆ at a photon energy of around 170 eV was measured under the influence of a strong infrared (abbr. ‘IR’) tuning laser beam with a photon energy of 0.808 eV (compare ref. [68]). The result is two peaks arranged in a doublet, whose area ratio and energy splitting depend on the effective exchange energy, which is modified by the tuning laser.

Both of the two directly measurable quantities are theoretically reproduced by a few-configuration model fit. A smaller version of this model allows to use those parameters to calculate the numerical value of the effective exchange energy. The section is concluded by a parameter-free *ab initio* simulation in good qualitative agreement with the measurement, which allows to obtain information about the broadening of the XAS pulse.

6.2 Few-Configuration Fit

Theory

In the few-configuration fit method, a suitable basis comprised of the most important many-body wave functions is constructed to find a few-parameter matrix representation of the operators at play.

The first basis vector is the initial state of the system, assumed to be the ground state $|\psi_0\rangle$. For simplicity its energy is set to 0.

The next set of states are those that are reached by acting on $|\psi_0\rangle$ with an operator \mathcal{T}_{XAS} corresponding to a dipole transition of interest. The case considered here is that of an excitation from a core shell c with p character to a valence shell v with s character, but the method is applicable to numerous other cases as well. The degeneracy of the core shell is lifted by spin-orbit coupling, resulting in two basis states $|c_+^{-1}v^1\rangle$ and $|c_-^{-1}v^1\rangle$ corresponding to a core hole with total angular momentum quantum number $j = 3/2$ and $j = 1/2$, respectively.

In the absence of a tuning laser this basis suffices to describe the shape of a double peak. It is insightful to set up the model for this simplified case.

With the given basis set it is a straightforward task to find the form of the matrix representations of the operators of interest. The perturbatively treated excitation \mathcal{T}_{XAS} can couple the ground state to the first excited states, and no others. Because there are (in this case) twice as many c_+ orbitals as there are c_- , the coupling is given by a normalised multiplicity prefactor times the dipole moment d times the

peak field strength ϵ_{XAS} . Thus, the matrix representation is found to be

$$T_{XAS} = \begin{pmatrix} 0 & \sqrt{\frac{2}{3}}d\epsilon_{XAS} & \sqrt{\frac{1}{3}}d\epsilon_{XAS} \\ \sqrt{\frac{2}{3}}d\epsilon_{XAS} & 0 & 0 \\ \sqrt{\frac{1}{3}}d\epsilon_{XAS} & 0 & 0 \end{pmatrix} . \quad (6.1)$$

The diagonal entries of the Hamiltonian matrix are given by the energy expectation values of the basis states. The ground state energy is gauged to 0, the excited block begins at some energy E and is split by an energy difference of Δ .

The mechanism mixing states with different core holes is the exchange part of the Coulomb interaction.⁶⁰ Here it is labelled with E_x , completing the matrix form of the Hamiltonian,*

$$H = \begin{pmatrix} 0 & 0 & 0 \\ 0 & E & E_x \\ 0 & E_x & E + \Delta \end{pmatrix} . \quad (6.2)$$

According to the theory of radiation,¹⁶ excitation peaks correspond to eigenenergies of the Hamiltonian, and their integral measure to the absolute square of the transition operator matrix element (compare section 4.2). To theoretically calculate these quantities it is therefore, in this model, sufficient to rotate both H and T_{XAS} to the eigensystem of H .

As the Hamiltonian does not couple the ground state to any other, this transformation matrix R is found by diagonalising the lower right 2×2 submatrix, which can be done analytically. The resulting diagonal entries are given by

$$(RHR^t)_{2,2} = \frac{1}{2} \left(2E + \Delta - \sqrt{4E_x^2 + \Delta^2} \right) \quad (6.3)$$

$$(RHR^t)_{3,3} = \frac{1}{2} \left(2E + \Delta + \sqrt{4E_x^2 + \Delta^2} \right) , \quad (6.4)$$

showing that the peak energy splitting is

$$s = \sqrt{4E_x^2 + \Delta^2} . \quad (6.5)$$

*This form assumes that all matrix elements are real valued. The adjustment for complex values is straightforward and not shown here for the sake of brevity.

The transition probabilities are

$$(RTR^t)_{1,2}^2 = \frac{-4\sqrt{2}E_x + \Delta + 3\sqrt{4E_x^2 + \Delta^2}}{6\sqrt{4E_x^2 + \Delta^2}} \quad (6.6)$$

$$(RTR^t)_{1,3}^2 = \frac{4\sqrt{2}E_x - \Delta + 3\sqrt{4E_x^2 + \Delta^2}}{6\sqrt{4E_x^2 + \Delta^2}}, \quad (6.7)$$

leading to a peak area ratio of

$$r = \frac{-4\sqrt{2}E_x + \Delta + 3\sqrt{4E_x^2 + \Delta^2}}{4\sqrt{2}E_x - \Delta + 3\sqrt{4E_x^2 + \Delta^2}}. \quad (6.8)$$

Using equation (6.5) the result can be rewritten as

$$r = \frac{-4\sqrt{2}E_x + 3s + \sqrt{s^2 - 4E_x^2}}{4\sqrt{2}E_x + 3s - \sqrt{s^2 - 4E_x^2}}. \quad (6.9)$$

The expected value $r = 2$ is obtained in the limit $E_x \rightarrow 0$. For other ratios and splittings the model value of E_x , henceforth called effective exchange E_x^{eff} , can be found using this equation.

Including the tuning laser in the model is achieved by complementing the basis set by acting on the excited states with an operator \mathcal{T}_{IR} representing the laser field. In the present case it excites the valence electron in v to a (not necessarily specified) polarising orbital p , adding the new states $|c_+^{-1}p^1\rangle$ and $|c_-^{-1}p^1\rangle$. Because the laser field is treated in the dipole approximation and v is in this case assumed to have s character, the polarising orbital must have p character due to selection rules.

The new states are not coupled by \mathcal{T}_{XAS} , so its matrix representation T_{XAS} remains the same except for the addition of two rows and columns with entries 0.

The tuning excitation \mathcal{T}_{IR} is treated as part of the Hamiltonian \mathcal{H} . It only couples between the two excited blocks, with a strength of $d'\epsilon_{IR}$, and cannot mix states with different core holes.

The two states with an occupied polarising orbital begin at energy E' , are split by Δ' , and are also coupled by exchange interaction, but with a different matrix element E'_x .

This leads to the new Hamiltonian matrix form

$$H = \begin{pmatrix} 0 & 0 & 0 & 0 & 0 \\ 0 & E & E_x & d'\epsilon_{IR} & 0 \\ 0 & E_x & E + \Delta & 0 & d'\epsilon_{IR} \\ 0 & d'\epsilon_{IR} & 0 & E' & E'_x \\ 0 & 0 & d'\epsilon_{IR} & E'_x & E' + \Delta' \end{pmatrix}. \quad (6.10)$$

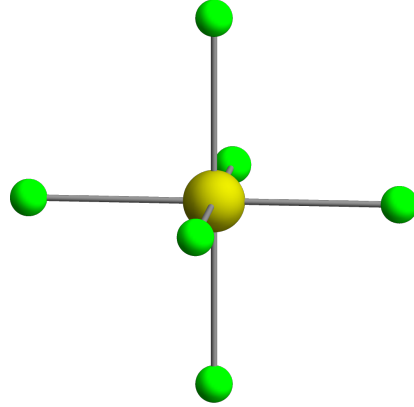


Figure 6.1: The molecular structure of Sulphur-hexafluoride.

Because finding the eigensystem of the lower 4×4 submatrix involves solving a polynomial of fourth order, analytically rotating both matrices to find s and r proves unwieldy. However, it is easily done for numerical values, many of which can be obtained from *ab initio* considerations once the system is specified.

The molecule Sulphur-hexafluoride (abbr. ‘SF₆’) is comprised of a central sulphur atom and six fluorine atoms arranged in octahedral geometry with a bond length* of $2.99a_B = 1.58\text{\AA}$ (compare figure 6.1).

The electronic structure of SF₆, as it is depicted in figure 6.2, is found by converging a DFT simulation. Also shown in the figure is the electron density

$$n_j(\vec{r}) = \bar{\psi}_j(\vec{r})\psi_j(\vec{r}) \quad (6.11)$$

of the molecular orbitals.

Equipped with the knowledge of the spatial dependence $\psi(\vec{r})$ of the wave functions the dipole matrix element

$$d' = \int_{\mathbb{R}^3} \bar{\psi}_v(\vec{r})z\psi_p(\vec{r}) d\vec{r} \quad (6.12)$$

can be calculated, where the polarising orbital ψ_p is approximated as the first unoccupied orbital with S- p character.[†] Analogously, d can be found by exchanging ψ_p for ψ_c .

*as found by an FPLO force relaxation

[†]The error made due to this approximation can be completely absorbed into a rescaling of ϵ_{IR} .

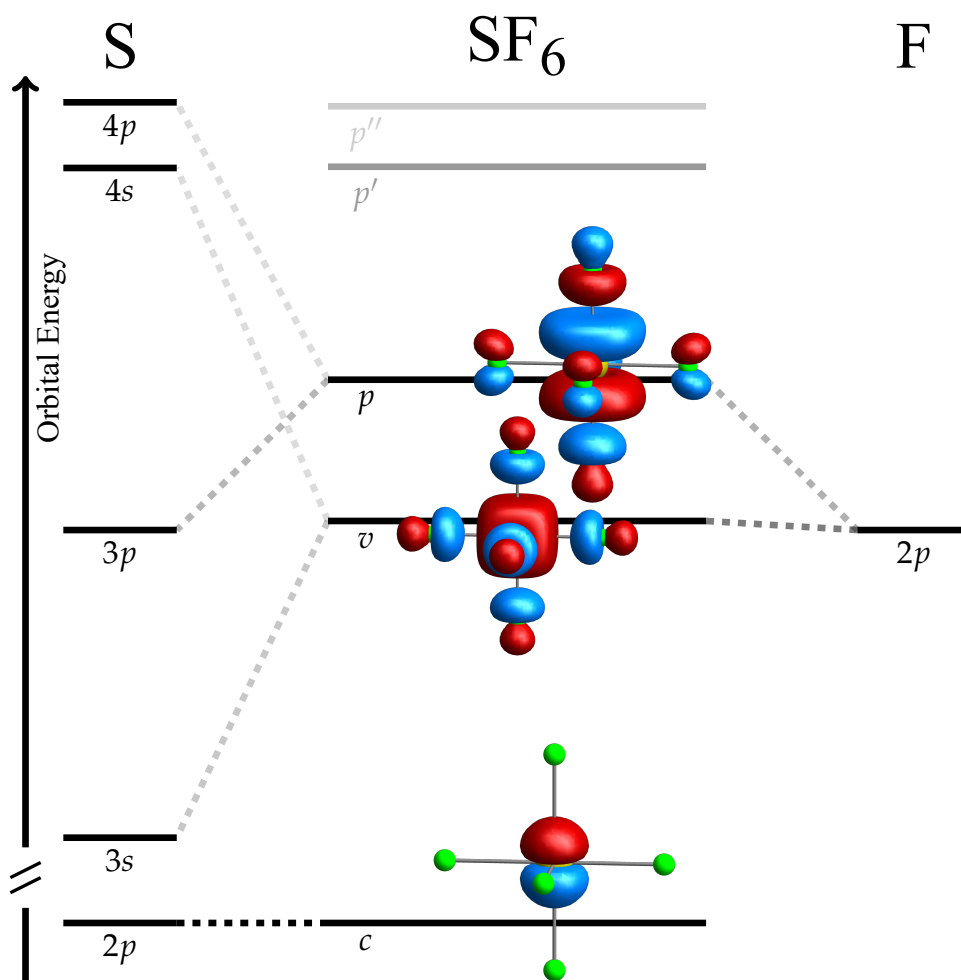


Figure 6.2: The energy level scheme of Sulphur-hexafluoride and its atomic constituents. The overlap of the core, valence and polarising molecular orbitals with the atomic orbitals is indicated by the opacity of the dotted lines, and their electron densities are plotted. More polarising orbitals at higher energies (not to scale) are suggested. The spin-orbit splitting of the core orbital is not displayed here.

The energy E of the first excited state can be approximated as the difference of the one-particle energies of the valence and core orbital. As it turns out, E is irrelevant for determining the peak energy splitting and area ratio, but it is mentioned here for the sake of completeness.

In the considered system E_x can be rewritten as

$$E_x = \frac{2\sqrt{2}}{9}G_1 \quad , \quad (6.13)$$

with the Coulomb integral G_1 , which can be approximately calculated using atomic radial functions and equation (3.9). However, as the occupied orbitals are not atomic, it is necessary to scale this result by a factor g , which is usually between 0.8 and 0.9.

The Hilbert space of a p core shell with one hole and an s orbital with one excited electron is spanned by a total number of $6 \times 2 = 12$ Slater-determinants. By calculating all matrix elements of the operators representing spin-orbit coupling and the exchange interaction on this basis an analytical expression for Δ in terms of ζ and E_x can be found. It is given by

$$\Delta = \frac{3}{2}\zeta - \frac{E_x}{\sqrt{2}} \quad . \quad (6.14)$$

Since ζ comes from an atomic calculation, a small scaling factor z is also allowed for here.

The parameters E' , E'_x and Δ' are found by fitting the theoretical results for peak energy splitting and area ratio to an experimental data point.

Results

The X-ray absorption spectrum as experimentally measured in ref. [68] is displayed in figure 6.3 for a low tuning laser field strength of $0.12 V/a_B$, and the highest available field strength of $2.16 V/a_B$.

In the absence of any coupling via exchange energy, the first peak at lower energy would correspond to an excitation from an S- $2p$ orbital with total angular momentum of $j = 3/2$, and its area would be twice as large as that of the second peak. As is visible from the plots, the first peak is instead suppressed compared to the second, and the suppression increases with tuning laser field strength.

At first glance the second peak is suppressed as well, but its loss in peak intensity is made up for by a broadening, such that the sum of the total integrals of the two peaks remains unchanged within error bars.⁶⁸

A small shifting of the peak position towards lower energies can also be observed, an effect which is not included in the theoretical description.

Using a Voigt fit, the areas and positions of the peaks, and hence their ratio and splitting, can be obtained from the spectra, thus quantising the observations.

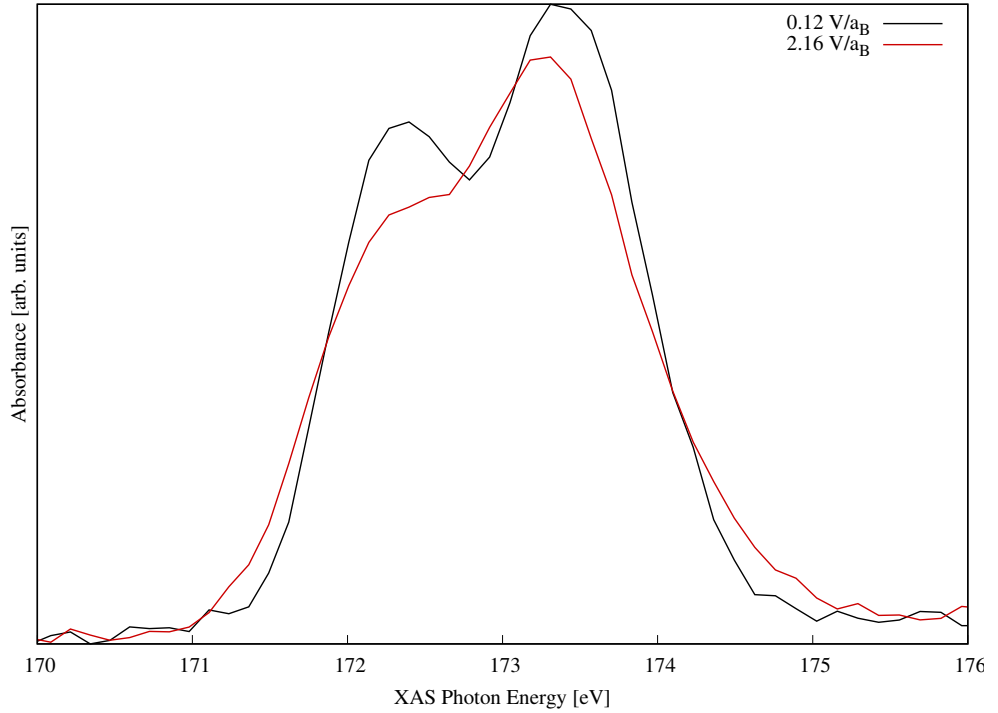


Figure 6.3: X-ray absorption spectrum of SF_6 at low ($0.12 V/a_B$, black line) and high ($2.16 V/a_B$, red line) tuning laser field strength.

The parameters for the few-configuration fit are listed in table 6.1. All values needed to reproduce the peak area and splitting of the X-ray absorption spectrum in absence of the tuning laser field can be obtained from *ab initio* considerations. The values of G_1 and ζ are both scaled with a respective factor of g and z in order for the results to agree with the first data point.

The numerical value of $g = 0.85$ is very common and can be explained, because assuming atomic orbitals in the calculation of Coulomb integrals has a tendency to overestimate their overlap. The factor of $z = 1.05$ is also well within reason and only necessary for perfect agreement with experiment.

The remaining parameters E' , E'_x and Δ' are chosen such that the model reproduces the peak area ratio and energy splitting obtained from the Voigt fit of the experimental spectrum at highest tuning laser field strength.

The energy difference between the first and second block of excited states is

Parameter	Value
d	$0.05 ea_b$
E	$160.77 eV$
$g \cdot G_1$	$0.85 \cdot 1.23 eV$
E_x	$0.33 eV$
$z \cdot \zeta$	$1.05 \cdot 0.75 eV$
Δ	$0.94 eV$
d'	$1.22 ea_b$
E'	$163.10 eV$
E'_x	$0.80 eV$
Δ'	$0.15 eV$

Table 6.1: The parameters for and from the few-configuration fit. The values of d , E , G_1 , ζ and d' are calculated in an *ab initio* fashion, while g and z (and subsequently E_x and Δ), E' , E'_x and Δ' are fitted to the experiment.

given by $E' - E = 2.33 eV$, which is about half as large as expected from the DFT calculation. However, since DFT can never include all reachable states in its basis and is optimised for finding the ground state of a system, it can only be considered an approximation and potentially overestimates the energy splitting.

Compared to E_x , E'_x is larger by a factor of about 2.5. An increase in exchange energy is expected, as the tuning laser in dipole approximation excites an electron from a core orbital with odd symmetry to the even valence orbital, and from there to the odd polarising orbital.* Because both the polarising and the core orbital have the same symmetry (and, if the valence orbital has s character, even the same angular momentum quantum number l) their overlap is potentially larger.

The comparably small value of $\Delta' = 0.15 eV$ stems from the fact that equation (6.14), which would instead suggest a value of $0.59 eV$, does not hold for the parameters of the polarising orbital, which due to selection rules necessarily has another character than the valence orbital.

With all parameters of the few-configuration fit model fixed, its results can be plotted together with the experimental ones. The peak area ratio is shown in figure 6.4, and the energy splitting in figure 6.5.

The trend of a suppressed first peak observed in the spectra of figure 6.3 is confirmed by the full evaluation of all 19 experimental data points. This means that the effective exchange energy increases, as the tuning laser mixes the valence with the

*Alternatively, it may excite from even to odd to even orbital if another system is considered.

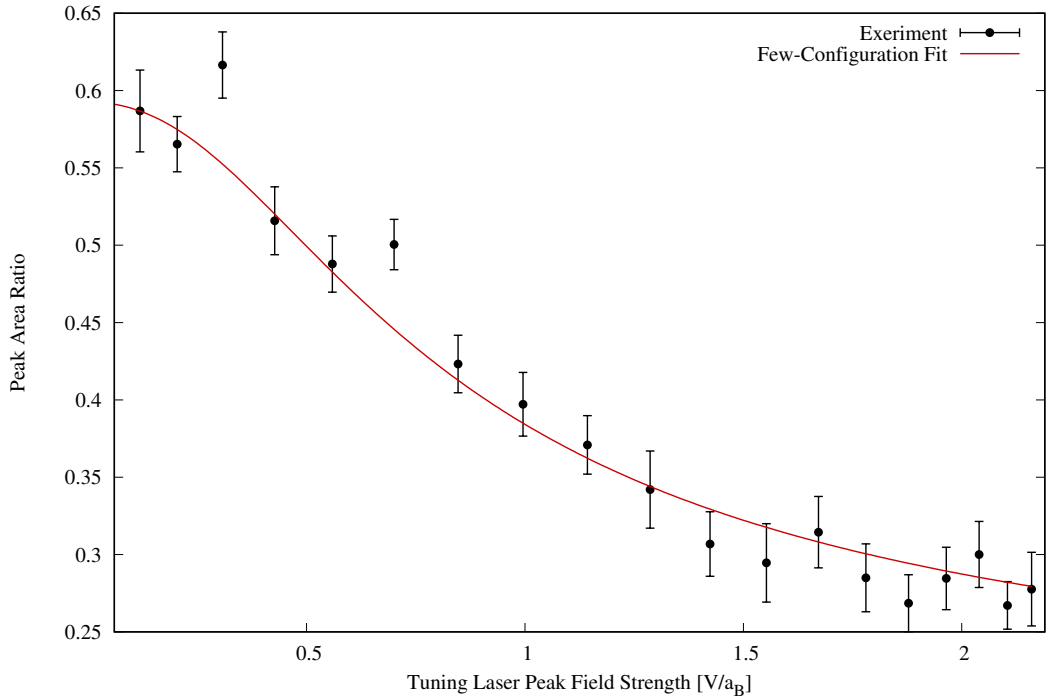


Figure 6.4: The ratio between the two peak areas as obtained from a Voigt fit to the experimental data (black dots) and from the few-configuration fit model (red line).

polarising orbital.* The few-configuration fit reproduces the behaviour remarkably well, considering that it is only fitted for the spectrum at the highest tuning laser field strength and at its absence.

At a first glance at the experimental points alone, a linear dependence of the area ratio on the tuning laser field strength is suggested. However, because a negative electric field strength is mathematically the same as the introduction of a phase of π in the oscillating field, it is expected to have the same effect as its positive counterpart. This means that the function describing the peak area ratio must be even in tuning laser field strength. The few-configuration fit model clarifies the behaviour, showing a quadratic dependence for low tuning laser field strengths and an approximately linear dependence only for larger values.

*For a plot of the effective exchange energy as extracted from the experimental data see figure 6.7.

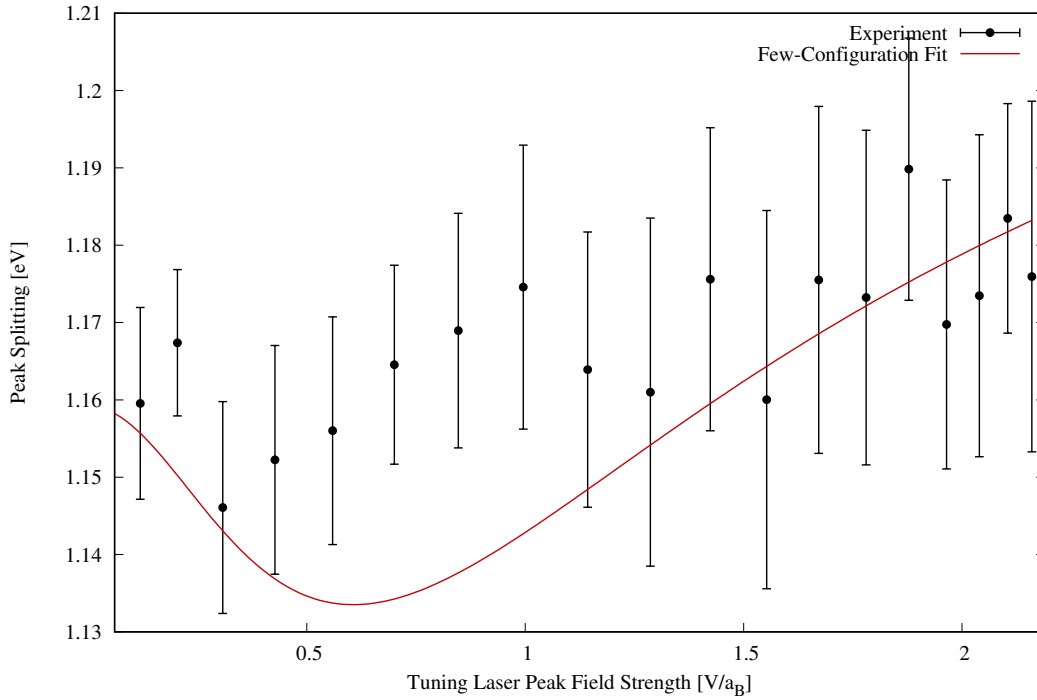


Figure 6.5: The splitting between the two peak energies as obtained from a Voigt fit to the experimental data (black dots) and from the few-configuration fit model (red line).

The energy splitting between the two peaks remains largely unchanged throughout the tuning laser field strength range (compare figure 6.5). Although the few-configuration fit has a small minimum at about $0.6 V/a_B$, no such behaviour can conclusively be observed experimentally, as it vanishes behind the error bars.

The fit model also suggests an increasing peak splitting at higher tuning field strengths, but whether or not this is realised in experiment remains an open question.

Figure 6.6 visualises the physical origins of the increase in effective exchange energy. In absence of the tuning laser the core hole can only be excited to the valence orbital, the electron density of which is plotted in the upper left. The phase of the (real valued) orbital is encoded in the colour of the isosurface. Increasing the field strength E_0 adds admixture with the polarising orbital and breaks the symmetry, as shown further to the right.

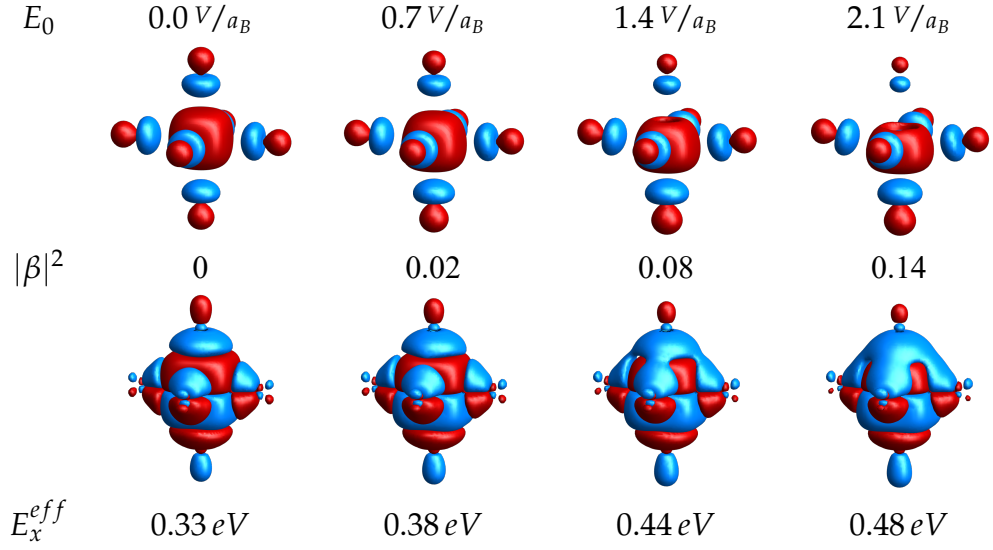


Figure 6.6: Electron densities (top) of the valence orbital, mixed with the polarising orbital with overlap β due to the tuning laser strength E_0 , densities of the product of this orbital with a p_z core orbital (middle), and operator density plot of the effective exchange energy E_x^{eff} between states with different total angular momentum j .

The mixing coefficients can be calculated by finding the four many-body states

$$|\Psi_+\rangle = \alpha |c_+^{-1}v^1\rangle + \beta |c_+^{-1}p^1\rangle \quad , \quad (6.15)$$

$$|\Psi_-\rangle = \alpha' |c_-^{-1}v^1\rangle + \beta' |c_-^{-1}p^1\rangle \quad , \quad (6.16)$$

$$|\tilde{\Psi}_+\rangle = \gamma |c_+^{-1}v^1\rangle + \delta |c_+^{-1}p^1\rangle \quad \text{and} \quad (6.17)$$

$$|\tilde{\Psi}_-\rangle = \gamma' |c_-^{-1}v^1\rangle + \delta' |c_-^{-1}p^1\rangle \quad , \quad (6.18)$$

that together with the ground state would diagonalise the matrix in equation (6.10) in absence of any exchange interaction. They each have a well-defined total angular momentum, but mix the valence with the polarising orbital. In absence of the IR laser field the coefficients β , β' , γ and γ' all vanish.

The coefficients α and β of the state with lowest energy are used to find the effective mixed valence orbital

$$\psi_m(\vec{r}) \stackrel{\text{def}}{=} \alpha\psi_v(\vec{r}) + \beta\psi_p(\vec{r}) \quad . \quad (6.19)$$

The exchange interaction features terms of the form

$$\int_{\mathbb{R}^3} \int_{\mathbb{R}^3} \overline{\psi_1(\vec{r}_1)} \overline{\psi_2(\vec{r}_2)} \frac{1}{|\vec{r}_1 - \vec{r}_2|} \psi_1(\vec{r}_2) \psi_2(\vec{r}_1) d\vec{r}_1 d\vec{r}_2 \quad . \quad (6.20)$$

To visualise its increase, the density of the product $\overline{\psi_m(\vec{r})} \psi_c(\vec{r})$ of mixed and core orbital is plotted in the middle line of figure 6.6. The p_z orbital is chosen here as an example of ψ_c . The isosurface at the very small value of $3 \cdot 10^{-6}$ is shown, for significantly larger values all four plots would resemble the more localised core orbital. As expected, the product is antisymmetric in absence of the tuning laser. This means that the integral (6.20) takes the form

$$\int_{\mathbb{R}^3} \int_{\mathbb{R}^3} \overline{a(\vec{r}_1)} \frac{1}{|\vec{r}_1 - \vec{r}_2|} a(\vec{r}_2) d\vec{r}_1 d\vec{r}_2 \quad , \quad (6.21)$$

with the antisymmetric function $a(\vec{r}) \stackrel{\text{def}}{=} \overline{\psi_v(\vec{r})} \psi_c(\vec{r})$. For large values of $|\vec{r}_2|$ the contribution of the integrand is small, because the core orbital and hence $a(\vec{r}_2)$ is localised. For small values of $|\vec{r}_2|$ the function $\frac{1}{|\vec{r}_1 - \vec{r}_2|} \approx \frac{1}{|\vec{r}_1|}$ is approximately symmetric and is multiplied by the antisymmetric $a(\vec{r}_1)$. This results in the integral over \vec{r}_1 approximating 0. If the approximation is not valid, $\frac{1}{|\vec{r}_1 - \vec{r}_2|}$ is still strictly positive, such that the terms $\frac{a(\pm\vec{r}_1)}{|\pm\vec{r}_1 - \vec{r}_2|}$ in the integral have opposite sign and partially cancel each other. The admixture of the polarising orbital breaks the antisymmetry and thus leads to larger exchange integrals.

6.3 *Ab initio* many-body Simulation

Theory

To reproduce the experimental behaviour with as few fit parameters as possible, a full many-body simulation of the SF₆ system is done in QUANTY. It is based on an FPLO calculation, from which a one-particle basis set is obtained via a downfolding (compare section 3.1), including those molecular orbitals whose overlap is strongest with the atomic basis orbitals S-2p, S-3s, S-3p and S-4s.

Knowing the spatial dependence of the basis orbitals, the Coulomb parameters in equation (3.8) are calculated, which together with the orbital energies and spin orbit parameter ζ complete the Hamiltonian \mathcal{H} .

Both the XAS and the (infrared) tuning laser are simulated as polarised dipole operators $\mathcal{T}_{XAS/IR}$ with the same polarisation \vec{p} . In case of XAS, the operator is

enabled to make a $2p - 3s$ and $2p - 4s$ excitation*, as well as the reverse. The tuning laser is built up analogously, with the $2p$ orbital replaced with $3p$. The electric dipole moments corresponding to the transitions are, as before, found by carrying out the spatial integrals involved in $\langle \psi_1 | r_i | \psi_2 \rangle$ numerically.

To accurately reproduce the experimental setup, the operator of the tuning laser is further modified by a time-dependent prefactor

$$E_\varphi(t) = E_0 \cos(\omega t + \varphi) \exp\left(-\frac{t^2}{2\sigma^2}\right) , \quad (6.22)$$

with the electric laser field strength amplitude E_0 , the laser frequency $\omega = 0.80771 \text{ eV}/\hbar$, and a standard deviation of the pulse length $\sigma = 9.01 \text{ fs}$ (and thus a full width at half maximum (abbr. ‘FWHM’) of $2\sqrt{2 \ln 2} \sigma = 21.21 \text{ fs}$, which corresponds to an FWHM of 15 fs for the intensity).

In the performed experiment the XAS laser pulse has the same polarisation as the tuning laser and usually occurs $2/3$ IR electric field periods after the maximum of the IR laser intensity.¹³ It can hence be found as

$$t_{XAS} = t_m(\varphi) + \frac{2}{3} \frac{2\pi}{\omega} , \quad (6.23)$$

where $t_m(\varphi)$ maximises $E_\varphi^2(t)$.

Accordingly, the simulation calculates[†]

$$S(\omega_{XAS}, t) = -\text{Im} \left\langle \psi_0 \left| \mathcal{T}_{XAS}^\dagger \frac{1}{\omega_{XAS} - \mathcal{H} - \mathcal{T}_{IR}(t) + i\Gamma} \mathcal{T}_{XAS} \right| \psi_0 \right\rangle , \quad (6.24)$$

the X-ray absorption spectrum at energies ω_{XAS} under the influence of the tuning laser, around the time t_{XAS} (compare section 4.2).

The intensity of the XAS pulse is assumed to follow a Gaussian curve with a broadening of $\sigma_{XAS} = 38 \text{ as}$ in the time domain, as is justified below. To account for this, the spectrum is averaged over 11 points in a small region $[t_{XAS} \pm 126 \text{ as}]$, weighted with

$$G(t) = \exp\left(-\frac{t^2}{2\sigma_{XAS}^2}\right) . \quad (6.25)$$

*again denoting the molecular orbitals, not the atomic ones

[†]Since \mathcal{T}_{IR} only acts between unoccupied orbitals the system remains in its ground state throughout the simulation.

MOs	Dipole [ea_b]	G_0 [eV]	G_1 [eV]	G_2 [eV]
S-2p, S-3s	0.05	-	0.96	-
S-2p, S-3p	-	1.08	-	1.07
S-2p, S-4s	0.01	-	0.11	-
S-3s, S-3p	1.22	-	5.65	-
S-3p, S-4s	0.68	-	0.32	-

Table 6.2: The electric dipole moments and exchange Coulomb integrals between several molecular orbitals, as calculated from the spatial distribution of the wave functions. The nomenclature reflects the largest overlap the MO has with the atomic basis orbital of the same name.

The result is further averaged over various choices

$$\varphi = (1, 2, \dots, 30) \frac{\pi}{30} \quad (6.26)$$

of the tuning laser phase.

To account for the random orientation of the molecule in experiment, an average over the laser field polarisations

$$\vec{p}_1 = \begin{pmatrix} 1 \\ 0 \\ 0 \end{pmatrix}, \quad \vec{p}_2 = \frac{1}{\sqrt{2}} \begin{pmatrix} 1 \\ 1 \\ 0 \end{pmatrix}, \quad \vec{p}_3 = \frac{1}{\sqrt{3}} \begin{pmatrix} 1 \\ 1 \\ 1 \end{pmatrix} \quad (6.27)$$

with respective geometry-multiplicity based weights of 6, 12 and 8 is done, bringing the total number of spectra calculated for one value of the tuning laser field strength to 990.

Results

The results of the calculation of the electric dipole moments and exchange Coulomb integrals between the molecular orbitals making up the basis are given in table 6.2. The direct Coulomb integrals are implemented on a mean field level.

The averaged spectra resulting from the simulation are fitted with the same Voigt fit method as the experimental data for every tuning laser field strength. This guarantees the best comparability of the extracted peak ratios and energy splittings with the measured data.

One source of error is that in the simulation only a single molecular orbital represents the polarising orbital, instead of the plethora of levels available to nature.

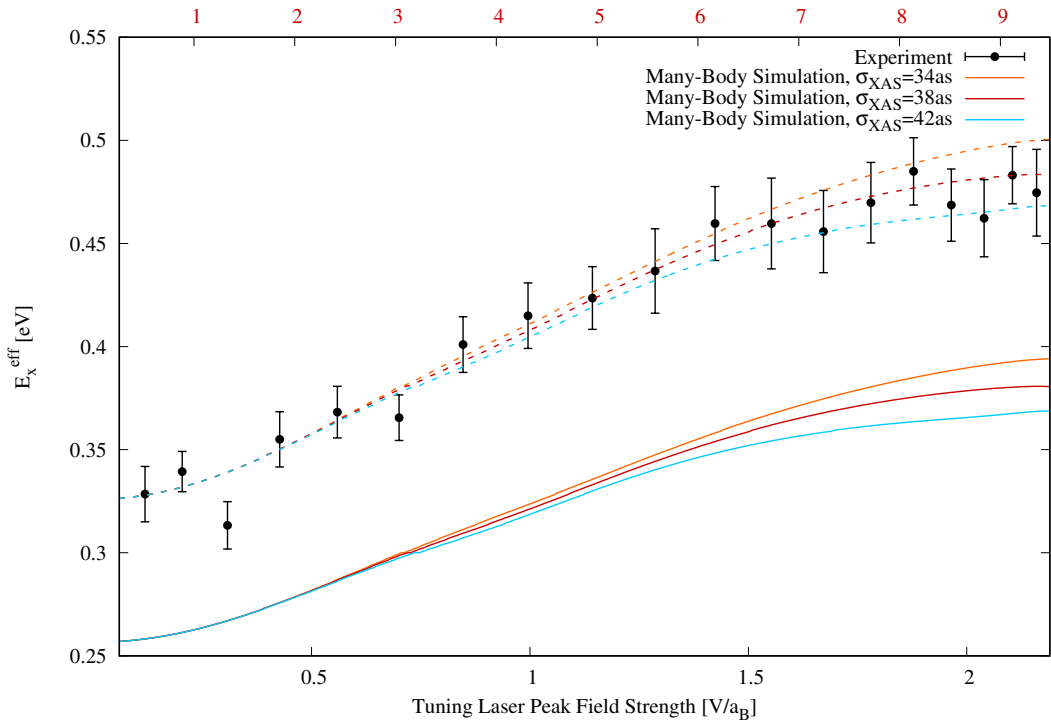


Figure 6.7: The effective exchange energy as obtained from the peak area ratio and energy splitting of the experimental data (black dots) and from the *ab initio* many-body simulation for a temporal broadening of the XAS laser pulse of $\sigma_{XAS} = 34 \text{ as}$ (orange line), $\sigma_{XAS} = 38 \text{ as}$ (red line) and $\sigma_{XAS} = 42 \text{ as}$ (turquoise line). Also shown are the results from the simulation scaled by a factor of 1.27 (dotted lines). Note that the scale of the tuning laser field strength for the simulated data is multiplied with a factor of 4.33 compared to the experiment.

As such, the polarisability of the valence orbital is underestimated. The calculation further relies on an FPLO calculation. As DFT codes, by nature, are optimised for the ground state of a system, the energy spacing between the initially unoccupied valence and polarising orbital is overestimated. Both these effects mean that a larger tuning laser field strength is necessary to observe the same effect as in experiment.

Another effect that FPLO does not take into account is that the core hole created during the excitation process attracts the valence electron, thus decreasing the spatial distribution of the valence and polarising orbital. This leads to an increased overlap with the confined core orbital and consequently larger values for the Coulomb

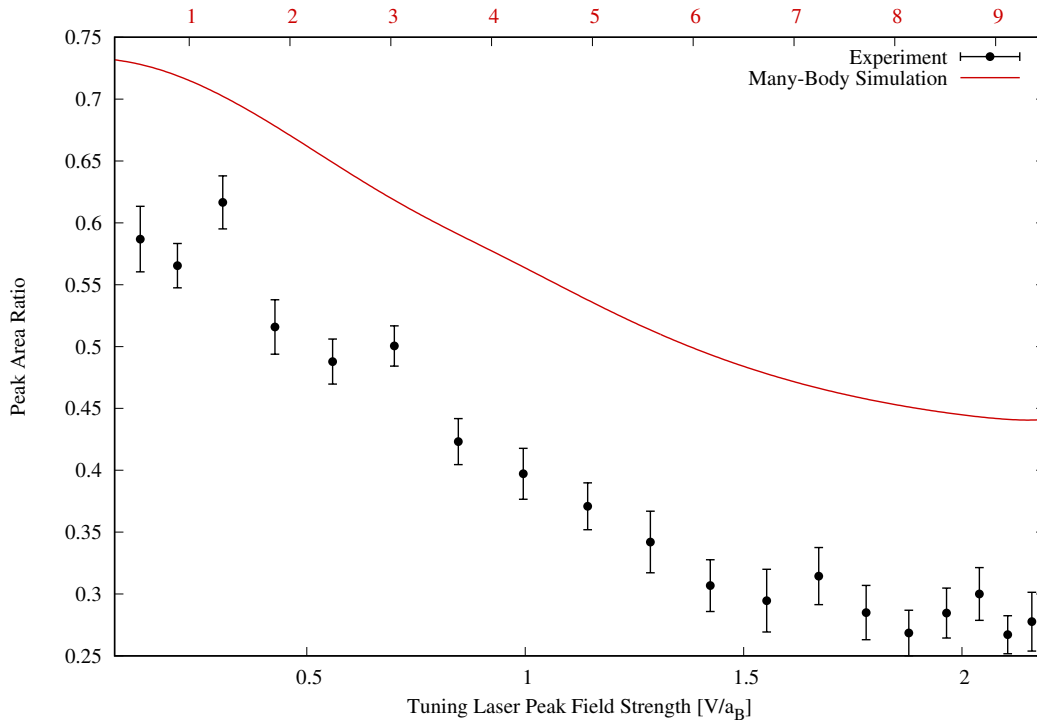


Figure 6.8: The ratio between the two peak areas as obtained from a Voigt fit to the experimental data (black dots) and from the *ab initio* many-body simulation (red line). Note that the scale of the tuning laser field strength for the simulated data is multiplied with a factor of 4.33 compared to the experiment.

parameters. The exchange energy is therefore underestimated in the simulation.

It is consequently necessary to make some adjustments. The effective exchange energy E_x^{eff} can be calculated from the extracted data using equation (6.9). It is displayed in 6.7, for both experiment and simulation. Their values are assumed to differ from one another by a constant scaling factor of 0.79, which is chosen such that experiment and simulation agree on the first data point. To remedy the other systematic error, the tuning laser field for the simulation is scaled by a factor of about 4.33, to make the curves agree on the last data point.

However, the shape of the simulated curve and thus its agreement with the other experimental data points depends on the assumed width σ_{XAS} in equation (6.25) to a surprising amount. It is therefore possible to extract the temporal width of the XAS

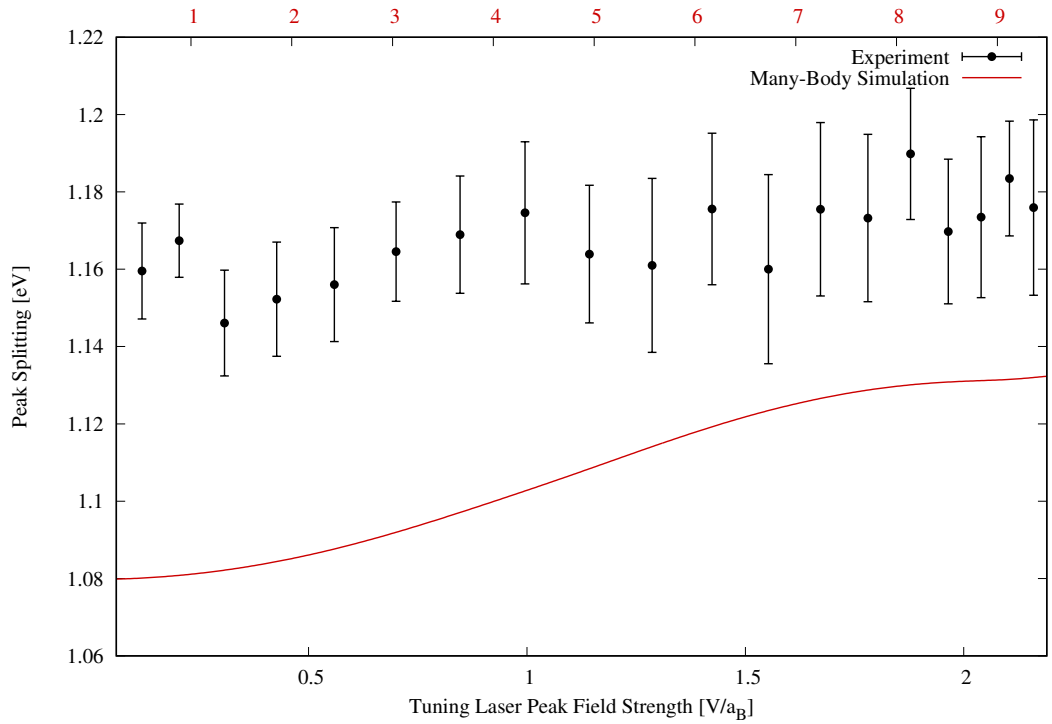


Figure 6.9: The splitting between the two peak positions as obtained from a Voigt fit to the experimental data (black dots) and from the *ab initio* many-body simulation (red line). Note that the scale of the tuning laser field strength for the simulated data is multiplied with a factor of 4.33 compared to the experiment.

laser pulse, which was previously unknown, from the comparison of simulated and experimental data in figure 6.7. It is found to be approximately

$$\sigma_{XAS} \approx 38 \pm 4 \text{ as} \quad , \quad (6.28)$$

which corresponds to an FWHM of $90 \pm 10 \text{ as}$. The error margin is estimated from the error bars of the experimental data in the figure.

The tuning laser manages to change E_x^{eff} from about 0.32 eV to approximately 0.48 eV , which is an increase by 50%. For even higher field strengths the energy is suggested to saturate. Because the Voigt fitting procedure is inadequate to describe the high field strength data of the simulation, this behaviour is neither confirmed nor contradicted by the calculation.

The area ratio of the peaks is shown in 6.8, and the energy splitting between them in figure 6.9 for both the experimental and simulated data. Because the underestimation of the effective exchange energy changes the behaviour of both quantities in a non-trivial manner, they cannot reproduce the experimental data points, even after the discussed scaling of the tuning laser field strength axis.

The simulation of the peak splitting shows a different behaviour than the few-configuration fit, as can be seen by comparing figure 6.5 and figure 6.9. The necessary scaling of the exchange interaction would influence the curve of the latter, but the experimental resolution does not allow to decide which of the two will then be closer to reality.

6.4 Discussion

The X-ray absorption spectrum, and specifically the peak area ratio and energy splitting of one doublet, were measured under the influence of a tuning laser. The ratio was observed to decrease with increasing field strength.

A few-configuration model resulting in a 3×3 matrix was able to explain this behaviour by an increase in the effective exchange energy, and yielded the means to quantify it. It was shown to grow by about 50%.

Extending the few-configuration model supplied a 5×5 matrix which could be fitted to two data points to accurately reproduce all others. It resolved the mystery of an apparent linear field dependency.

This model may be improved by making the analytical considerations for the core and polarising orbital leading to relations between Δ' and E'_x analogous to equation (6.14). In order to do that the 12 Slater-determinants spanning the space of one hole in the p shell and one electron in the s shell would need to be complemented by the $6 \cdot 6 = 36$ configurations of one hole in $S-2p$ and one electron in $S-3p$. This would eliminate one of the five remaining fit parameters from the theory.

An *ab initio* many-body calculation without any fit parameters reproduced the data qualitatively. It could be shown to come into quantitative agreement after a scaling of the two axes. Furthermore it was possible to extract the approximate temporal width of the XAS laser pulse from the comparison between simulated and measured data.

The discrepancies necessitating the scaling are well understood to be caused by the limitations of Density Functional Theory. There are means to push these further. Including more atomic basis orbitals in the DFT calculation would enable it to more accurately reproduce the energy difference between unoccupied orbitals. This would lessen the need to scale the tuning laser field strength axis. Some scaling

would still be necessary, though, because the theory would resume to underestimate the polarisability of the molecule.

Executing an additional DFT calculation with a fixed artificial core hole would result in spatially more confined unoccupied orbitals. Using these would more accurately reproduce the Coulomb integrals and thus exchange energy, possibly erasing the necessity of one scaling parameter.

An improved theory should furthermore be able to reproduce the total energy shift of the peaks, which was observed in figure 6.3.

Sulphur-hexafluoride was chosen as the scrutinised system because its comparably simple dynamics allow for a clear proof-of-concept that lasers can be used to tune the effective exchange interaction between various configurations. The *ab initio* simulation can easily be adjusted to describe other systems. It can thus serve to pick a more complex one with richer dynamics to be observed in experiment. Adjusting the few-configuration model to fit new results is even less complicated.

This interplay of prediction and measurement can lead the way to further developing lasers to tools for even more applications, for example as chemical agents on the sub-nucleonic timescale.

7 Holmium-doped Gold

7.1 Motivation

In his 1930 letter* to the “Radioactive Ladies and Gentlemen”, Wolfgang Pauli proposed a new particle,⁸⁰ which we today know as the ‘neutrino’. Its existence solved the issue of otherwise non-conserved energy during the β -decay that had arisen at that time.¹¹ Pauli wrote that the new particle should be neutral in charge and of mass comparable to that of the electron.

Pauli’s statement about the mass of the neutrino is not necessary to explain decay via the β -channel, and for a time it was believed that the particle was indeed massless. This hypothesis has since been disproven by the discovery of several neutrino flavours and oscillations between them, which can only be explained if they are massive particles.^{1,2,26} Whilst the mechanism allows to measure the differences between the squares of the mass eigenvalues, it makes no statement about the absolute mass.²⁵

Today, more than 90 years after the proposal of its existence, only upper limits have been found for the mass of the electron neutrino.⁵⁶ One proposed attempt to assign a numerical value to this quantity is to study the energy spectrum of radioactive decays.²⁴

A channel of particular interest is the electron capture event, during which a proton and an electron of a mother atom merge to become a neutron and a neutrino, leaving the daughter atom in an excited state.

The total energy released during the decay is given by the mass difference between the mother and daughter atom, the so called ‘Q-value’. Because the neutrino is the only particle leaving the system, the maximum energy of the excited state is the Q-value minus the elusive rest mass of the neutrino. For this reason the high-energy tail of the spectrum is sensitive to its value.

*A translation of the full letter can be found on www.symmetrymagazine.org.

The ECHo experiment is based around this idea.²⁸ The studied atom here is $^{163}\text{Holmium}$, which decays to $^{163}\text{Dysprosium}$ by capturing an electron. It then relaxes to its ground state, giving off energy to a chemical environment comprised of Gold atoms. The spectrum of the relaxation is measured via calorimeters.

In order to extract the inordinately tiny neutrino mass from this spectrum its theoretical description has to be enormously precise. Recently it has been shown that most features of the spectrum can be reproduced by a simulation of atomic Holmium if the effect of several Auger-Meitner decay channels is added via a self-energy.¹⁰ However, in the experiment the Holmium atom is embedded in a Gold environment, where its valence shells hybridise with the neighbouring atoms. This is expected to have a non-negligible impact on the electron capture spectrum.

The aim of this section is to improve on the results from ref. [10] by replicating the simulation for Holmium-doped Gold (abbr. ‘Au:Ho’) instead of atomic Holmium, and by also including the effect of the environment as a self-energy.

7.2 Atomic Ho vs. Au:Ho

Theory

Atomic Holmium has an electronic configuration of $[\text{Xe}]4f^{11}6s^2$, whereas the two valence shells hybridise with the Gold environment in case of Au:Ho. To emulate this, a relativistic DFT calculation is conducted using FPLO, in which Holmium replaces one of the Gold atoms in a $2 \times 2 \times 2$ fcc supercell* (compare figure 7.1). This replacement induces a small distortion of the atomic positions, which is incorporated without additional parameters using the force relaxation module of FPLO.

The large and small part of the radial functions of the atomic basis of Holmium are contained in the output of FPLO. They are used to calculate the Coulomb interaction \mathcal{Q} and the (atomic) Dirac Hamiltonian $\mathcal{D}_{\text{Ho/Dy}}$ for the potentials created by both the Holmium and Dysprosium core.

The system is then formally split into a main part \mathcal{M} containing all non-hybridising orbitals of Holmium (including $4f$), and an environment \mathcal{E} , comprised of the hybridising Holmium and Gold orbitals ($^{\text{Ho/Au}}6s$, $6p$ and $5d$). The Coulomb operator describing the interaction on the Holmium atom acts on and between those two parts and therefore separates into three operators

$$\mathcal{Q} = \mathcal{Q}_{\mathcal{M}} + \mathcal{Q}_{\mathcal{E}} + \mathcal{Q}_{\mathcal{M}\mathcal{E}} \quad . \quad (7.1)$$

*A calculation for a $3 \times 3 \times 3$ supercell was also attempted, but proved to be beyond the limits of the available hardware.

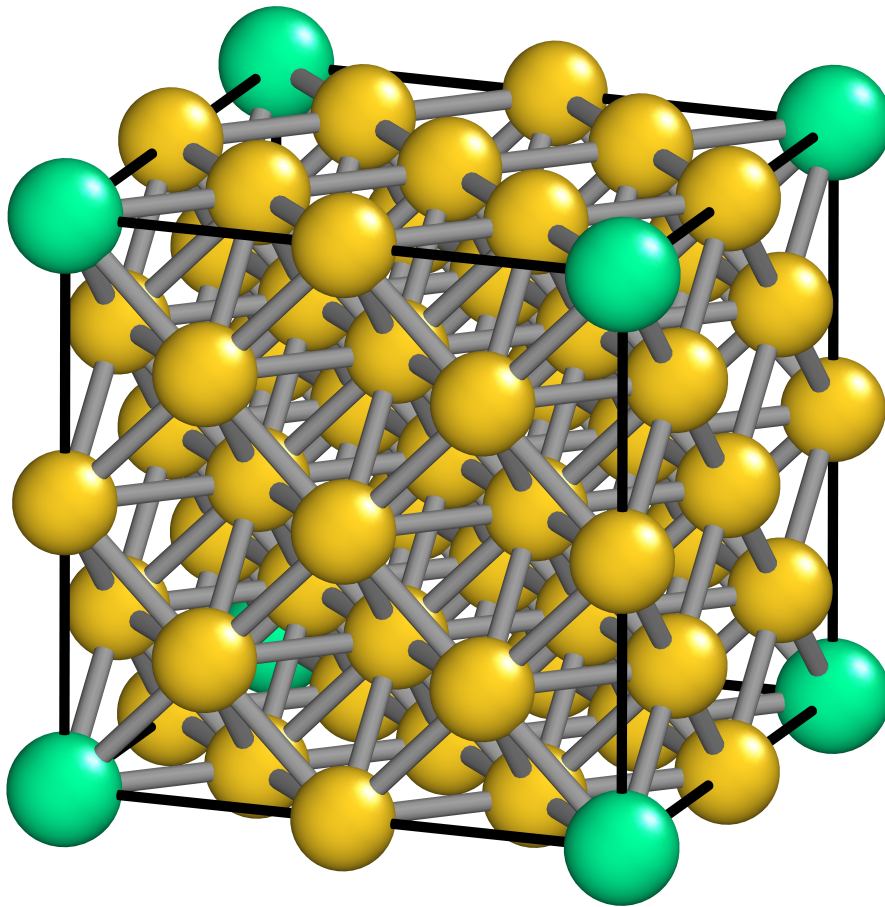


Figure 7.1: The crystal structure of Holmium-doped Gold, with a doping factor of $1/32 \approx 3\%$. The distortion of the atomic positions due to the presence of Holmium is too minuscule to be visible to the naked eye.

In order to have the environment drop out of the calculation as a first approximation, the one-particle density matrix $n_{DFT, Ho}$ of the Holmium atom in a Gold environment is also extracted from the DFT result.* It is used to calculate the mean effect as given

*Except for the occupation of the Ho-4*f* shell, which due to technical reasons is fixed at 10 electrons.

by equation (3.10) that the environment \mathcal{E} has on \mathcal{M} via \mathcal{Q} ,

$$\mathcal{Q}_{\mathcal{M}\mathcal{E}} \rightarrow \overline{\mathcal{Q}}_{\mathcal{M}\mathcal{E}} \rightarrow \overline{\mathcal{Q}}_{\mathcal{M}\mathcal{E}}|_{\mathcal{M}} . \quad (7.2)$$

Note that although all terms of $\mathcal{Q}_{\mathcal{M}\mathcal{E}}$ only act between \mathcal{M} and \mathcal{E} , its mean field version obeys no such restriction. Here $\overline{\mathcal{Q}}_{\mathcal{M}\mathcal{E}}|_{\mathcal{M}}$ denotes the part of $\overline{\mathcal{Q}}_{\mathcal{M}\mathcal{E}}$ only acting on \mathcal{M} . All other parts are ignored for the nonce.

The Hamiltonian for the main part of the mother atom ^{163}Ho and the daughter atom ^{163}Dy in a Gold environment is given by

$$\mathcal{H}_{\text{Ho/Dy}} = \mathcal{D}_{\text{Ho/Dy}}|_{\mathcal{M}} + \mathcal{Q}_{\mathcal{M}} + \overline{\mathcal{Q}}_{\mathcal{M}\mathcal{E}}|_{\mathcal{M}} . \quad (7.3)$$

Their respective approximate eigensystems are found (compare section 4.1), yielding the ground states $|\psi_{0,\text{Ho/Dy}}\rangle$ as their first element.

During the decay process a proton of the atomic core captures an electron and emits a neutrino. Because the only direct effect this event has on the hull is the loss of an electron, it is represented by the operator⁸

$$\mathcal{T}_{EC,j} \stackrel{\text{def}}{=} p_j a_j , \quad (7.4)$$

an annihilation operator multiplied with the square root of the decay probability corresponding to the orbital j . It transforms the electronic Holmium ground state $|\psi_{0,\text{Ho}}\rangle$ to an excited Dysprosium state $\mathcal{T}_{EC,j}|\psi_{0,\text{Ho}}\rangle$. On this level of theory, the energy spectrum of the electron capture process without the effect of the neutrino is, as explained in section 4.2, proportional to the negative imaginary part of the sum of response functions⁹

$$\mathcal{G}(\omega) = \sum_{j,k} \left\langle \psi_{0,\text{Ho}} \left| \mathcal{T}_{EC,j}^\dagger \frac{1}{\omega - \mathcal{H}_{\text{Dy}} + E_0 + i\Gamma} \mathcal{T}_{EC,k} \right| \psi_{0,\text{Ho}} \right\rangle , \quad (7.5)$$

with

$$E_0 = \langle \psi_{0,\text{Dy}} | \mathcal{H}_{\text{Dy}} | \psi_{0,\text{Dy}} \rangle . \quad (7.6)$$

Because of conserved total angular momentum and, after the capture process, also parity, this calculation can be split up into electron capture from an $s^{1/2}$ and $p^{1/2}$ orbital, and into spin up and down. This significantly reduces the required amount of computational power.

The neutrino featured in the decay process carries away energy and thus influences the probabilities for excited daughter states to occur. This effect needs to be included by multiplying the spectrum with the phase space factor⁸

$$f_m(\omega) = \begin{cases} (Q - \omega) \sqrt{(Q - \omega)^2 - m^2 c^4} & , \quad (Q - \omega)^2 \geq m^2 c^4 \\ 0 & , \quad (Q - \omega)^2 < m^2 c^4 \end{cases} \quad (7.7)$$

for a neutrino of mass m , where Q denotes the Q-value and hence total energy gained by the decay process.

In this thesis all electron capture spectra are plotted with the phase space factor

$$f_0(\omega) = (Q - \omega)^2 \quad (7.8)$$

for massless neutrinos, and they are scaled such that their integral coincides with that of the experimental measurement. Because

$$f_0(\omega) \neq 0 \quad \forall \omega < Q \quad , \quad (7.9)$$

adjusting the spectrum to that of a massive neutrino can be achieved by multiplying with⁸

$$\frac{\sum_{a=1}^3 |U_{ae}|^2 f_{m_a}(\omega)}{f_0(\omega)} \quad , \quad (7.10)$$

where the numerator is the phase space factor for three neutrino mass eigenvalues m_a which features the Pontecorvo-Maki-Nakagawa-Sakata matrix U .⁵⁰ The matrix elements U_{ae} transform the state of the electron neutrino from a flavour basis to the basis of mass eigenstates.

Results

The electron capture spectrum of atomic Holmium and Holmium in Gold with an artificial Lorentzian broadening is shown in figure 7.2, and a detailed view of the two largest structures in figure 7.3. The spectrum of atomic Holmium was calculated by Martin Braß (compare ref. [8]), and the experimental spectrum was analysed and published in ref. [75].

The Q-value is given by $Q = 2838 \text{ eV}$ ⁷⁶ and the approximate eigenstate spanned by 100 Krylov states per spin and angular momentum of the captured electron. The broadening of $\Gamma = 4 \text{ eV}$ (compare equation (7.5)) is chosen purely to fit the experimental measurement.

It can be seen that all major peaks in the experimentally accessible energy range as well as their satellite structures are reproduced. They are labelled with the shells of the captured electron in the states responsible for them.

However, a closer inspection reveals that the theoretical peak energies do not quite agree with the experimental ones. This effect cannot be explained by a total offset, as the peaks at higher energies tend to deviate further than the lower ones. This effect is stronger for atomic Holmium than for Holmium in Gold. The major

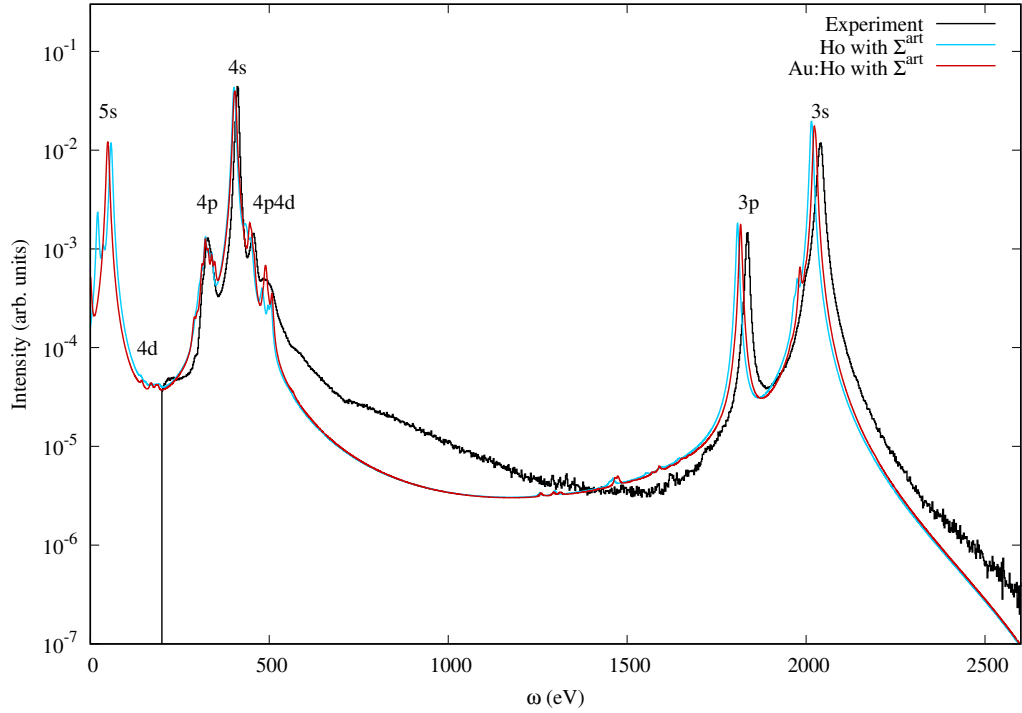


Figure 7.2: The electron capture spectrum of Holmium in Gold as measured experimentally (black), and with an artificial Lorentzian broadening of $\Gamma = 4 \text{ eV}$ for atomic Holmium (turquoise) and Holmium in Gold (red).

peaks are all closer to their true experimental energy in case of the latter. The atomic and embedded peak positions differ by almost 9 eV in case of the peak labelled $3s$. This shows that already on this level of theory the implicit inclusion of the Gold environment significantly improves the result. The $3s$ capture peak is of special significance, because it dominates the form of the spectral endpoint, which is the part most strongly influenced by the mass of the electron neutrino.

The height of the peaks is overestimated in some cases, and underestimated in others, suggesting that the true peak broadening is not constant. This can also be seen by comparing the widths of the experimentally measured peaks labelled $3s$ and $4s$. The two calculations roughly agree on the heights of the major peaks, but the minor ones exhibit some differences.

The largest discrepancy between theory and experiment is of course found in

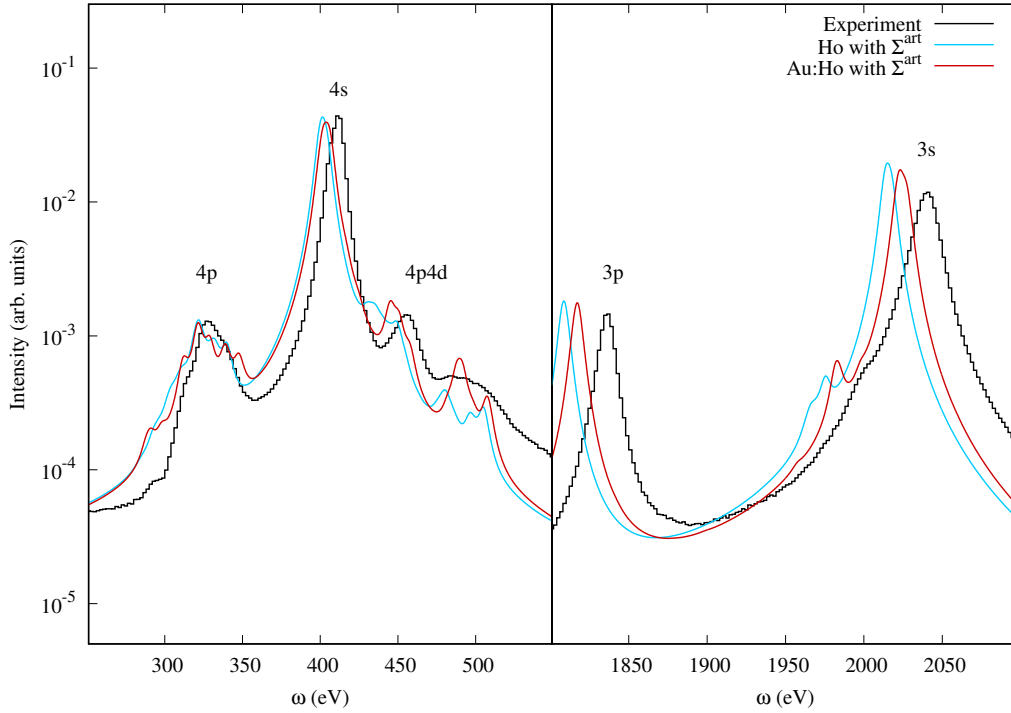


Figure 7.3: Details of the electron capture spectrum of Holmium in Gold as measured experimentally (black), and with an artificial Lorentzian broadening of $\Gamma = 4 eV$ for atomic Holmium (turquoise) and Holmium in Gold (red).

the region between $500 eV$ and $1700 eV$. As all peaks here have almost negligible spectral weight, it is dominated by the shape of the large capture peak labelled $4s$, which is experimentally shown to have an asymmetric high-energy broadening tail.

The method of spectral calculation with an energy independent broadening is inherently incapable of reproducing this asymmetry. Furthermore, the endpoint of the spectrum strongly depends on the comparably arbitrary choice of Γ .

Sufficiently precise experimental agreement of an *ab initio* calculation can therefore not be achieved without including some of the so far neglected decay mechanisms. These lead to a peak-specific and energy-dependent broadening, which is found by calculating the self-energy of the spectral peaks.

7.3 Self-energy due to Auger-Meitner decay

Theory

One important relaxation channel not yet included in the simulation is that of Auger-Meitner decay. There, the core hole created by the electron capture event is occupied by a particle from a higher shell, which donates enough energy to another electron that it is no longer bound to the atom (compare figure 4.1).

Explicitly incorporating the continuum orbitals in the calculation is far from computationally feasible, but their effect can instead be included as a self-energy, as explained in section 4.3. The response function given by equation (7.5) then becomes¹⁰

$$\mathcal{G}(\omega) = \sum_{j,k,l} \langle \psi | \mathcal{T}_{EC,j}^\dagger | E_k \rangle \frac{1}{\omega - E_k \delta_{k,l} + E_0 - \Sigma_{k,l}^{AM}(\omega)} \langle E_l | \mathcal{T}_{EC,j} | \psi \rangle, \quad (7.11)$$

with the self-energy due to Auger-Meitner decay*

$$\Sigma_{k,l}^{AM}(\omega) = \left\langle E_k \left| \mathcal{U}_{AM}^\dagger \frac{1}{\omega + E_0 + i\Gamma - \mathcal{H}_{Dy} - \mathcal{H}_C} \mathcal{U}_{AM} \right| E_l \right\rangle. \quad (7.12)$$

Here, $\{|E_k\rangle\}$ is an approximate eigensystem found by diagonalising the Hamiltonian on a subspace spanned by a Krylov basis of appropriate size. The operator \mathcal{H}_C is the Hamiltonian of the continuum of unbound electrons, approximated using a one-particle basis comprised of a finite number of eigen-differentials, which sample the continuum orbitals (compare section 5.2 in ref. [8]). The operator

$$\mathcal{U}_{AM} = \sum_{j,k,l,m} \alpha_{m,j,l,k} a_m^\dagger a_j^\dagger a_k a_l + h.c. \quad (7.13)$$

is a part of the Coulomb interaction between the bound states and the unbound eigen-differentials. It describes Auger-Meitner decay, in which a continuum electron with index m is created.

Because $\{\mathcal{U}_{AM} | E_k\rangle\}$ is in general not an eigensystem of the combined Hamiltonian $\mathcal{H}_{Dy} + \mathcal{H}_C$, the self-energy can be non-diagonal. This mixes different eigenstates of \mathcal{H}_{Dy} in equation (7.11), which is known as Fano's effect.²³

*Formally, the eigenstates $|E_l\rangle$ of the bound system need to be replaced by the tensor product $|E_l\rangle \otimes |\psi_{C,0}\rangle$ with the groundstate of the continuum. However, because the latter is assumed to be empty, this was refrained from to ease notation.

The full Hamiltonian $\mathcal{H}_{Dy} + \mathcal{H}_C$ conserves the relativistic quantum number

$$\kappa = \underbrace{2(l-j)}_{=\text{sgn}(l-j)} \left(j + \frac{1}{2} \right) \quad (7.14)$$

of a created Auger-Meitner electron, which contains information about the total angular momentum j of the electron and its orientation relative to spin. By splitting up the Auger-Meitner decay operator \mathcal{U} into

$$\mathcal{U}_{AM} = \sum_{\kappa} \mathcal{U}_{\kappa} \quad , \quad (7.15)$$

where \mathcal{U}_{κ} contains only the terms interacting with a continuum electron with a specific κ , the self-energy can therefore be simplified to

$$\begin{aligned} \Sigma_{k,l}^{AM}(\omega) &= \sum_{\kappa,\kappa'} \left\langle E_k \left| \mathcal{U}_{\kappa'}^{\dagger} \frac{1}{\omega + E_0 + i\Gamma - \mathcal{H}_{Dy} - \mathcal{H}_C} \mathcal{U}_{\kappa} \right| E_l \right\rangle \\ &= \sum_{\kappa} \left\langle E_k \left| \mathcal{U}_{\kappa}^{\dagger} \frac{1}{\omega + E_0 + i\Gamma - \mathcal{H}_{Dy} - \mathcal{H}_C} \mathcal{U}_{\kappa} \right| E_l \right\rangle . \end{aligned} \quad (7.16)$$

To a very good approximation, the unbound electrons do not interact with each other and do not return to the atom. It follows that the continuum Hamiltonian just measures the orbital energies ϵ_m^c , which are given by the entries of the Dirac Hamiltonian in the basis of the unbound eigen-differentials with index m ,

$$\mathcal{H}_C = \sum_{m \in \mathcal{C}} \epsilon_m^c a_m^{\dagger} a_m \quad . \quad (7.17)$$

Therefore a further separation of \mathcal{U}_{AM} ,

$$\mathcal{U}_{\kappa} = \sum_m \mathcal{U}_{\kappa,m} \quad , \quad (7.18)$$

where $\mathcal{U}_{\kappa,m}$ creates a continuum electron with a specific* index m , leads to a further simplification of the self-energy,

$$\begin{aligned} \Sigma_{k,l}^{AM}(\omega) &= \sum_{\kappa,m,n} \left\langle E_k \left| \mathcal{U}_{\kappa,m}^{\dagger} \frac{1}{\omega + E_0 + i\Gamma - \mathcal{H}_{Dy} - \mathcal{H}_C} \mathcal{U}_{\kappa,n} \right| E_l \right\rangle \\ &= \sum_{\kappa,m} \left\langle E_k \left| \mathcal{U}_{\kappa,m}^{\dagger} \frac{1}{\omega + E_0 + i\Gamma - \mathcal{H}_{Dy} - \epsilon_m^c} \mathcal{U}_{\kappa,m} \right| E_l \right\rangle . \end{aligned} \quad (7.19)$$

*The choice of m fixes the choice of κ , but keeping this now redundant notation is in this case more instructive than dropping it.

Because the form of all $\mathcal{U}_{\kappa,m} |E_l\rangle$ for fixed κ only differs by an m dependent prefactor p_m , it is for large parts of the calculation possible to formally restrict \mathcal{U}_κ to only those terms interacting with an arbitrary continuum orbital m' . Sending

$$\mathcal{U}_{\kappa,m} \mapsto \mathcal{U}_{\kappa,m'} \stackrel{\text{def}}{=} \mathcal{U}'_\kappa \quad (7.20)$$

significantly reduces the required computational power, because ϵ_m^c and p_m are now the only objects depending on m , where the former merely introduces an offset to ω and the latter a scaling of the contribution.

The self-energy does not only introduce a broadening of the peaks via its imaginary part, but also an individual shifting and even deformation because of its real part. The implicit inclusion of the new decay channels furthermore creates a total offset to E_0 , because the energy of the Dysprosium ground state is corrected. It is found to be given by $\text{Re}(\Sigma_{00}^{AM}(0))$, the real part of the self-energy for the ground state, evaluated at $\omega = 0$.¹⁰

To numerically access the continuum, a value of $\Gamma = 6 \text{ eV}$ is chosen, and the energies ϵ_m^c are discretised and sampled by 3000 points with a spacing of 2 eV .

After the artificial broadening is replaced with the self-energy and the ground state energy is corrected, the spectrum is calculated and is, as in section 7.2, multiplied by the neutrino phase-space factor of equation (7.7) and normalised to the experimental integral.

Results

Figure 7.4 displays the electron capture spectrum of atomic Holmium and Holmium in Gold, broadened with a self-energy due to Auger-Meitner decay. It incorporates the sum of all channels with values of $\kappa \in \{-1, 1, -2, 2, -3, 3, -4, 4\}$ for the continuum electron. The self-energy for larger values of $|\kappa|$ was also calculated, but did not visibly change the spectrum. The spectrum of atomic Holmium was calculated by Martin Braß (compare ref. [8]). Both spectra are further broadened with a Gaussian of $FWHM = 8 \text{ eV}$ due to experimental uncertainty. The spectrum with an artificial Lorentzian broadening discussed in section 7.2 is also shown for reference. A detailed view of the spectra can be seen in figure 7.5.

The broadening due to the Auger-Meitner decay self-energy contributes several improvements. Most importantly, it much more accurately describes the asymmetric line broadening, and hence the form of the valley between 500 eV and 1700 eV , and of the endpoint.

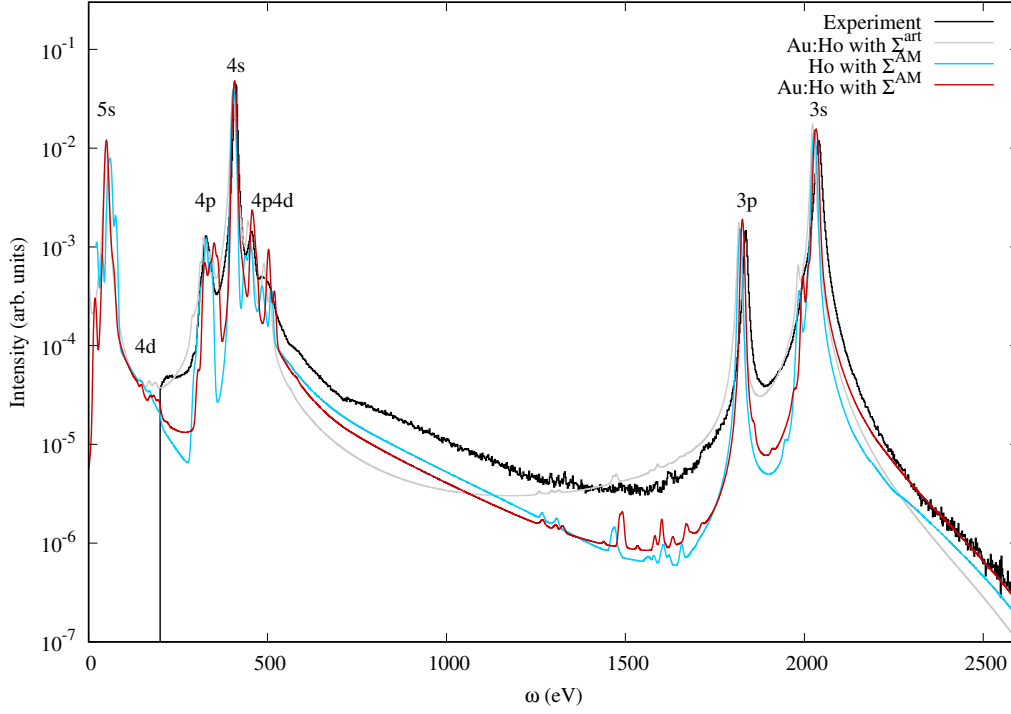


Figure 7.4: The electron capture spectrum of Holmium in Gold as measured experimentally (black), and with an artificial Lorentzian broadening of $\Gamma = 4 \text{ eV}$ (grey). Also shown is the spectrum with broadening due to Auger-Meitner decay and additionally a Gaussian broadening with $FWHM = 8 \text{ eV}$ for atomic Holmium (turquoise) and Holmium in Gold (red).

The peak positions are also corrected by the real part of the self-energy. As in the case of artificial broadening, the major peaks are reproduced better by the calculation for Holmium in Gold than for atomic Holmium.

Apart from the positions the broadening is also closer to the experiment in case of the spectrum implicitly including the Gold environment. The effect is most visible in the valleys around 250 eV , 1500 eV , 1900 eV , and at the important endpoint. This stems from the fact that the altered configuration of the valence shells of Holmium compared to the atomic case opens up new Auger-Meitner decay channels and thus influences the self-energy, as was conjectured in ref. [10].

One interesting feature measured in experiment is a small bump at 700 eV . It is shown in figure 7.6, together with the theoretically calculated spectra with the Auger-Meitner decay self-energy for continuum electrons with a value of $|\kappa|$ up to

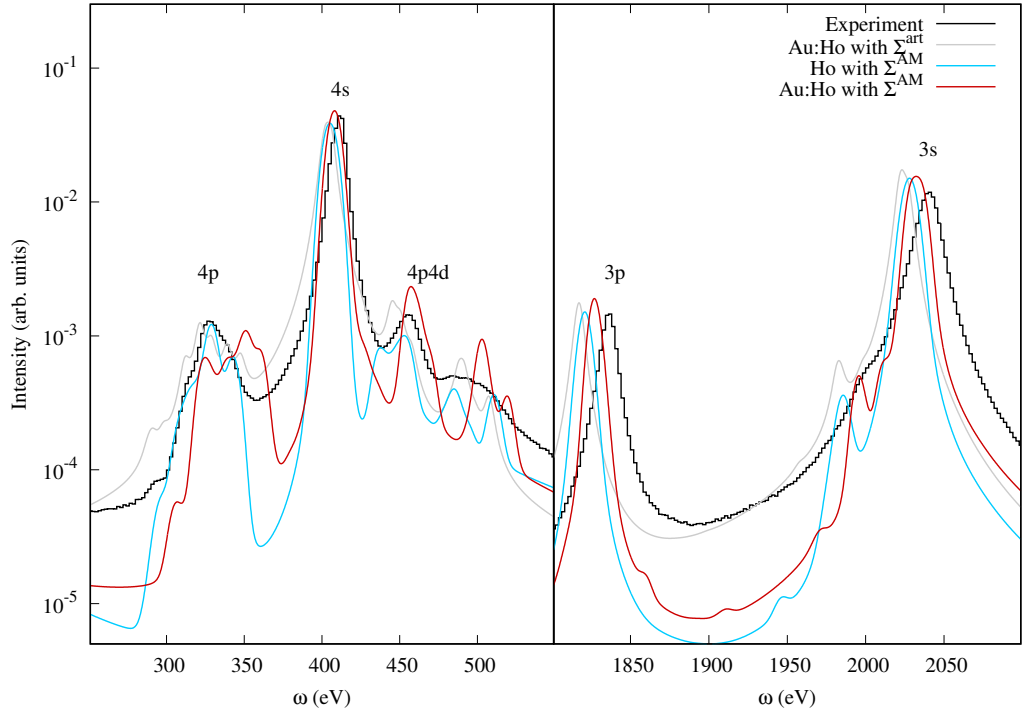


Figure 7.5: Details of the electron capture spectrum of Holmium in Gold as measured experimentally (black), and with an artificial Lorentzian broadening of $\Gamma = 4 \text{ eV}$ (grey). Also shown is the spectrum with broadening due to Auger-Meitner decay and additionally a Gaussian broadening with $FWHM = 8 \text{ eV}$ for atomic Holmium (turquoise) and Holmium in Gold (red).

and including the values 1, 2, 3 and 4. The spectra are in this case not broadened with a Gaussian. The bump is briefly reproduced for $|\kappa| \leq 2$ (orange line, left panel), but is then flattened out when including $\kappa = \pm 3$ (turquoise line). A much larger bump that is not found in experiment is analogously produced and flattened at 2150 eV (compare right panel), suggesting that the feature at 700 eV might be mere coincidence. However, the bump at larger energies can also be observed in case of the atomic calculation, while this is not the case for the one at lower energy (not depicted).

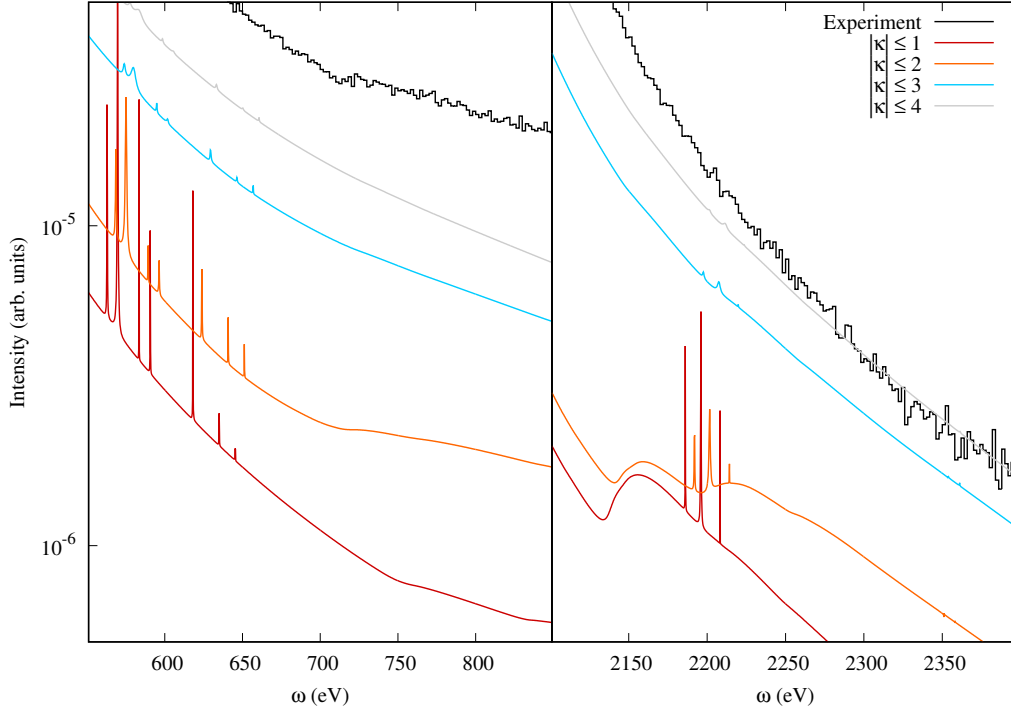


Figure 7.6: Details of the electron capture spectrum of Holmium in Gold as measured experimentally (black), and with broadening due to Auger-Meitner decay, including continuum electrons up to various values of κ .

7.4 Self-energy due to the Gold environment

Theory

In section 7.2 the system was split into a main part \mathcal{M} and an environment \mathcal{E} , the latter of which was subsequently neglected except for its effect via a mean field Coulomb interaction. Re-introducing \mathcal{E} to the system gives a correction to equation (7.5) in form of a self-energy $\Sigma^{\mathcal{E}}$, completely analogous to the Auger-Meitner decay correction in equation (7.11). Under the assumption that the two effects are not coupled, the total of these corrections is mathematically represented by $\Sigma^{AM} + \Sigma^{\mathcal{E}}$ (compare section 4.3).

The self-energy resulting from the effect of the environment is given by*

$$\Sigma_{k,l}^{\mathcal{E}}(\omega) = \left\langle E_k \otimes \psi_{\mathcal{E},0} \left| \mathcal{U}_{\mathcal{M}\mathcal{E}}^\dagger \frac{1}{\omega + E_0 + i\Gamma - \mathcal{H}_x} \mathcal{U}_{\mathcal{M}\mathcal{E}} \right| E_l \otimes \psi_{\mathcal{E},0} \right\rangle \quad (7.21)$$

with

$$\mathcal{H}_x \stackrel{\text{def}}{=} \mathcal{H}_{Dy} + \mathcal{H}_{\mathcal{E}} + \mathcal{H}_{\mathcal{M}\mathcal{E}} \quad , \quad (7.22)$$

where $\mathcal{H}_{\mathcal{E}}$ is the part of the Hamiltonian only acting on \mathcal{E} , $\mathcal{H}_{\mathcal{M}\mathcal{E}}$ acting between \mathcal{M} and \mathcal{E} , $|\psi_{\mathcal{E},0}\rangle$ is the ground state of the unperturbed environment, and $\mathcal{U}_{\mathcal{M}\mathcal{E}}$ comprises any interaction with previously unreachable states and is characterised below.

To cope with the enormous number of possible configurations two important approximations have to be made. The first is to treat both $\mathcal{H}_{\mathcal{E}}$ and $\mathcal{U}_{\mathcal{M}\mathcal{E}}$ on a mean field level, transforming them into $\overline{\mathcal{H}}_{\mathcal{E},k}$ and $\overline{\mathcal{U}}_{\mathcal{M}\mathcal{E},k}$, respectively. This introduces a dependence of the operators on the one-particle density matrix induced by the states $|E_k\rangle$. The second approximation is to assume that the effect that $\mathcal{H}_{\mathcal{M}\mathcal{E}}$ and any operator $\overline{\mathcal{U}}_{\mathcal{M}\mathcal{E},k}$ has on \mathcal{M} is negligible,

$$\mathcal{H}_{\mathcal{M}\mathcal{E}} = 0 \quad , \quad \overline{\mathcal{U}}_{\mathcal{M}\mathcal{E},k} = \overline{\mathcal{U}}_{\mathcal{E},k} \otimes \mathbb{1}_{\mathcal{M}} \quad . \quad (7.23)$$

As all $|E_k\rangle$ are orthonormal to one another it follows that the self-energy is diagonal,

$$\Sigma_{k,l}^{\mathcal{E}}(\omega) = \delta_{k,l} \Sigma_{k,k}^{\mathcal{E}}(\omega) \stackrel{\text{def}}{=} \delta_{k,l} \Sigma_k^{\mathcal{E}}(\omega) \quad , \quad (7.24)$$

with

$$\Sigma_k^{\mathcal{E}}(\omega) = \left\langle \psi_{\mathcal{E},0} \left| \overline{\mathcal{U}}_{\mathcal{E},k}^\dagger \frac{1}{\omega + E_0 + i\Gamma - E_k - \overline{\mathcal{H}}_{\mathcal{E},k}} \overline{\mathcal{U}}_{\mathcal{E},k} \right| \psi_{\mathcal{E},0} \right\rangle \quad . \quad (7.25)$$

Hence the choice of density matrix used to calculate the mean field version of the operators becomes unique for every entry of $\Sigma_k^{\mathcal{E}}$. It can be calculated via

$$\left(n_{|E_k\rangle} \right)_{m,n} = \left\langle E_k \otimes \psi_{\mathcal{E},0} \left| a_m^\dagger a_n \right| E_k \otimes \psi_{\mathcal{E},0} \right\rangle \quad . \quad (7.26)$$

*Because the ground state $|\psi_{\mathcal{E},0}\rangle$ of the unperturbed environment is non-trivial it is explicitly included in the notation via $|E_k \otimes \psi_{\mathcal{E},0}\rangle \stackrel{\text{def}}{=} |E_k\rangle \otimes |\psi_{\mathcal{E},0}\rangle$ here.

The environmental Hamiltonian can in this approximation be written down as

$$\begin{aligned} \overline{\mathcal{H}}_{\mathcal{E},k} = & \mathcal{H}_{DFT} + \mathcal{D}_{Dy} - \mathcal{D}_{Ho} \\ & + \overline{\mathcal{Q}}_{\mathcal{M}\mathcal{E}}|_{\mathcal{E}} \left(n_{|E_k\rangle} \right) - \overline{\mathcal{Q}}_{\mathcal{M}\mathcal{E}}|_{\mathcal{E}} \left(n_{|\psi_{0,Ho}\rangle} \right) \quad , \end{aligned} \quad (7.27)$$

where \mathcal{H}_{DFT} is an effective Hamiltonian as read in from FPLO (compare section 3.1), which describes the unperturbed $6s$, $6p$ and $5d$ shell of a central Holmium atom and all Gold atoms contained in an effective molecule in form of a sphere with a radius of $15.1 a_B$. The operator $\overline{\mathcal{Q}}_{\mathcal{M}\mathcal{E}}|_{\mathcal{E}}(n)$ is the mean field version of the Coulomb interaction acting between \mathcal{M} and \mathcal{E} , restricted to \mathcal{E} (compare equation (7.1)). It is found according to equation (3.10).

The extra terms added to \mathcal{H}_{DFT} correct both the Dirac Hamiltonian, which changes due to the decreased charge of the atomic core, and the effective mean field Coulomb interaction, which is altered by the loss of an electron. The result is a proper description of Dysprosium in a Gold environment.

The operator $\mathcal{U}_{\mathcal{E}}$ is given by the coupling between the subspace spanned by $\{|E_k \otimes \psi_{\mathcal{E},0}\rangle\}$ and the subspace reached by acting on it with $\mathcal{H}_{\mathcal{E}}$. Because of the approximations this coupling operator can be written as

$$\overline{\mathcal{U}}_{\mathcal{E},k} = \overline{\mathcal{H}}_{\mathcal{E},k} - \mathcal{C}_k \quad , \quad (7.28)$$

where \mathcal{C}_k comprises all parts of $\overline{\mathcal{H}}_{\mathcal{E},k}$ that project the unperturbed ground state $|\psi_{\mathcal{E},0}\rangle$ on a multiple of itself. As \mathcal{H}_{DFT} , the Hamiltonian of the unperturbed environment, is a one-particle operator, it is straightforward to find the rotation that diagonalises it. In this basis $|\psi_{\mathcal{E},0}\rangle$ is given by a single Slater-determinant, and \mathcal{C}_k is consequently given by the diagonal entries of $\overline{\mathcal{H}}_{\mathcal{E},k}$.

As in the case of Auger-Meitner decay, $\text{Re}\Sigma_{00}^{\mathcal{E}}(0)$, the real part of the self-energy of the Dysprosium ground state evaluated at $\omega = 0$, further corrects the ground state energy E_0 .

For the numerical calculation a value of $\Gamma = 6 eV$ is picked, and the Lánczos algorithm (compare section 2.3) applied to \mathcal{H}_{DFT} , with the three Holmium shells as the first block and 30 additional blocks describing the environment. Because of the size of the Hilbert space a further restriction to the subspace with a maximum of one electron in the orbitals above the Fermi energy is necessary.

After the Auger-Meitner decay self-energy and the ground state energy are corrected by the influence of the environment, the spectrum is extracted from the response function and is, as in section 7.2, multiplied by the neutrino phase-space factor of equation (7.7) and normalised to the experimental integral.

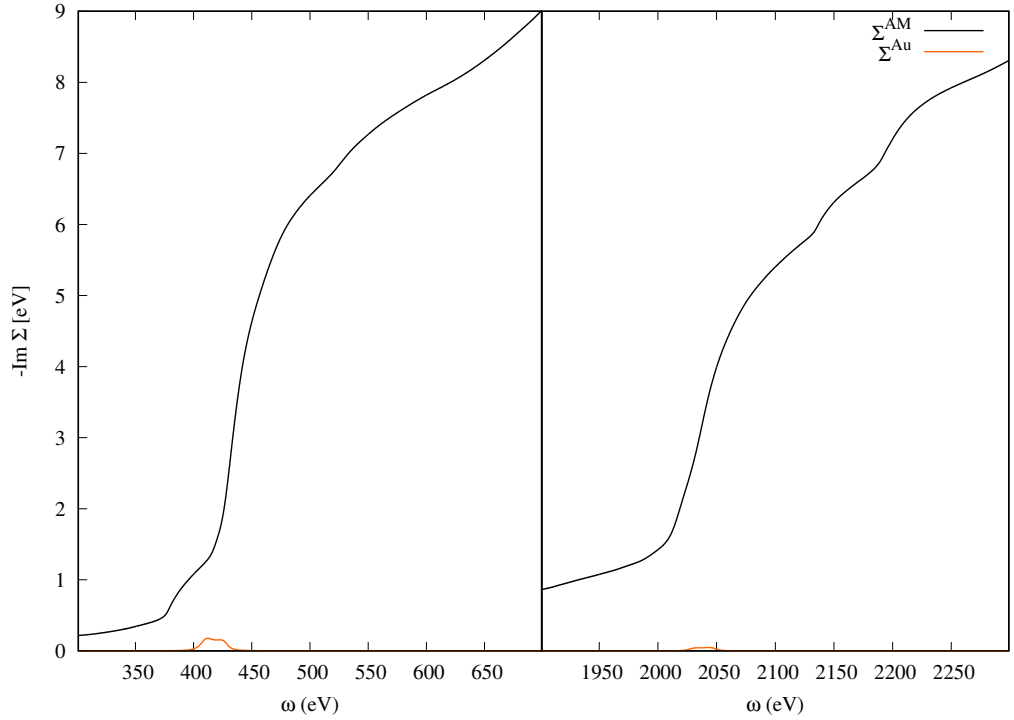


Figure 7.7: Details of the diagonal entries of the self-energy of Holmium in Gold due to Auger-Meitner decay (black) and the Gold environment (orange), for a peak at 402 eV (left) and 2023 eV (right).

Results

An excerpt of the self-energy Σ^{AM} due to Auger-Meitner decay as well as the environmental self-energy $\Sigma^{\mathcal{E}} = \Sigma^{Au}$ for the case of Holmium-doped Gold are shown in an exemplary plot in figure 7.7. Displayed is the negative imaginary part, which is responsible for the peak broadening. It is shown here for the approximate eigenstates of the uncorrected Dysprosium Hamiltonian corresponding to energies 402 eV and 2023 eV. The states are responsible for the emergence of the major peaks corresponding to an electron capture process from the 3s and 4s orbital, respectively.

For both (and all other) states the self-energy caused by the Gold environment is approximately a single, slightly lopsided peak with a height of about 0.1 eV, seated at the position of the corresponding eigenenergy. The self-energy due to Auger-

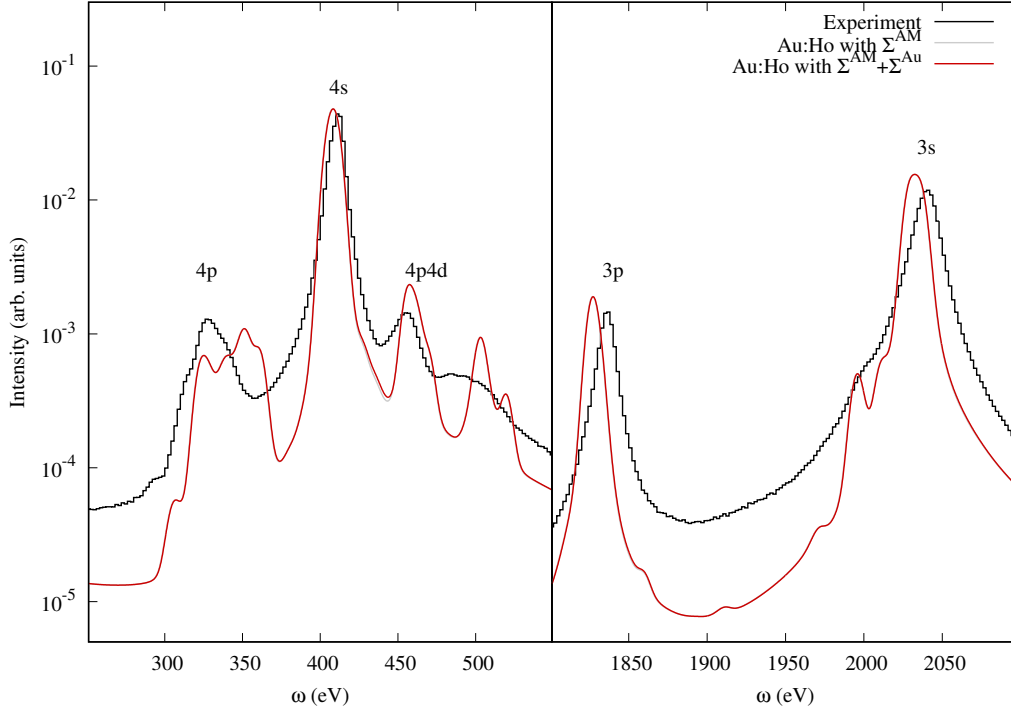


Figure 7.8: Details of the electron capture spectrum of Holmium in Gold as measured experimentally (black), with broadening due to Auger-Meitner decay (grey), and with additional broadening due to the Gold environment (red). The theoretical spectra are further broadened by a Gaussian with $FWHM = 8 eV$.

Meitner decay on the other hand takes on values on the orders of $1 eV$ to $10 eV$. In contrast to the Gold self-energy it does not or only slowly fall off with increasing energy.

This means that Σ^{Au} , in its current theoretical implementation, is almost irrelevant for the shape of the spectrum. This is confirmed by figure 7.8, where only a small difference between the spectra around $450 eV$ is visible to the naked eye. It therefore stands to reason that the approximations made to decrease the computational time are too crude. Especially neglecting any direct interaction between the main part and the environment disregards numerous relaxation channels, all of which contribute to the self-energy.

If these were included, the imaginary part of Σ^{Au} is expected to be of the same order of magnitude as Σ^{AM} at the position of the peak, or even dominate there. It

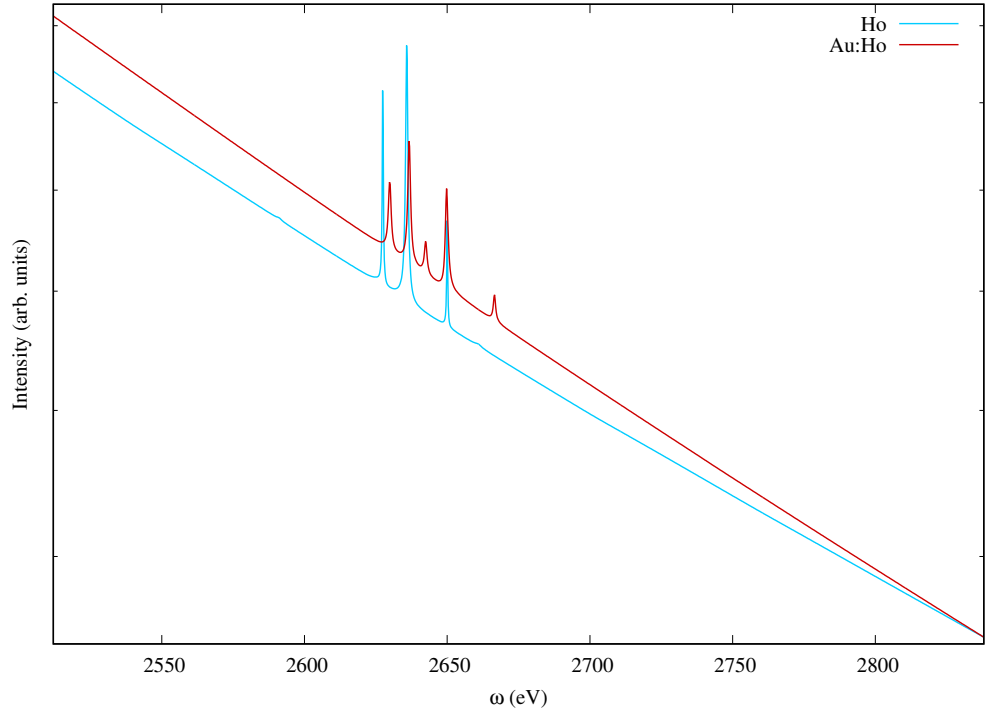


Figure 7.9: The endpoint of the electron capture spectrum without the neutrino phase space factor, for atomic Holmium (turquoise) and Au:Ho (red). The spectra are broadened with Auger-Meitner decay self-energy and, in the latter case, the environmental self-energy. The intensity is plotted logarithmically and the curves are scaled to agree at the Q-value.

is not expected to have a significant effect on the form of the tails of the peaks at higher energies.

The endpoint of the spectrum, which contains information about the rest mass of the electron neutrino, is depicted in figure 7.9 for both the calculation of atomic Holmium as well as for Au:Ho. It is shown there without the phase space factor of the neutrino (compare equation (7.7)). The logarithmic plot clearly shows that both spectra follow an exponential decay law, but with different damping constants.

This confirms the conjecture made in ref. [10], which states that the inclusion of the gold environment does not change the qualitative behaviour of the spectrum at the end point. It is hence comparably easy to extract the rest mass of the electron neutrino from experimental data with sufficient accuracy, which manifests as a deviation from the exponential falloff found after dividing by the phase space factor

for massless particles.

7.5 Discussion

The electron capture spectrum of Holmium in Gold was calculated with an artificial Lorentzian broadening, with a self-energy due to Auger-Meitner decay, and an additional self-energy caused by the environment. The first two spectra were compared to a calculation of atomic Holmium.

The comparison showed that already without any self-energy the inclusion of the Gold environment in the calculation on a mean field level improved the agreement with the experiment, as the peak energies were more accurately reproduced.

This improvement carried over to the calculation with *ab initio* broadening due to the Auger-Meitner decay self-energy. As had been conjectured in ref. [10], not only the peak energies were corrected by the effect of the environment, but also their line shape. Especially the form of the peak labelled 3s, which dominates the endpoint and hence strongly influences the determination of the neutrino mass, experienced a crucial gain in agreement with the experiment compared to the atomic calculation.

The inclusion of the environment furthermore gave rise to a bump around 700 eV, which can also be seen in the experiment. However, this feature only appeared in calculations that did not include all relevant Auger-Meitner decay channels and was not visible in the final spectrum. Its physical meaning hence remains an open question.

Finally, the broadening due to excitations in the Gold environment was included in the calculation via an additional self-energy. It turned out to be miniscule, which can be attributed to the approximation of not directly interacting main part and environment. The small effect the self-energy had was shown to only affect the shape of the peaks themselves, but not their tails.

It was demonstrated that the endpoint of the spectrum continued to fall off exponentially when dividing out the phase space factor of the neutrino of the spectrum broadened by both Auger-Meitner decay and the Gold environment. However, it was shown to fall off slightly steeper than in the atomic case.

The most obvious improvement to be made is to allow some direct interaction between the main part and the environment. It is expected to increase the imaginary part of the self-energy by at least one order of magnitude, such that it possibly dominates the spectrum close to the peak.

One effect not yet included in the calculation is the broadening caused by spontaneous fluorescence decay, during which an electron is de-excited and a photon

emitted. However, it has recently been shown⁵⁵ that this broadening, while important for many atoms, is insignificant in case of ¹⁶³Holmium.

Another path of possible improvement is to relax some of the simplifying assumptions made for the inclusion of the self-energy due to the Gold environment. Allowing two instead of one excited electron beyond the Fermi energy might change the shape of the imaginary part, and hence the broadening. However, for systems with less Krylov states tests show that relaxing these restrictions has only little effect on the self-energy.

If some mathematical trick or sheer calculation power allows to make this adjustment, it may be advantageous to treat the operators governing the environment on a level beyond mean field.

The Hamiltonian was obtained from an FPLO calculation in which Holmium replaced one of the 32 Gold atoms in a $3 \times 3 \times 3$ supercell of its face-centred cubic lattice. While the doping factor of about 3% roughly corresponds to that in the experiment, it is not at all certain that the foreign atom adopts this particular position in the supercell. Holmium might for example instead push the atoms around it aside, effectively replacing four Gold atoms instead of one. Recalculating the spectrum for this alternative configuration could well grant new insights.

The ECHo experiment will be modified in the future, leading to higher resolution. To keep up with the achieved precision, the theoretical description needs to be adapted to the new setups. At some point, the experimental spectrum will likely have been measured using Holmium-doped Silver. With the techniques developed in this section it is straightforward to perform an *ab initio* calculation of the effect of this and any other new environment that Holmium is subjected to, in order to one day find the mass of the electron neutrino.

Part III
Conclusions

8 Summary of Results and Outlook

Starting from mean field Density Functional Theory calculations the theoretical methods were improved to become the full many-body simulations required for this thesis. By pushing the limits of available calculation power it was possible to give an accurate description of the physical properties of various compounds. For all three systems under scrutiny the theory was refined step by step, thus revealing which level of theory is necessary to explain which feature.

In the case of Nickel^{II}oxide a prediction for the ultrafast dynamics of the crystal under the influence of a driving laser was made. Varying the parameters of this laser showed under which conditions the system behaves approximately Rabi-like, and when charge-transfer excitations are most likely to occur. Spin-flips were observed to be suppressed.

By using the GKSL equation, the theoretical description was enabled to include the effect of an idealised Auger-Meitner decay mechanism in the time evolution. It predicted that orbital excitations decrease, while charge-transfer excitations are amplified.

The second system whose interaction with a laser beam was described was Sulphur-hexafluoride. The area ratio and energy splitting of the two components of a peak doublet in the X-ray absorption spectrum was related to the effective exchange interaction energy, which could be tuned by increasing the laser intensity.

A few-configuration model was used to quantify the exchange energy and show that it was increased by 50% in the experiment. It was further able to accurately reproduce the ratio and splitting after fitting its parameters to only two data points. A many-body simulation showed that an *ab initio* treatment of the effect is possible, and even revealed information about the duration of the X-ray pulse.

Holmium-doped Gold formed the last studied system, for which the electron capture spectrum was calculated. The effect of Auger-Meitner decay was here included as a self-energy correction to the spectrum, to find the form of the energy peaks in an *ab initio* fashion.

The effect of the Gold environment was also included as a self-energy, resulting

in a very small additional broadening. The strongest effect was that already the implicit inclusion of the environment on a mean field level induced a significant improvement on the line shape found by the Auger-Meitner decay self-energy alone.

Several suggestions for improving the theories of the three systems were made. They will benefit most from connecting them with one another: The methods applied to SF₆ could be used to accurately predict the electric dipole moments of Ni^{II}O, and those of Au:Ho can enable an *ab initio* calculation of the Auger-Meitner decay operator. The inclusion of this mechanism in the SF₆ calculations either in the GKSL equation or as a self-energy can help to better explain the broadening of the X-ray absorption spectrum. Finally, a time-domain simulation of the relaxation process in Au:Ho after an electron capture event can lead to the discovery and understanding of yet not included phenomena, and subsequently to a better description of the spectrum.

Equipped with this solid and versatile construct of theoretical many-body physics it may eventually be possible to control reactions on a sub-nucleonic timescale using lasers in chemistry, and to find the mass of the electron neutrino in particle physics.

*“In nature’s infinite book of secrecy
A little I can read.”*

-Antony and Cleopatra, Act 1, Scene 2

9 Acknowledgements

Although I am the only author of this work, modern physics is always a group effort. Finishing this thesis would not have been enjoyable, I daresay not even possible, without the people around me.

I owe gratitude to my supervisor Maurits Haverkort, who sent me on this journey. His intuitive approach to physics is fascinating and inspiring, and he often pointed me in completely unexpected directions. I am grateful for his trust to employ me as a PhD student and to let me work on his brainchild QUANTY.

Although he was officially not my supervisor, Martin Braß could easily have been one for me. Whenever I was stuck he listened patiently and with genuine interest, and then either offered most helpful advice or shared my frustration. Most of all, however, he was, and is, a close friend.

Our cosy PhD student group would not be complete without Marc Merstorf. I thank him for numerous highly intellectual discussions about physics and music, and also for sometimes being as frustrated as I was.

I am grateful for the many forms of help provided by Nadejda Bouldi, be it proof-reading a paper, rehearsing a talk or discussing FPLO. I am especially amazed that she continued to be of help even after the birth of her child.

The weekly group meetings established during the last year of my studies were also of great help for me, as they provided new insights on several levels. For this my thanks extend also to the master and bachelor students of our group.

I thank Patrick Rupprecht for the close and fruitful collaboration on Sulphur-hexafluoride. He tirelessly wrote and rewrote the text for the publication, fitted spectrum after spectrum I sent him, and corrected several mistakes I made. In short, working with him was a blast.

Moritz Drescher, quickest finder of absurd counterexamples, Victor Ksoll, CR4 Memeball, and Johannes Hölck, bottomless pit of useless knowledge, all deserve my gratitude for countless discussions during lunch. This daily dose of nonsense was an important tradition for me until a certain pandemic quenched it.

Realistically simulating the physics of molecules and crystals is a fascinating

topic – if you are well acquainted with the matter. Otherwise, this thesis is probably 109 pages of gibberish. My gratitude goes to Dennis Reichard, who proof-read it anyway.

Carolin Krejtscha shall be thanked for her support and helpful suggestions. Finishing this thesis would have been possible without her, but I don't think I would have enjoyed the process quite as much.

I cannot find the adequate words to express my gratitude towards my parents and grandparents. They promised unconditional support, and, amazingly, they kept their word.

The last lines of this section are devoted to Melina and Lisa. Again, words are not well suited to express my feelings for you. Thank you for sharing your lives with me.

Appendices

List of Abbreviations

- AM decay — Auger-Meitner decay
- Au:Ho — Holmium-doped Gold
- CFT — Crystal Field Theory
- DFT — Density Functional Theory
- ELF — Extended Ligand Field Theory
- FPLO — Full-Potential Local-Orbital
- FWHM — full width at half maximum
- GKSL equation — Gorini-Kossakowski-Sudarshan-Lindblad equation
- IR — infrared
- LFT — Ligand Field Theory
- MF — mean field
- MO — molecular orbitals
- Ni^{II}O — Nickel^{II}oxide
- NORI — Natural-Orbital Representation of the Impurity Model
- RASCI — Restricted Active Space Configuration Interaction
- SF₆ — Sulphur-hexafluoride
- XAS — X-ray absorption spectrum

List of Publications

- [43] A. KOMNIK AND S. HEINZE, *Analytical results for the Green's functions of lattice fermions*, Physical Review B, 96 (2017), p. 155103.

[Not used in this thesis.]

- [68] P. RUPPRECHT, L. AUFLEGER, S. HEINZE, A. MAGUNIA, T. DING, M. REBHOLZ, S. AMBERG, N. MOLLOV, F. HEINRICH, M. W. HAVERKORT, C. OTT, AND T. PFEIFER, *Laser control of multi-electron interaction in molecules*. Submitted to *Science* (as report).

I supported the principal author in applying the few-configuration model, and created the *ab initio* simulation as well as several visualisations. I also contributed most of the theoretical parts to the supplements.

List of Figures

4.1	Feynman diagram and schematic representation of Auger-Meitner decay	38
5.1	Partial occupations of the Ni ^{II} O 2 state system at const. polarisation	46
5.2	Partial occupations of Ni ^{II} O in CFT at const. polarisation	48
5.3	Partial occupations of Ni ^{II} O in LFT at const. polarisation	50
5.4	Partial occupations of Ni ^{II} O in LFT at $\mathbb{E} = 76 fV_s/a_B$	51
5.5	Spectra of Ni ^{II} O and Fourier-transforms of laser pulses	52
5.6	Partial occupations of Ni ^{II} O at const. polarisation and $\mathbb{E} = 38 fV_s/a_B$	54
5.7	Partial occupations of Ni ^{II} O at const. polarisation and $\mathbb{E} = 76 fV_s/a_B$	55
5.8	Partial occupations of Ni ^{II} O at const. polarisation and $\mathbb{E} = 152 fV_s/a_B$	56
5.9	Partial occupations of Ni ^{II} O at const. polarisation and $\mathbb{E} = 304 fV_s/a_B$	57

5.10	Spin of Ni ^{II} O at const. polarisation	58
5.11	Spin of Ni ^{II} O at $\mathbb{E} = 76 fVs/a_B$	59
6.1	Molecular structure of SF ₆	67
6.2	Electronic structure of SF ₆	68
6.3	X-ray absorption spectrum of SF ₆	70
6.4	Peak ratio of SF ₆ from experiment and few-configuration fit	72
6.5	Peak splitting of SF ₆ from experiment and few-configuration fit	73
6.6	Plot of electron and Coulomb densities at varying fields for SF ₆	74
6.7	Effective exchange energy of SF ₆ from experiment and simulation	78
6.8	Peak ratio of SF ₆ from experiment and simulation	79
6.9	Peak splitting of SF ₆ from experiment and simulation	80
7.1	Crystal structure of Au:Ho	85
7.2	EC spectrum of Au:Ho with Σ^{art}	88
7.3	Details of EC spectrum of Au:Ho with Σ^{art}	89
7.4	EC spectrum of Au:Ho with Σ^{AM}	93
7.5	Details of EC spectrum of Au:Ho with Σ^{AM}	94
7.6	Details of EC spectrum of Au:Ho for different κ	95
7.7	Self-energies of Au:Ho	98
7.8	Details of EC spectrum of Au:Ho with $\Sigma^{AM} + \Sigma^{Au}$	99
7.9	Endpoint of the EC spectrum of Au:Ho without phase space factor	100

List of Tables

5.1	Parameters for the laser exciting Ni ^{II} O	44
5.2	Parameters for different levels of theory for Ni ^{II} O	47
6.1	Parameters of the few-configuration fit of SF ₆	71
6.2	Dipole moments and Coulomb integrals between SF ₆ MOs	77

Bibliography

- [1] Q. R. AHMAD, R. C. ALLEN, T. C. ANDERSEN, ET AL., *Measurement of the rate of $\nu_e + d \rightarrow p + p + e^-$ interactions produced by ^8B solar neutrinos at the Sudbury Neutrino Observatory*, Physical Review Letters, 87 (2001), p. 071301.
- [2] ———, *Direct evidence for neutrino flavor transformation from neutral-current interactions in the Sudbury Neutrino Observatory*, Physical review letters, 89 (2002), p. 011301.
- [3] P. W. ANDERSON, *More is different*, Science, 177 (1972), pp. 393–396.
- [4] P. AUGER, *Sur les rayons β secondaires produits dans un gaz par des rayons X.*, CR Acad. Sci.(F), 177 (1923), p. 169.
- [5] H. BETHE, *Termaufspaltung in Kristallen*, Annalen der Physik, 395 (1929), pp. 133–208.
- [6] M. BORN AND R. OPPENHEIMER, *Zur Quantentheorie der Molekeln*, Annalen der Physik, 389 (1927), pp. 457–484.
- [7] C. A. BRASIL, F. F. FANCHINI, AND R. D. J. NAPOLITANO, *A simple derivation of the Lindblad equation*, Revista Brasileira de Ensino de Física, 35 (2013), pp. 01–09.
- [8] M. BRAB, *Ab initio calculations of the electron capture spectrum in ^{163}Ho* , PhD thesis, Heidelberg University, 2021.
- [9] M. BRAB, C. ENSS, L. GASTALDO, R. J. GREEN, AND M. W. HAVERKORT, *Ab initio calculation of the calorimetric electron-capture spectrum of ho 163: Intra-atomic decay into bound states*, Physical Review C, 97 (2018), p. 054620.

- [10] M. BRAB AND M. W. HAVERKORT, *Ab initio calculation of the electron capture spectrum of ^{163}Ho : Auger-Meitner decay into continuum states*, New J. Phys., 22 (2020).
- [11] J. CHADWICK, *Intensitätsverteilung im magnetischen Spectrum der β -Strahlen von Radium B + C*, Verhandl. Dtsc. Phys. Ges., 16 (1914), p. 383.
- [12] M. CHERGUI, *Ultrafast photophysics of transition metal complexes*, Accounts of chemical research, 48 (2015), pp. 801–808.
- [13] P. B. CORKUM AND F. KRAUSZ, *Attosecond science*, Nature physics, 3 (2007), pp. 381–387.
- [14] J. H. DE BOER AND E. J. W. VERWEY, *Semi-conductors with partially and with completely filled 3d-lattice bands*, Proceedings of the Physical Society, 49 (1937), p. 59.
- [15] J. L. DEHMER, *Evidence of effective potential barriers in the x-ray absorption spectra of molecules*, The Journal of Chemical Physics, 56 (1972), pp. 4496–4504.
- [16] P. A. M. DIRAC, *The quantum theory of the emission and absorption of radiation*, Proceedings of the Royal Society of London. Series A, Containing Papers of a Mathematical and Physical Character, 114 (1927), pp. 243–265.
- [17] F. J. DYSON, *The radiation theories of Tomonaga, Schwinger, and Feynman*, Physical Review, 75 (1949), p. 486.
- [18] —, *The S matrix in quantum electrodynamics*, Physical Review, 75 (1949), p. 1736.
- [19] —, *Divergence of perturbation theory in quantum electrodynamics*, Physical Review, 85 (1952), p. 631.
- [20] T. ENSS, *Condensed matter theory (lecture notes)*, 2016.
- [21] H. ESCHRIG AND K. KOEPERNIK, *Tight-binding models for the iron-based superconductors*, Physical Review B, 80 (2009), p. 104503.
- [22] R. C. EVANS, P. DOUGLAS, AND H. D. BURROW, *Applied photochemistry*, Springer, 2013.
- [23] U. FANO, *Effects of configuration interaction on intensities and phase shifts*, Physical Review, 124 (1961), p. 1866.

- [24] E. FERMI, *Versuch einer Theorie der β -Strahlen. I*, Zeitschrift für Physik, 88 (1934), pp. 161–177.
- [25] S. FUKUDA, Y. FUKUDA, M. ISHITSUKA, ET AL., *Constraints on neutrino oscillations using 1258 days of Super-Kamiokande solar neutrino data*, Physical Review Letters, 86 (2001), p. 5656.
- [26] Y. FUKUDA, T. HAYAKAWA, E. ICHIHARA, ET AL., *Evidence for oscillation of atmospheric neutrinos*, Physical Review Letters, 81 (1998), p. 1562.
- [27] L. GASTALDO. Personal correspondence, 13. Feb 2021.
- [28] L. GASTALDO, K. BLAUM, K. CHRYSALIDIS, ET AL., *The electron capture in ^{163}Ho experiment—ECHO*, The European Physical Journal Special Topics, 226 (2017), pp. 1623–1694.
- [29] V. GORINI, A. KOSSAKOWSKI, AND E. C. G. SUDARSHAN, *Completely positive dynamical semigroups of N -level systems*, Journal of Mathematical Physics, 17 (1976), pp. 821–825.
- [30] J. P. GRAM, *Om rackendvilklinger bestemte ved hjaelp af de minfste kvadraters metode, translated in German as: Über die Entwicklung reeller Funktionen in Reihen mittels der Methode der kleinsten Quadrate*, Journal für reine und angewandte Mathematik, 94 (1883), pp. 41–73.
- [31] M. W. HAVERKORT, *Quanty for core level spectroscopy-excitons, resonances and band excitations in time and frequency domain*, Journal of Physics: Conference Series, 712 (2016), p. 012001.
- [32] M. W. HAVERKORT, G. SANGIOVANNI, P. HANSMANN, ET AL., *Bands, resonances, edge singularities and excitons in core level spectroscopy investigated within the dynamical mean-field theory*, EPL (Europhysics Letters), 108 (2014), p. 57004.
- [33] M. W. HAVERKORT, M. ZWIERZYCKI, AND O. K. ANDERSEN, *Multiplet ligand-field theory using wannier orbitals*, Physical Review B, 85 (2012), p. 165113.
- [34] P. HOHENBERG AND W. KOHN, *Inhomogeneous electron gas*, Physical review, 136 (1964), p. B864.
- [35] W. HÜBNER AND G. P. ZHANG, *Ultrafast spin dynamics in nickel*, Physical Review B, 58 (1998), p. R5920.

- [36] E. HUDSON, D. A. SHIRLEY, M. DOMKE, ET AL., *High-resolution measurements of near-edge resonances in the core-level photoionization spectra of sf 6*, Physical Review A, 47 (1993), p. 361.
- [37] M. IWAMURA, S. TAKEUCHI, AND T. TAHARA, *Ultrafast excited-state dynamics of copper^(I) complexes*, Accounts of chemical research, 48 (2015), pp. 782–791.
- [38] W. JIN, C. LI, G. LEFKIDIS, AND W. HÜBNER, *Laser control of ultrafast spin dynamics on homodinuclear iron-and nickel-oxide clusters*, Physical Review B, 89 (2014), p. 024419.
- [39] M. KADEK, L. KONECNY, B. GAO, ET AL., *X-ray absorption resonances near L_{2,3}-edges from real-time propagation of the Dirac-Kohn-Sham density matrix*, Physical Chemistry Chemical Physics, 17 (2015), pp. 22566–22570.
- [40] K. KOEPERNIK AND H. ESCHRIG, *Full-potential nonorthogonal local-orbital minimum-basis band-structure scheme*, Physical Review B, 59 (1999), p. 1743.
- [41] W. KOHN, *Nobel lecture: Electronic structure of matter—wave functions and density functionals*, Reviews of Modern Physics, 71 (1999), p. 1253.
- [42] W. KOHN AND L. J. SHAM, *Self-consistent equations including exchange and correlation effects*, Physical review, 140 (1965), p. A1133.
- [43] A. KOMNIK AND S. HEINZE, *Analytical results for the Green’s functions of lattice fermions*, Physical Review B, 96 (2017), p. 155103.
- [44] A. N. KRYLOV, *On the numerical solution of the equation by which in technical questions frequencies of small oscillations of material systems are determined*, Izvestija AN SSSR (News of Academy of Sciences of the USSR), Otdel. mat. i estest. nauk, 7 (1931), pp. 491–539.
- [45] M. W. KUTTA, *Beitrag zur näherungsweise Integration totaler Differentialgleichungen*, Z. Math. Phys., 46 (1901), pp. 435–453.
- [46] K. LÁNCZOS, *An iteration method for the solution of the eigenvalue problem of linear differential and integral operators*, Journal of Research of the National Bureau of Standards, 45 (1950), pp. 255–282.
- [47] G. LINDBLAD, *On the generators of quantum dynamical semigroups*, Communications in Mathematical Physics, 48 (1976), pp. 119–130.

- [48] P.-O. LÖWDIN, *On the non-orthogonality problem connected with the use of atomic wave functions in the theory of molecules and crystals*, The Journal of Chemical Physics, 18 (1950), pp. 365–375.
- [49] S. MAI AND L. GONZÁLEZ, *Molecular photochemistry: Recent developments in theory*, Angewandte Chemie International Edition, 59 (2020), pp. 16832–16846.
- [50] Z. MAKI, M. NAKAGAWA, AND S. SAKATA, *Remarks on the unified model of elementary particles*, Progress of Theoretical Physics, 28 (1962), pp. 870–880.
- [51] D. MANZANO, *A short introduction to the Lindblad master equation*, AIP Advances, 10 (2020), p. 025106.
- [52] R. D. MATTUCK, *A guide to Feynman diagrams in the many-body problem*, Courier Corporation, 1992.
- [53] J. K. MCCUSKER, *Femtosecond absorption spectroscopy of transition metal charge-transfer complexes*, Accounts of chemical research, 36 (2003), pp. 876–887.
- [54] L. MEITNER, *Über die Entstehung der β -Strahl-Spektren radioaktiver Substanzen*, Zeitschrift für Physik, 9 (1922), pp. 131–144.
- [55] M. MERSTORF. Personal correspondence, 27. Jan 2021.
- [56] S. MERTENS, *Direct neutrino mass experiments*, J. Phys. Conf. Ser, 718 (2016), p. 022013.
- [57] C. J. MILNE, T. J. PENFOLD, AND M. CHERGUI, *Recent experimental and theoretical developments in time-resolved X-ray spectroscopies*, Coordination Chemistry Reviews, 277 (2014), pp. 44–68.
- [58] N. F. MOTT AND R. PEIERLS, *Discussion of the paper by de Boer and Verwey*, Proceedings of the Physical Society, 49 (1937), p. 72.
- [59] R. S. MULLIKEN, *Electronic population analysis on LCAO–MO molecular wave functions. I*, The Journal of Chemical Physics, 23 (1955), pp. 1833–1840.
- [60] Y. ONODERA AND Y. TOYOZAWA, *Excitons in alkali halides*, Journal of the Physical Society of Japan, 22 (1967), pp. 833–844.
- [61] W. PAULI, *The connection between spin and statistics*, Physical Review, 58 (1940), p. 716.

- [62] L. PAULING, *The nature of the chemical bond. Application of results obtained from the quantum mechanics and from a theory of paramagnetic susceptibility to the structure of molecules*, Journal of the American Chemical Society, 53 (1931), pp. 1367–1400.
- [63] E. PAVARINI, *Crystal-field theory, tight-binding method and Jahn-Teller effect*, Correlated electrons: from models to materials, 2 (2012).
- [64] P. PEARLE, *Simple derivation of the Lindblad equation*, European journal of physics, 33 (2012), p. 805.
- [65] J. P. PERDEW AND Y. WANG, *Accurate and simple analytic representation of the electron-gas correlation energy*, Physical review B, 45 (1992), p. 13244.
- [66] J. PLEMELJ, *Problems in the sense of Riemann and Klein*, Interscience Publishers, (1964).
- [67] C. RUNGE, *Über die numerische Auflösung von Differentialgleichungen*, Mathematische Annalen, 46 (1895), pp. 167–178.
- [68] P. RUPPRECHT, L. AUFLEGER, S. HEINZE, ET AL., *Laser control of multi-electron interaction in molecules*. In preparation.
- [69] E. SCHMIDT, *Über die Auflösung linearer Gleichungen mit unendlich vielen Unbekannten*, Rendiconti del Circolo Matematico di Palermo (1884-1940), 25 (1908), pp. 53–77.
- [70] E. SCHRÖDINGER, *An undulatory theory of the mechanics of atoms and molecules*, Physical review, 28 (1926), p. 1049.
- [71] J. C. SLATER, *The theory of complex spectra*, Physical Review, 34 (1929), p. 1293.
- [72] J. C. SLATER AND W. F. MEGGERS, *Quantum theory of atomic structure*, Physics Today, 14 (1961), p. 48.
- [73] I. TAVERNELLI, E. TAPAVICZA, AND U. ROTH LISBERGER, *Non-adiabatic dynamics using time-dependent density functional theory: Assessing the coupling strengths*, Journal of Molecular Structure: THEOCHEM, 914 (2009), pp. 22–29.
- [74] J. H. VAN VLECK, *Theory of the variations in paramagnetic anisotropy among different salts of the iron group*, Physical Review, 41 (1932), p. 208.

- [75] C. VELTE, *Measurement of a high energy resolution and high statistics ^{163}Ho electron capture spectrum for the ECHo experiment*, PhD thesis, Heidelberg University, 2020.
- [76] C. VELTE, F. AHRENS, A. BARTH, ET AL., *High-resolution and low-background ^{163}Ho spectrum: interpretation of the resonance tails*, *The European Physical Journal C*, 79 (2019), pp. 1–8.
- [77] A. VLČEK JR., *The life and times of excited states of organometallic and coordination compounds*, *Coordination Chemistry Reviews*, 200 (2000), pp. 933–978.
- [78] J. VON NEUMANN, *Wahrscheinlichkeitstheoretischer Aufbau der Quantenmechanik*, *Nachrichten von der Gesellschaft der Wissenschaften zu Göttingen, Mathematisch-Physikalische Klasse*, 1927 (1927), pp. 245–272.
- [79] G. H. WANNIER, *The structure of electronic excitation levels in insulating crystals*, *Physical Review*, 52 (1937), p. 191.
- [80] C. WU, *History of beta decay*, in *Beiträge zur Physik und Chemie des 20. Jahrhunderts*, Springer, 1959, pp. 45–65.
- [81] J. ZAAANEN, G. A. SAWATZKY, AND J. W. ALLEN, *Band gaps and electronic structure of transition-metal compounds*, *Physical Review Letters*, 55 (1985), p. 418.
- [82] F. ZHANG, *The Schur complement and its applications*, vol. 4, Springer Science & Business Media, 2006.